Final Scientific/Technical Report

Award Number: DE-EE0003265

Recipient: Purdue University

Title: Establishing a Comprehensive Wind Energy Program

Project Period: July 1, 2010 – June 30, 2012

Working Partners: Sanford Fleeter, Doug Adams – Mechanical Engineering, Purdue West Lafayette IN, Chenn Zhou, Xiuling Wang – Mechanical Engineering Purdue Calumet IN, David Kozel, Constantin Apostoaia – Electrical and Computer Engineering Purdue Calumet IN

Cost-Sharing Partners: Purdue University – Calumet and West Lafayette

PI: Sanford Fleeter, Mechanical Engineering, Purdue University, West Lafayette, Indiana 47906 fleeter@purdue.edu

Executive Summary

This project was directed at establishing a comprehensive wind energy program in Indiana, including both educational and research components. A graduate/undergraduate course ME-514 - Fundamentals of Wind Energy has been established and offered and an interactive prediction of VAWT performance developed. Vertical axis wind turbines for education and research have been acquired, instrumented and installed on the roof top of a building on the Calumet campus and at West Lafayette (Kepner Lab). Computational Fluid Dynamics (CFD) calculations have been performed to simulate these urban wind environments. Also, modal dynamic testing of the West Lafayette VAWT has been performed and a novel horizontal axis design initiated. The 50-meter meteorological tower data obtained at the Purdue Beck Agricultural Research Center have been analyzed and the Purdue Reconfigurable Micro Wind Farm established and simulations directed at the investigation of wind farm configurations initiated. The virtual wind turbine and wind turbine farm simulation in the Visualization Lab has been initiated.

Table of Contents

Comparison of Accomplishments with Project Goals & Objectives

Wind Energy & Wind Turbine Education

Objective: Initiate the development of graduate/undergraduate curricula in Energy Engineering with an emphasis on Wind Power including the development of a course titled "Fundamentals of Wind Energy" including initiating the development of a laboratory component, software that enables students to perform realistic projects involving the design of wind turbines.

Accomplishments: These objectives have been accomplished. The graduate/undergraduate course ME-514 - Fundamentals of Wind Energy has been established and offered. Also, an interactive prediction of VAWT performance has been developed.

Small & Urban Wind Turbines

Objective: Small vertical axis wind turbines for research and education will be acquired, instrumented and installed on the roof tops of buildings on the Calumet and West Lafayette campuses. Modal dynamic testing of the West Lafayette VAWT will be performed and Computational Fluid Dynamics (CFD) initiated to simulate these urban wind environments.

Accomplishments: These objectives have been accomplished. Vertical axis wind turbines have been acquired, instrumented and installed on the tops of buildings on the Calumet and West Lafayette campuses. Modal dynamic testing of the West Lafayette VAWT has been performed. The CFD calculations have been performed to simulate these urban wind environments.

Purdue Micro Wind Farm

Objective: The rural wind environment will be investigated, accomplished by analyzing the 50-meter meteorological tower data obtained at the Purdue Beck Agricultural Research Center. Also, the Purdue Micro Wind Farm will be established, with the reconfigurable wind turbines mounted on their semi-portable bases and instrumentation installed to measure their aerodynamic performance. Simulations directed at the investigation of wind farm configurations that optimize the overall wind farm performance, wind turbine aerodynamic performance, and turbine-turbine aerodynamic interactions will be initiated.

Accomplishments: These objectives have been accomplished. The 50-meter meteorological tower data obtained at the Purdue Beck Agricultural Research Center have been analyzed and the Purdue Reconfigurable Micro Wind Farm established. Also simulations directed at the investigation of wind farm configurations have been initiated.

Virtual Reality Visualization

Objective: A virtual wind turbine and wind turbine farm simulation will be initiated in the Purdue Calumet Visualization Lab.

Accomplishments: These objectives have been accomplished. The virtual wind turbine and wind turbine farm simulation in the Visualization Lab has been initiated.

Summary of Project Activities

Wind Energy & Wind Turbine Education

The graduate/undergraduate course ME-514-Fundamentals of Wind Energy has been established and offered and an interactive prediction of VAWT performance has been developed.

This course introduces the student to the technology and economics of converting wind energy to electricity and for integration with pumps. Both utility scale horizontal axis wind turbines and small horizontal and vertical axis wind turbine technology are addressed, as well as wind energy environmental issues.

With the current increased interest in developing renewable energy, there is renewed interest in VAWTs for small wind applications. Hence, the goal of this project is to develop an interactive computational tool to predict the aerodynamic performance of VAWTs that is computationally less demanding.

A streamtube is an arbitrary surface formed by streamlines, with no flow crossing the boundary. Streamtube models are based upon the idea of relating the change in streamwise momentum to the aerodynamic forces on the rotor which is represented as an actuator disk. The actuator disk is a 1-D representation of a fluid machine where work is exchanged with the velocity continuous and the pressure discontinuous. The relationship between the velocity upstream of the actuator disk and that induced at the disk is also known as the Actuator Disk theory (ADT). The aerodynamics forces acting on an airfoil section are a result of the lift and drag. These forces are summed over all blade elements defined along the rotor span and originated from the blade. Figure 1 shows the general setup used throughout this work.

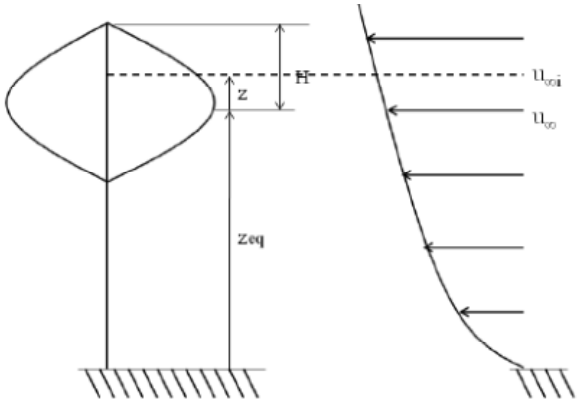

Figure 1. VAWT with its equator at 0 meters from the ground. The wind velocity at the equator is taken as the reference, u_{∞} with $u_{\infty i}$ the wind velocity at different heights

The Actuator Disk Theory (ADT) models the rotor as a uniform 1-D thin disk, with uniform velocity at the disk. The velocity across the disk is continuous whereas the pressure is discontinuous.

The interactive computer tool developed is based on the double multiple streamtube (DMS) and multiple streamtube (MS) models. The latter was included for comparison of the results obtained. Both MS and DMS models involve iteration for the induced velocity and the computation of the corresponding performance parameters. Based on these streamtube models, a computer tool VAWTGUI was developed using MATLAB. It is an interactive graphical user

interface (GUI), which enables VAWT geometries and incoming velocity profiles to be defined by the user. VAWT-GUI provides various plots to enable the performance of the turbine to be evaluated.

VAWTGUI is an interactive MATLAB interface used in the prediction of the performance of VAWTs based on the MS and DMS models developed in MATLAB. Figure 2 shows the resultant GUI developed with MATLAB. The program is called VAWTGUI, and it can be categorized into four panels.

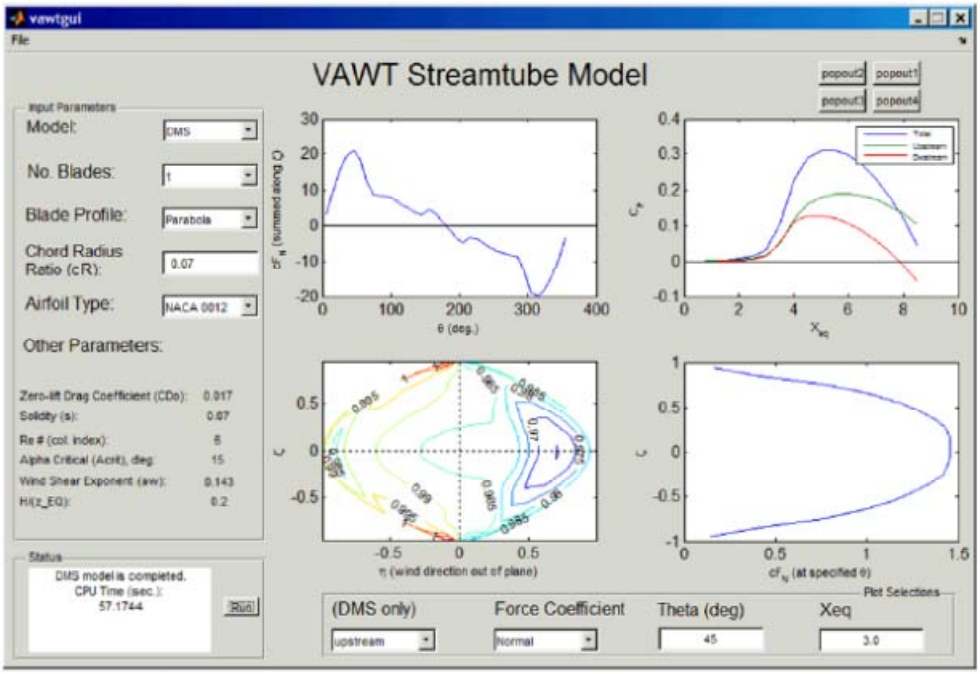

Figure 2. VAWTGUI layout.

There are five options that can be changed frequently, most of which are restricted to a few drop down options. The first option is the selection between the MS or the DMS model. The MS model is only able to deliver two of the four possible plots in the display. Next is the number of blades. Only up to three blades are available because they are the most commonly found VAWT designs. Options to apply more blades could easily be added. However, caution must be taken with the plotting commands. The following selection is the rotor blade's vertical profile, with two default shapes available. In addition, there is an option to insert a user defined blade profile based on coordinates specified in the text file *input profile:txt*. Another selection is the ratio of chord length to the largest radius *R*. Lastly, the airfoil type. NACA 0012, NACA 0015 and NACA 0018 are the three default airfoils available.

The status panel consists of a *Run* push button, and a display text box. The program is run when the *Run* button is clicked, or when the MATLAB file *vawtgui:m* is executed on the command window. Once the program is run, no changes in the status text box until the program is terminated. If the model is run successfully, the display indicates its completion with the CPU run time. Otherwise, it prompts the user to check the MATLAB command window for errors.

Upon completion of the streamtube model calculations, the results are displayed on the four plot axes. The corresponding plots are as follows, clockwise from top right:

- Power coefficient (C_p) vs. tip speed ratio (X_{eq})
- ζ vs. individual force coefficient (cF_N or cFT) at a specified angular location (θ)
- Contour plot of the interference factor (a). Option to change to display both surface and contour plots.
- Sum of force coefficient (cF_N or cFT) along ζ vs. angular location θ

On the top right corner are four push buttons corresponding to the location of the four plots. These are pop-up buttons, which enable plots to be displayed as standalone windows. The MS model is only able to deliver results for the first and third plots.

The Syllabus for ME-514 Fundamentals of Wind Energy and the details of the interactive prediction of VAWT performance are presented in Appendix A.

Small & Urban Wind Turbines

Vertical axis wind turbines have been acquired, instrumented and installed on the roof top of a building on the Calumet campus and at West Lafayette (Kepner Lab), with Computational Fluid Dynamics (CFD) calculations performed to simulate the urban wind environments. Modal dynamic testing of the West Lafayette VAWT has been performed. Also, a novel horizontal axis wind turbine has been designed.

An EddyGT vertical axis wind turbine (VAWT) was installed on a two meter tower on the roof of the Student Union Library Building (SUL) at Purdue Calumet, Figure 3. Two of the three anemometers used for measuring wind speed are also shown. A similar wind turbine was installed at Kepner Labs, Purdue West Lafayette.

Figure 3. Wind turbine and anemometers with vanes on roof of SUL building.

The CFD modeling starts with geometry model construction. Based on geometry model computational meshes are generated. Then the input condition and boundary conditions are applied to the CFD model. After running the CFD models, numerical results are obtained. Numerical results are validated with experimental data. Once the accuracy of the simulation results is checked to be acceptable, post-processing of the results is developed. Predictions of the wind power density past the Purdue Calumet Buildings arrays are shown in Figure 4.

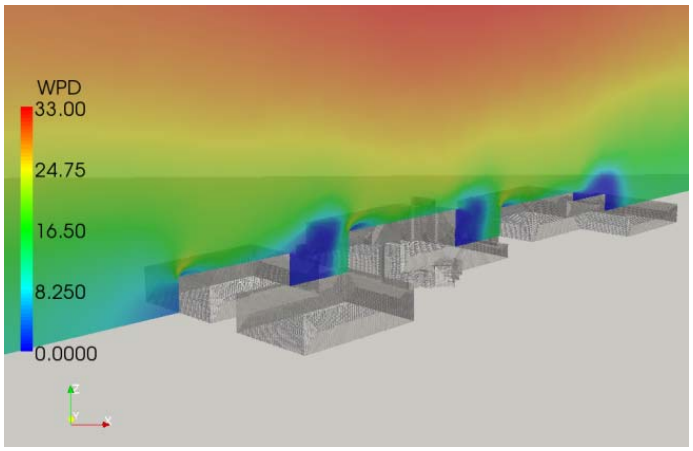

Figure 4. Side View of Contours of Wind Power Density

Modern utility-scale wind turbines are equipped with several types of sensors for monitoring the wind resource as well as mechanical and electrical variables of interest in the turbine. The performance and reliability of wind turbines are largely governed by the nature of the wind loads that act on the turbine rotor blades. The ability to characterize these loads in real time is advantageous for implementing control algorithms that increase energy capture, which is the primary short-term measure of wind turbine performance. An equally important measure of performance is long-term wind turbine reliability. Reliability is related to the structural integrity of the blade root, low speed shaft, yaw joint, and other load bearing components.

A more complete awareness of the temporal and spatial variations in the wind loads that act upon the turbine rotor would allow operators to implement advanced control and maintenance strategies. Such information could also provide an understanding of why similar turbines in the same wind farm experience different failure patterns. The methodologies developed characterize how the rotor forced response changes due to yaw and pitch set-point errors and how these changes affect the sensitivity of blade measurements to damage mechanisms. This understanding can be applied to improve energy capture while simultaneously facilitating turbine health management.

The centerpiece of the test apparatus is a Whisper 100™ 2.1 meter rotor diameter wind turbine manufactured by Southwest Windpower®. To observe the structural dynamics of the rotor, tri-axial accelerometers were mounted in several key locations. Figure 5 highlights the locations of all sensors and transducers on the wind turbine.

Experiments were performed in a wind tunnel, with a total of 189 tests conducted at a wind speed of approximately 7 mph. The test duration was ten minutes and began when the rotor had reached its steady state rotational speed. The test data were later segmented into an ensemble of ten, one-minute duration consecutive data sets to allow for the application of statistical analysis. Damage conditions correspond to no damage, blade ice accretion, and a blade root crack, respectively. The damage conditions were tested through a range of yaw error angles, pitch error angles, and wind states to determine how the blade dynamic response changes due to both variations in the wind state and damage to the rotor.

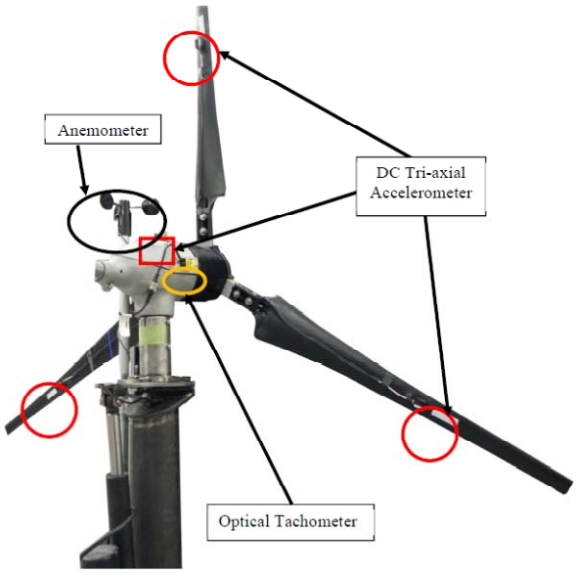

Figure 5. Locations of sensors and transducers on the wind turbine.

Wind turbine rotor blade modes of vibration are excited by wind loads to a greater or lesser degree depending on both the frequency of wind loading and the spatial distribution of that loading. The first step taken to identify changes in the operating state of the wind turbine rotor was to characterize the free dynamic response of the three-bladed rotor system. Knowledge of the free response of the rotor is critical when attempting to monitor the health of the blades because the operational response is a convolution of the blade free response characteristics and the blade forcing function. The mode shapes and resonant frequencies of the rotor dictate the modes of vibration that will be most sensitive to changes in the turbine's operating state (i.e. changes in wind state and/or changes in yaw and pitch set point) and blade damage condition.

To identify the free response characteristics of the wind turbine rotor system, a modal impact test was performed. A multi-reference modal impact test was conducted using three measurement degrees of freedom (DOF) that were local to each rotor blade's coordinate system. Figure 2-11 6 illustrates the local degrees of freedom of a rotor blade.

Experiments were conducted by controlling the inflow conditions and measuring the inertial response of the rotor blades as a function of yaw error, pitch error, and simulated damage conditions (ice accretion and blade root crack). Using cyclic averaging in conjunction with operational modal analysis techniques, it was demonstrated that the sensitivity of the measured blade flap and lead-lag acceleration responses to yaw error was larger in the presence of vertical wind shear than in the case of uniform flow, but smaller in the presence of horizontal wind shear. It was also shown using these same operational blade acceleration measurements that the presence of either horizontal or vertical shear inflow conditions makes it possible to distinguish between positive and negative yaw error, which would be important for controlling yaw error in practice. In contrast, the measured blade acceleration responses did not exhibit a significant sensitivity to a single blade pitch error. Although the small-scale wind turbine blade that was tested has a substantially different aerodynamic profile than a utility-scale blade, the measurement technique and data analysis methodology are general and can translate well to utility-scale blades.

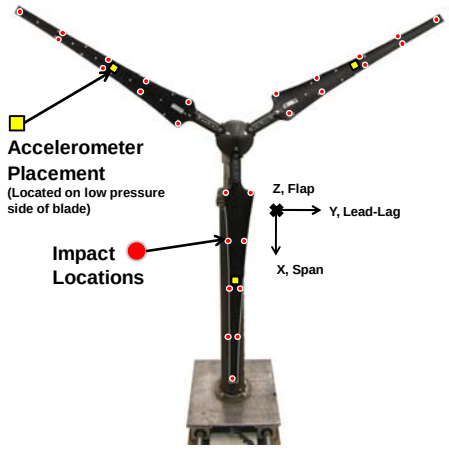

Figure 2-11 6. Accelerometer placement, input-output measurement and degrees of freedom

It was also shown that ice accretion could be detected using the lead-lag operational blade acceleration measurements at a frequency of one per revolution regardless of the yaw error and regardless of the inflow condition (vertical or horizontal wind shear). The percent change in the lead-lag acceleration response at this frequency was 35%. Likewise, the percent change in the lead-lag response was again 35% for pitch errors less than 5 degrees, and the presence of ice could be detected regardless of pitch error. For the case of a simulated blade root crack, the flap acceleration response of the blade showed the most sensitivity to the simulated damage. The presence of the faulty blade could be detected regardless of the yaw/pitch error and regardless of the inflow conditions.

The results of this investigation indicate that blade operational acceleration responses in conjunction with operational modal analysis techniques are a promising means of detecting and characterizing yaw error and certain blade damage conditions. The experiments demonstrate that the data analysis procedure is capable of extracting features that can detect errors in yaw and pitch as well as simulated damage conditions despite significant variations in the wind inflow conditions, which is an important finding given that such variations are prevalent in utility-scale wind farms.

These accomplishments are detailed in Appendix B and Appendix C, with the VAWT and SCADA System at Purdue Calumet are detailed in Appendix D.

Purdue Micro Wind Farm

Wind speeds were recorded in West Lafayette, Indiana from October 1st, 2008 to December 31st, 2009 and analyzed to determine the wind speed trends both throughout the year and throughout the day. A Weibull function is fit to the data and its accuracy proven in the quality of the Weibull calculated average wind speed. The five anemometer height locations are used to describe the atmospheric velocity profile, which is studied to understand its trends. The wind speed data is used to calculate performance for both residential and utility-size wind turbines. Two leading manufacturers of small wind turbines are compared at varying hub heights, and three utility size wind turbines from one manufacturer are compared which vary in rotor diameter and generator size.

The analysis of wind speed data shows strong seasonal and daily trends. Within the day and throughout the year wind speeds are observed that fluctuate as a substantial percentage of the average. The trends hold that highest wind speeds occur seasonally in winter and early spring, and the lowest values are during the summer months. Daily variations are such that the lowest wind speeds occur in the first half of the day where the highest values are in the second half. The time within the day averages out from the year to occur at 7:10 am and 4:25 pm for the minimum and maximum. The distribution of the wind speed was described using the Weibull probability function and the accuracy of this method is again proven for both estimating the average velocity from calculated parameters and from estimating the power in the wind with maximum errors around 0.85% and 4%. The atmospheric velocity profile was estimated using a power law approximation and coefficients determined.

Wind turbine performance within the measured wind conditions were calculated for small residential wind turbines and for utility-size wind turbines to compare. The two small wind turbines compared differed by about 33% on the year at 50m in capacity factor with a 32.8% maximum value average on the year. A comparative study between rotor diameter and rated power was performed for utility-size wind turbines, with 100m and 1.6 MW as the benchmark. Performing in the wind conditions of this study revealed that the low capacity, large rotor diameter had the highest capacity factor, but also the lowest power coefficient on the year. The low capacity, small rotor diameter had the highest power coefficient on the year. Increasing the rotor diameter by 21% resulted in a 19% increase in the power production for the 1.6 MW machines, therefore an 8.6% decrease in average power coefficient. For the turbine with a 56% increase in the rated capacity, the capacity factor decreased by only 28%.

The Purdue University Micro Reconfigurable Wind Farm consists of four wind turbines mounted on movable carts located in a field north of Zucrow Laboratories, Figure 7. Southwest Windpower Whisper 100 wind turbines are used in this facility which has a 900W rated power and a 7-ft diameter. The turbines have a hub height of approximately 35-ft above the ground level. Two of the four turbines are instrumented and data collected on the cart. Produced power is used to power the instrumentation with additional power sent to a dump load resistor bank. Wind farm wind speed is measured with an anemometer mounted at the same height as the turbines 200-ft east of the instrumented turbines, also shown in Figure 7.

Two instrumented wind turbines will be used to measure the performance and load effects on operating in wakes of upstream turbines.

Figure 7. Micro Reconfigurable Wind Farm and anemometer

Generalized actuator disc and related methods, which combine full set Navier Stokes equations with a blade element approach and two-dimensional airfoil data, is a promising technique for studying the dynamics in the wake since the influence of the blades on the flow field is modeled with a limited number of mesh points. This technique has been used for both stand alone turbines and rows of wind turbines. Computations have mostly been carried out assuming steady state or uniform inflow but a few studies have been conducted in simulated atmospheric boundary layers.

The objectives of this task is to develop a high order finite volume CFD solver, combine the generalized actuator disc and actuator line methods, provide detailed knowledge of wind-turbine wakes and atmospheric turbulence over a wide range of spatial and temporal scales, provide accurate prediction of the ABL flow and its interaction with wind turbines as well as turbine-induced wakes, gain more insight into the phenomenon of wake interaction and how it affects the external aerodynamic loads on wind turbines in order to maximize wind energy production and minimize fatigue loading in the evaluation of wind farm layouts, and to provide valuable quantitative insight into the potential impacts of wind farms on local meteorology.

Simulation results are obtained for atmospheric boundary layer LES simulation combined actuator line model. The contour plot for iso-surface contour is shown in Figure 8.

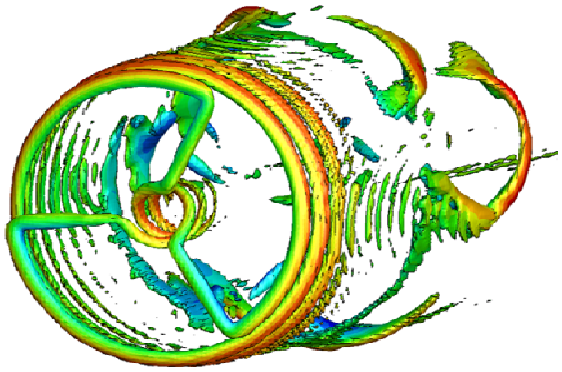

Figure 8. Wind turbine wake simulation with Actuator Line Method

These accomplished are detailed in Appendix E.

Virtual Reality Visualization

The virtual wind turbine and wind turbine farm simulation in the Visualization Lab has been initiated. A 3-D Virtual Wind Turbine (VWT) simulator was created and used in an introductory wind energy engineering course (dual level graduate/undergraduate) at Purdue University Calumet. The GE 1.5 Megawatt turbine was selected to act as a model for the creation of the VWT based on literature review and input from instructors at Purdue Calumet and the Wind Turbine Technician Academy at Kalamazoo Valley Community College. 3-D geometry of a GE 1.5 turbine was created based on publicly available photos, and was later refined based on direct inspection of a GE 1.5 Megawatt turbine during a site visit to a wind farm in Illinois, Figure 9.

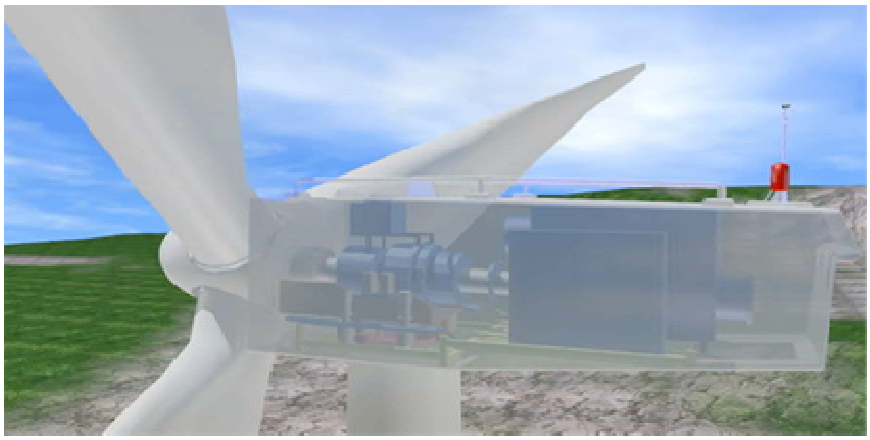

Figure 9. 3-D geometry of a GE 1.5 turbine

The 3-D VWT uses the open source package "OpenSceneGraph" (OSG). The model can be loaded on a variety of systems including PC, and fully immersive VR system. For the pilot implementation with the Purdue Calumet Wind Energy Engineering course, students viewed and interacted with the simulator in the Immersive Theater at the Center for Innovation through Visualization and Simulation. The simulator combined multiple copies of the GE 1.5 wind turbines to create a small wind farm. Students navigated through the wind farm, observed the entrance and control systems at the base of the tower, and climbed the tower ladder to reach the nacelle at the top of a turbine. There, the course instructor provided an orientation of the various components of the turbine, while the blades were spinning. The nacelle covering for one turbine was made transparent so students could see the internal components. Students then flew to another turbine to learn how the control systems worked with automated instruments to turn the turbine blades into the wind to harvest the most energy.

The 3-D Virtual Wind Turbine is usable to explore in fully immersive Virtual Reality, or on standard PC. The initial version was completed in Fall 2011 and implemented in an Intro to Wind Energy Course at Purdue University Calumet.

Another simulator has been developed for undergraduate (and graduate) engineering courses related to wind energy. The simulator is designed as interactive 3D software that demonstrates and allows exploration of wind turbine components, energy flow through turbine systems, and aerodynamic properties of wind turbine blades. Extensive Computational Fluid Dynamics (CFD) simulations are being developed to be integrated into the aerodynamics section of the software.

As illustrated in Figure 10, students can learn about turbine components (left), Aerodynamics equations (center), and Aerodynamic properties of wind turbine blades (right).

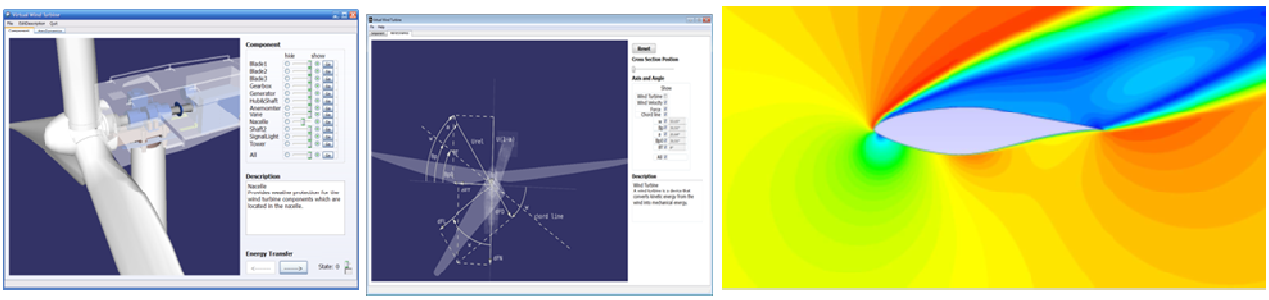

Figure 10. Simulator examples

The following achievements have been accomplished for this simulator:

- Initial version was completed in Fall 2011.
- Used in Purdue Calumet Intro to Wind Energy course
- Presented poster at American Wind Energy Association (AWEA) Wind Power conference (June 5, 2012)

Products developed and Technology Transfer

a. Publications, conference papers, or other public releases of results.

Adams, D. E., Kusnick, J., Dana, S., and Yutzy, J., "Dynamics-Based Health Monitoring and Control of Wind Turbine Rotors," *Emerging Topics of Aerodynamics in Wind Energy*, WIT Press, 2012 (in press).

Dana, S., and Adams, D. E., "Dynamics-Based Health Monitoring of Wind Turbine Rotor Blades using Integrated Inertial Sensors," Proceedings of the International Design Engineering Technical Conferences & Computers and Information in Engineering Conferences, IDETC/CIE 2012, August 12-15, Chicago, IL.

Yutzy, J. Dana, S., and Adams, D. E., "Model Identification and Operating Load Characterization for a Small Horizontal Axis Wind Turbine Rotor using Integrated Blade Sensors," 2010, *Proceedings of the Dynamic Systems and Control Conference*, Boston, MA.

Kusnick, J., and Adams, D., "Vertical Axis Wind Turbine Operational Modal Analysis in Sheared Wind Flow," 2012, *Proceedings of the International Modal Analysis Conference*, Jacksonville, FL.

Yutzy, J., and Adams, D. E., "Load Shaping for Maximizing Energy Capture and Structural Health in a HAWT Using Rotor-Mounted Inertial Sensors," 2011, *Proceedings of the 8th International Workshop on Structural Health Monitoring*, Palo Alto, CA.

Dana, S. R., and Adams, D. E., "Operational Damage Detection of Turbine Rotors using Integrated Blade Sensors," 2011, *Proceedings of the International Modal Analysis Conference*, Jacksonville, FL.

C. Wilson, D. Kozel, and C. Apostoaia, "Educational Tools for Wind Energy Programs", accepted and presented at 2012 ASEE Illinois - Indiana Section Conference, March 17, 2012, Valparaiso University, Valparaiso IN.

L. Lu and X. Wang, "The application of computational fluid dynamics for installing the roof-mounted wind turbine" (accepted) 2012 ASME International Mechanical Engineering Congress and Exposition, Nov. 9-15, 2012, Houston, Texas.

L. Lu and X. Wang, "Integration of computational fluids dynamics and virtual reality visualization for constructing the wind field", 2011 ASME International Mechanical Engineering Congress and Exposition, Nov. 11-17, 2011, Denver, Colorado.

J. Moreland, T. Okosun, C. Wang, X. Wang and C. Zhou, "Development and pilot implementation of a virtual wind turbine simulator", Wind Power 2012 conference and exhibition, Jun. 3-6, 2012, Atlanta, GA.

L. Lu**, X. Wang, S. Kothakapu, C. Qian and J. Moreland, "Virtual reality applied for visualization of 3D wind field on Purdue university calumet campus", Proceedings of the ASME 2011 World Conference on Innovative Virtual Reality, June 27-29, 2011, Milan, Italy.

Lu, L., Wang, X., Kothakapu, S., Moreland, J., and Zhou, C. Q., 2011, "Wind Field Simulation for Placement of Small Scale Wind Turbines on a College Campus", Proceedings of the ASME 2011 World Conference on Innovative Virtual Reality, WINVR2011, Milan, Italy.

Moreland, J., Okosun, T., Wang, C., Wang, X., Zhou, C. 2012. “Development and Pilot Implementation of a Virtual Wind Turbine Simulator”, Proceedings of the AWEA 2012 Wind Power Conference, WindPower2012, Atlanta, GA.

Yan, N., Okosun, T., Basak, S. K.., Fu, D., Moreland, J. M., and Zhou, C. Q., 2011, "Numerical Simulation and Virtual Reality Visualization of Horizontal and Vertical Axis Wind Turbines", Proceedings of the ASME 2011 International Design Engineering Technical Conferences & Computers and Information in Engineering Conference, IDETC2011, Washington, DC, DETC2011-47969

b. Web site or other Internet sites that reflect the results of this project;

http://webs.purduecal.edu/civs/research/renewable-energy-applications/wind-energy-2/

http://civsweb01.purduecal.edu/fipse/?page_id=24

The following link shows live video from atop Purdue University Calumet Student Union and Library Building of the 1000 W Vertical Axis Wind Turbine from Urban Green Energy. Left of the wind turbine is a 3D anemometer, 2D anemometer with weather station from Gill Instruments, and an anemometer/vane from RainWise.

http://civsweb01.purduecal.edu/fipse/?page_id=24

Also a video is available on the following website.

http://webs.purduecal.edu/civs/research/renewable-energy-applications/wind-energy-2

c. Networks or collaborations fostered;

Wind tunnel tests of 100W Vertical Axis Wind Turbines for Windstream, a small business in New Albany, IN, were performed at Purdue West Lafayette and Windstream sold thousands of these units to Brazil.

Sorian Inc. based in West Lafayette Purdue Research Park performed testing at Purdue University for commercialization of their wind turbine blade flow control technology.

National Science Foundation Cyber-Physical Systems grant of $1.6M over approximately 4 years was awarded.

Indiana Space Grant Consortium grant of $50K to conduct modal testing of Endurance horizontal axis wind turbine at Taylor University.

National Renewable Energy Laboratory $15K travel and equipment rental grant for testing of 750kW gearbox.

Student summer internship at National Renewable Energy Laboratory for modal testing of utility scale turbine.

Sandia National Laboratory $50K grant in modeling of 5MW offshore wind turbine pending.

US Dept. of Education $750K grant to develop mixed reality simulators for wind energy education

Allen-Bradley/Rockwell Automation donations over $150K of Hardware and Software for the Supervisory Control and Data Acquisition (SCADA) System on the VAWT installed on top of the SUL building at Calumet Campus in Hammond, IN described in Appendix F.

Gill Instruments donated $10K for the 3D anemometer and 2D anemometer with weather station for the verification of wind energy on top of the SUL building at Calumet Campus in Hammond, IN described in Appendix F.

d. Technologies/Techniques;

For 3-D wind fields construction, the input data for the CFD model are based on statistical analysis (Weibull and Rayleigh distribution) of the recorded data in sub-urban environment. Commercial software GAMBIT is used to construct computational mesh, FLUENT is used to conduct the simulation, specifically, the realizable k-epsilon turbulence model is employed to solve the turbulent flow. Techplot is used as post processing tools to generate x-y plots and contour plots.

e. Inventions/Patent Applications, licensing agreements

None

f. Other products, such as data or databases, physical collections, audio or video, software or netware, models, educational aid or curricula, instruments or equipment.

Dana, S., “Detection of Blade Damage and Ice Accretion for Health Monitoring of Wind Turbines Using Integrated Blade Sensors,” 2011, Master of Science Thesis, Purdue University, School of Mechanical Engineering.

Yutzy, J., “Characterizing the Structural Dynamic Response of a Horizontal Axis Wind Turbine in a Yawed Flow Field Using Rotor and Nacelle Mounted Inertial Sensors,” 2011, Master of Science Thesis, Purdue University, School of Mechanical Engineering.

Kusnick, J., “Condition Monitoring Methods and Applications for Vertical and Horizontal Axis Wind Turbines,” 2012, Master of Science Thesis, Purdue University, School of Mechanical Engineering.

Windiana posters were presented in Indianapolis, IN.

Seminars presented at Sandia National Laboratory (July 2011) and National Renewable Energy Laboratory (September 2011).

Wilson, C., “SCADA System Design for Vertical Axis Urban Wind Turbines,“ 2011, preliminary report for Master of Science Thesis.

Okosun, T., “A Computational Examination of Utility Scale Wind Turbine Wakes and Vortices to Provide Improved Siting and Efficiency,” 2012, Master of Science Thesis, Purdue University, School of Mechanical Engineering.

APPENDIX A. Wind Energy & Wind Turbine Education

This appendix presents the syllabus for ME-514 - Fundamentals of Wind Energy and the VAWT performance analysis.

Syllabus - ME-514 - Fundamentals of Wind Energy

This course introduces the student to the technology and economics of converting wind energy to electricity and for integration with pumps. Both utility scale horizontal axis wind turbines and small horizontal and vertical axis wind turbine technology are addressed, as well as wind energy environmental issues.

1. Energy Overview
    - Why energy from alternative sources
2. Introduction to Wind Energy
    - Brief History of Wind Energy
    - Current Status
3. Wind Energy Fundamentals
    - Power in the Wind
    - Actuator Disk Theory
        - Horizontal Axis Wind Turbines
        - Vertical Axis Wind Turbines
    - Wind Turbine Power & Torque
    - Rotor Characteristics
4. Wind Characteristics & Measurement
    - Ecological Indicators
        - Wind Shear
        - Turbulence
        - Anemometers
5. Wind Data Analysis
    - Average Wind Speed
    - Wind Speed Distribution
    - Statistical Models (Rayleigh & Weibull) for Wind Data Analysis
    - Energy estimation of wind regimes
6. Wind Energy Systems
    - Wind Electric Generators
    - Generator & Gearbox Characteristics
    - Wind Turbine - Pump Characteristics
    - Wind Farms
        - Turbine Wake Interactions
7. Wind Turbine Control
8. Wind Turbine Aerodynamics

- Airfoil Aerodynamics
- Axial Momentum Theorem
- Blade Element Theory
- Strip Theory
- Rotor Design
- Rotor Performance

9. Economics of Wind Energy
   - Cost of Wind Generated Electricity
10. Environmental Issues
11. Blade Dynamics

AN INTERACTIVE TOOL TO PREDICT VAWT PERFORMANCE USING STREAMTUBE MODELS

STREAMTUBE MODELS

Figure 1 shows the general setup used throughout this work. When considering wind shear, the wind velocity profile is assumed to follow the power law function with the wind shear index = 1/7.

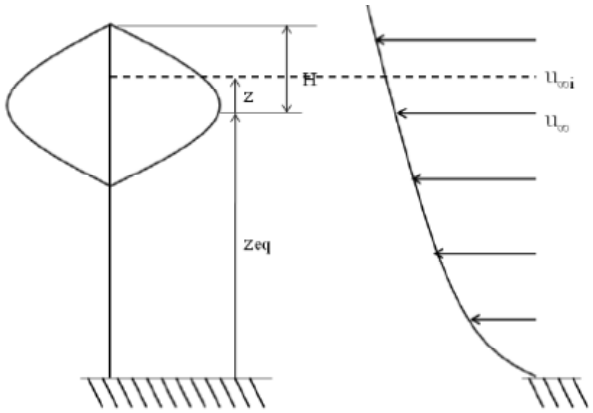

Figure 1. VAWT with its equator at 0 meters from the ground. The wind velocity at the equator is taken as the reference, u_∞ with $u_{\infty i}$ the wind velocity at different heights

Actuator Disk Theory (ADT)

The ADT models the rotor as a uniform 1-D thin disk, with uniform velocity at the disk. The velocity across the disk is continuous whereas the pressure is discontinuous.

The incompressible Bernoulli equation is applied separately to each side of the actuator disk, with the axial force acting on the actuator disk given in Equation 1.

$$F_a = 2\dot{m}(u_\infty - u_1). \tag{1}$$

Another relation is defined for the axial force coefficient, Equation 2.

$$F_a^\dagger = \frac{F_a}{\frac{1}{2}\rho u_1^2 S}. \tag{2}$$

Combining Equations 1 and 2 results in the velocity relationship of Equation 3.

$$\frac{u_\infty}{u_1} = 1 + \frac{1}{4}F_a^\dagger. \tag{3}$$

The axial force F_a can also be determined from Blade Element Theory BET. Equating the two expressions for F_a enables the interference factor a to be determined, Equation 4.

$$u_1 = (1 - a)u_\infty. \tag{4}$$

Knowing the reduced axial velocity, the rotational speed, ω, and the corresponding lift and drag characteristics enables the torque and power generation to be calculated. The incompressible Bernoulli equation requires the streamtube to expand when passing through an actuator disk because the velocity decreases, Figure 3. However, for simplicity, all streamtubes are assumed to pass straight through the actuator disks. These streamtubes are also taken to be independent of each other. Other assumptions include quasi-steady flow with no secondary flow effects.

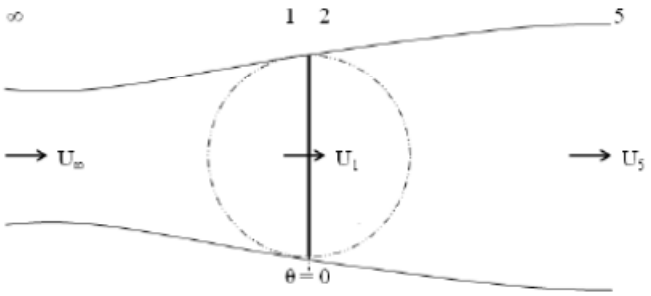

Single Actuator Disk

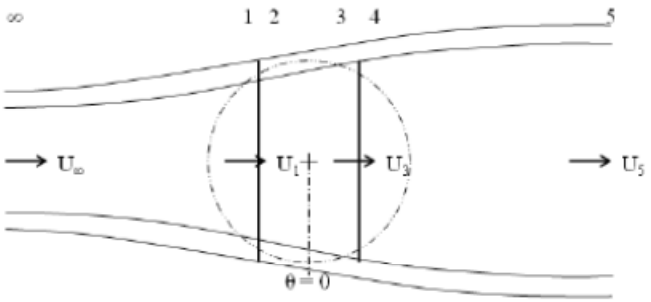

Double Actuator Disk

Figure 3. Streamtube expansion and arbitrary actuator disks within rotor revolution path.

Blade Element Theory (BET)

In BET, a rotor blade is discretized into individual blade elements, Figure 4. Aerodynamic forces acting on these blade elements are determined from Equations 5 and 6 and the corresponding lift and drag coefficients (C_L and C_D), where C_N and C_T are the normal and tangential components as a result of C_L and C_D, Figure 5. It is assumed that the airfoil is two-dimensional and the chord length is small relative to the distance traveled in a rotor revolution.

$$C_N = C_L \cos\alpha + C_D \sin\alpha \tag{5}$$

$$C_T = C_L \sin\alpha - C_D \cos\alpha \tag{6}$$

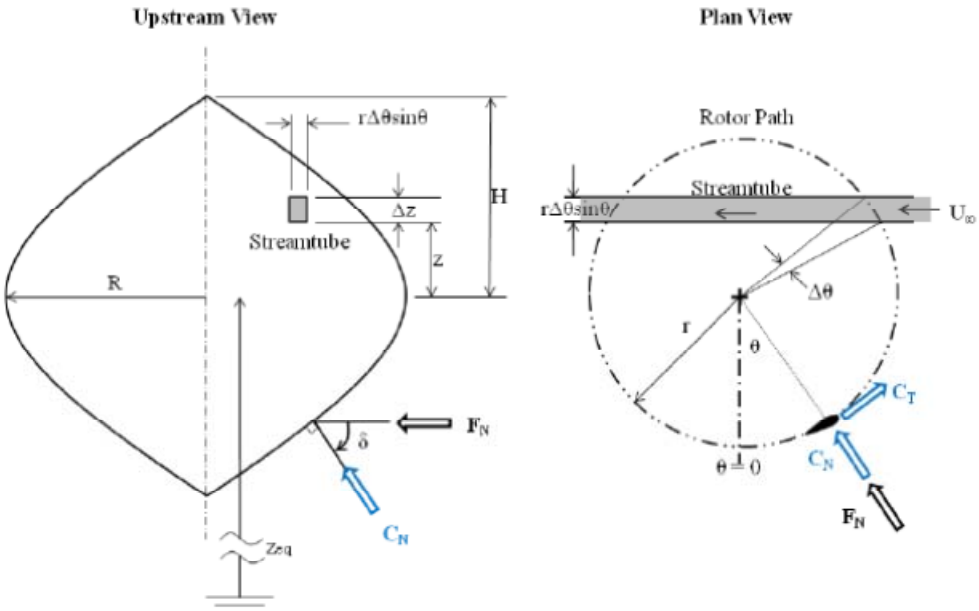

Figure 4. Schematic of a streamtube passing through the VAWT.

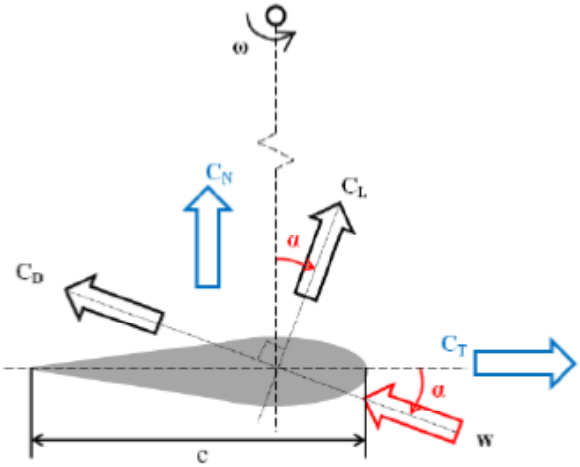

Figure 5. Directional convention of aerodynamic force coefficients.

In BET, the elemental forces are determined based on

$$dF_N = \frac{C_N q c}{\cos\delta} dz \tag{7}$$

$$dF_T = \frac{C_T q c}{\cos\delta} dz \tag{8}$$

where $q = (1/2)\rho w^2$ is the local relative dynamic pressure and δ is the angle between normal to the blade and the horizontal axis, Figure 4.

The normal and tangential component of the forces acting on these individual blade elements are summed to determine the total force experienced by the rotor in these respective directions. The angle of attack α is determined based on the blade geometry and θ, Figure 6. α and the corresponding wind relative velocity, w can be expressed as

$$\alpha = \tan^{-1}\left(\frac{\sin\theta\cos\delta}{\frac{r\omega}{u_1} + \cos\theta}\right) \tag{9}$$

$$\left(\frac{w}{u_1}\right)^2 = \left(\frac{r\omega}{u_1} + \cos\theta\right)^2 + (\sin\theta\cos\theta)^2 . \tag{10}$$

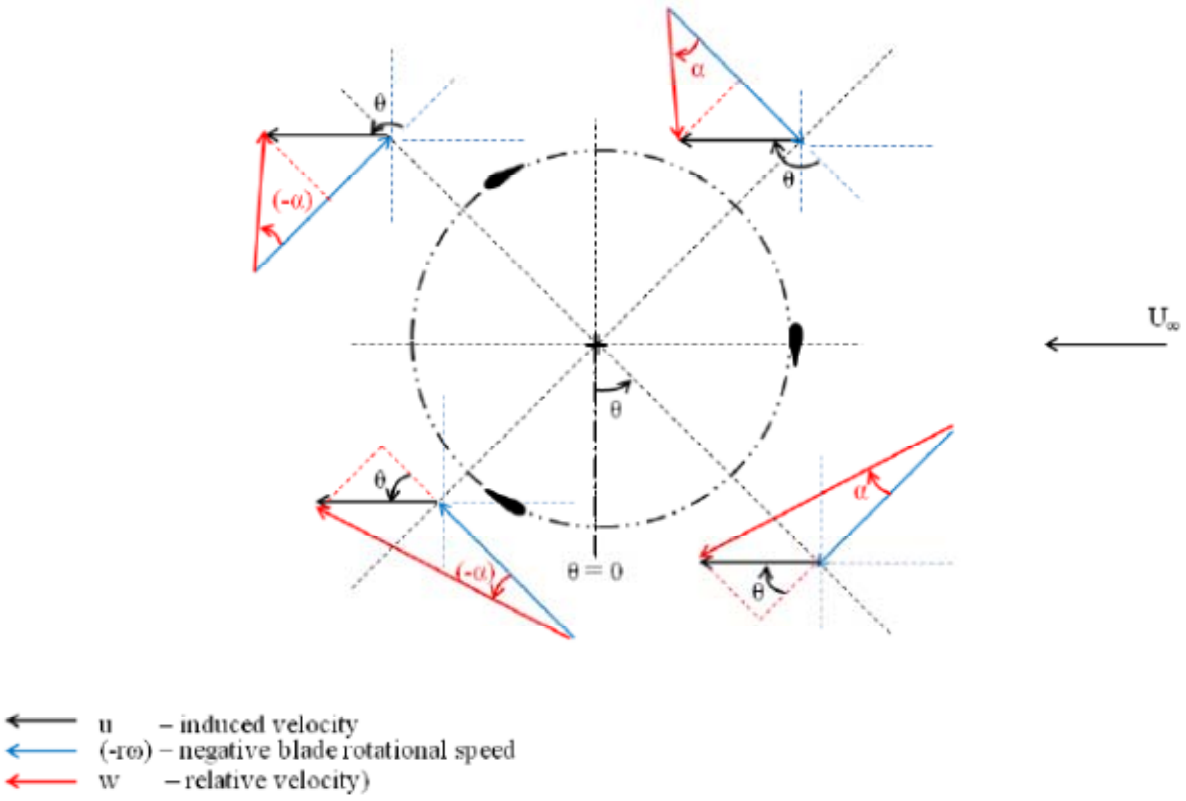

Figure 6. Velocity triangles and the corresponding sign of α.

Single Streamtube (1S)

The model assumes that the flow traverses a VAWT rotor with one single streamtube with uniform velocity. Hence the interference factor, a is constant over the actuator disk. a provides information about the local wind velocity at the actuator disk which is then used to determine the resulting forces. Both a and the forces acting on the actuator disk are unknowns. Instead of guessing a, the 1S model guesses the specific velocity $r\omega/u_1$ so that α, w, and other following performance parameters are immediately determined. The tip speed ratio is determined at the end.

Blade Element Theory (BET)

Equations 7 and 8 are combined to calculate the forces acting on the rotor in the axial direction, which is the effective force in the direction of the wind.

$$dF_a = qc(C_N \sin\theta - C_T \frac{\cos\theta}{\cos\delta})dz, \tag{11}$$

The total axial force is determined by double integration of Eq. 11 for a complete rotor revolution ($0 < \theta < 2\pi$), and along the rotor height ($-H < z < H$),

$$F_a = \frac{Nc}{2\pi} \int_{-H}^{H} \int_{0}^{2\pi} (1/2)\rho w^2 (C_N \sin\theta + C_T \frac{\cos\theta}{\cos\delta}) d\theta dz. \tag{12}$$

For rotor blades that are symmetric in the radial direction around $z = 0$, Equation 12 reduces to

$$F_a = \frac{Nc}{\pi} \int_{0}^{H} \int_{0}^{2\pi} (1/2)\rho w^2 (C_N \sin\theta + C_T \frac{\cos\theta}{\cos\delta}) d\theta dz. \tag{13}$$

In non-dimensional terms, Equation 13 is divided by a reference $F = \frac{1}{2} u_1 S$ where the rotor swept area $S = S^+RH$. Then, the axial force coefficient becomes

$$F_a^\dagger = \frac{1}{S^\dagger \pi} \frac{Nc}{R} \int_{0}^{1} \int_{0}^{2\pi} (1/2)\rho w^2 (C_N \sin\theta + C_T \frac{\cos\theta}{\cos\delta}) d\theta d\zeta. \tag{14}$$

Before computing the power generation, F_a^+ is used to determine the tip speed ratio at the specific velocity guessed in the beginning. The tip speed ratio, Equation 15, is obtained by combining Equations 3 and 14. As a result, there is no need to determine a in the 1S model because the information was incorporated into Equation 3.

$$X_{eq} = \frac{R\omega}{u_\infty} = \frac{R\omega}{u_1} \left(\frac{1}{1 + \frac{1}{4} F_a^\dagger} \right) \tag{15}$$

Once the tip speed ratio is determined, the corresponding power coefficient is computed. First, integrating the product of local radius and Equation 8 over the rotor span and around the revolution gives the effective torque experienced by the rotor blade, Equation 16

$$T = \frac{Nc}{2R}\int_{-H}^{H}\int_{0}^{2\pi}\frac{C_T q r c}{cos\delta}d\theta dz. \tag{16}$$

The power P produced by the VAWT due to the torque it experiences is then the product of T and the angular speed ω. The power coefficient is a non-dimensional parameter defined as the ratio of actual power output over the maximum possible power available P_{max} for a given rotor swept area, Equation 17, with the power coefficient, C_P given in Equation 18.

$$P_{max} = \frac{16}{27}\left(\frac{1}{2}\rho u_\infty S^\dagger\right). \tag{17}$$

$$C_P = \frac{P}{P_{max}} = \frac{27}{8}\frac{1}{2S^\dagger\pi}\frac{Nc}{R}X_{eq}\int_0^1\int_0^{2\pi}\left(\frac{u_1}{u_\infty}\right)^2\frac{\eta C_T}{cos\delta}d\theta d\zeta. \tag{18}$$

Multiple Streamtube (MS)

The MS model is developed from the single streamtube model. Figure 2.4 illustrates one of the streamtubes passing the VAWT actuator disk. In the 1S model, a specific velocity $r\omega/u_1$ is guessed, and the actual tip speed ratio, $r\omega/u_\infty$ determined. In the MS model, $r\omega/u_\infty$ is guessed and iterated until a desired accuracy is achieved. Given the same initial guess at each blade element, the iteration allows variations in a over the area swept by the rotor blade. Convergence is usually rapidly achieved, with more iterations closer to the equator. This model allows vertical variation of wind velocity and assumes that the streamtubes are independent.

Equating Equations 1 and 12 yields the following equation for the MS.

$$\frac{Nc}{\pi}\int_{-H}^{H}\int_0^{\pi}(1/2)\rho w^2(C_N\sin\theta + C_T\frac{\cos\theta}{\cos\delta})d\theta dz = 2\rho\int_{-H}^{H}\int_0^{\pi}u_1(u_{\infty i}-u_1)r\sin\theta d\theta dz. \tag{19}$$

The $d\theta$ and dz integrals are simplified as $\Delta\theta$ and Δz as a result of the discrete blade elements, Equation 20.

$$\frac{Nc}{R}\frac{1}{2\pi}\left(\frac{w}{u_{\infty i}}\right)^2(C_N + C_T\frac{\cos\theta}{\sin\theta\cos\delta})\Delta\theta\Delta z = 2\frac{u_1}{u_{\infty i}}(1-\frac{u_1}{u_{\infty i}})\eta\Delta\theta\Delta z. \tag{20}$$

Further simplification of Equation 20 reduced to Equation 21

$$\frac{s}{4\pi\eta}\left(\frac{w}{u_{\infty i}}\right)^2(C_N + C_T\frac{\cos\theta}{\sin\theta\cos\delta}) = (1-a)a. \tag{21}$$

Representing the left side of Equation 21 by F^*_a, Equation 22 is developed and used to iterate for the interference factor.

$$a = F^*_a + a^2, \tag{22}$$

The initial guess of a is chosen as unity, implying that the induced velocity is the same as the incoming velocity. The value is typical close to unity near the edge. As a result of the

iteration, the values of C_T and w are also refined and used to determine the torque experience by each blade element.

The elemental torque is determined using Equation 23

$$T = \frac{1}{2}\rho r C_T \frac{c\Delta h}{\cos\delta} w^2. \tag{23}$$

Summing the elemental torques along the height and around the half rotor revolution yields the average torque experience by N blades of the VAWT,

$$\bar{T} = \frac{N}{N_t}\sum_{1}^{Nt}\sum_{1}^{Ns} T. \tag{24}$$

The power coefficient is then determined, Equation 25.

$$C_P = \frac{\omega\frac{N}{N_t}\sum_{1}^{Nt}\sum_{1}^{Ns}\frac{1}{2}\rho C_T w^2 \frac{rc\Delta h}{\cos\delta}}{\frac{1}{2}\rho\sum_{1}^{Ns} 2r\Delta h u_\infty^3}, \tag{25}$$

where N_s is the number of blade elements in the ζ direction, and N_t is the number of blade element counts around the rotor revolution.

Double Multiple Streamtube (DMS)

Applying Equation 19 around a complete rotor revolution results in Equation 26,

$$\frac{Nc}{2\pi}\int_{-H}^{H}\int_{0}^{2\pi}(1/2)\rho w^2(C_N\sin\theta + C_T\frac{\cos\theta}{\cos\delta})d\theta dz = 2\rho\int_{-H}^{H}\int_{0}^{\pi} u_1(u_{\infty i}-u_1)r\sin\theta d\theta dz. \tag{26}$$

Simplification of Equation 26 leads to,

$$\frac{s}{8\pi R}\int_0^{2\pi}\left(\frac{w}{u_1}\right)^2\left(\frac{u_1}{u_{\infty i}}\right)^2(C_N + C_T\frac{\cos\theta}{\sin\theta\cos\delta})d\theta = \int_0^{2\pi}(1-a)a\eta d\theta,$$

$$\int_0^{2\pi} f(\theta)(1-a_1)d\theta = \int_0^{2\pi} K\eta a_1\sin\theta d\theta,$$

$$a_1 = \left(1 + \frac{KK_0\eta}{\int_0^{2\pi} f(\theta)d\theta}\right)^{-1} \tag{27}$$

$$K = \frac{8\pi R}{Nc},\ K_0 = \cos\theta + \frac{\Delta\theta}{2} - \cos\theta - \frac{\Delta\theta}{2},\ f_1(\theta) = (\frac{w_1}{u_1})\left(C_{N1} + C_{T1}\frac{\cos\theta}{\sin\theta\cos\delta}\right).$$

Similarly for downstream, the interference factor is

$$a_3 = \left(1 - \frac{K K_0 \eta}{\int_0^{2\pi} f(\theta) d\theta}\right)^{-1} \tag{28}$$

$$f_3(\theta) = \left(\frac{w_3}{u_3}\right)\left(C_{N3} + C_{T3}\frac{\cos\theta}{\sin\theta\cos\delta}\right).$$

Equations for w/u_3 and α also change depending on a_3. The negative sign is due to the reversed flow direction. The upstream actuator disk accepts wind from far upstream, whereas the downstream one receives flow from within the turbine.

The elemental normal and tangential forces can be expressed as

$$dF_{N1} = \frac{1}{2}\rho w_1^2 C_{N1}\left(\frac{cdz}{\cos\delta}\right) \tag{29}$$

$$dF_{T1} = \frac{1}{2}\rho w_1^2 C_{T1}\left(\frac{cdz}{\cos\delta}\right). \tag{30}$$

Integrating the above, the total normal and tangential forces are then be expressed in terms of the non-dimensional parameters, Equations 31 and Equation 32

$$F_{N1}^{\dagger} = \frac{cH}{S}\int_{-1}^{1} C_{N1}\left(\frac{w_1}{u_\infty}\right)^2 \frac{1}{\cos\delta} d\zeta \tag{31}$$

$$F_{T1}^{\dagger} = \frac{cH}{S}\int_{-1}^{1} C_{T1}\left(\frac{w_1}{u_\infty}\right)^2 \frac{1}{\cos\delta} d\zeta \tag{32}$$

$$S = S^{\dagger} RH.$$

The constant, S^+ depends on the rotor blade profile. For instance, for a straight blade with R/H = 1, then S = 2RH. Numerical integration is applied to Equation 31 and 32, and the integrands assumed to be constants at each blade element because they are not direct functions of ζ. From Equation 30, the torque is determined for a single actuator, $T_1(\theta)$, in non-dimensional terms

$$T_1(\theta) = \frac{1}{2}\rho c R H \int_{-1}^{1} C_{T1} w_1^2 \left(\frac{\eta}{\cos\delta}\right) d\zeta$$

and applied to the upstream actuator disk power coefficient

$$C_{p1} = \frac{N}{2\pi}\frac{cH}{S} X_{eq} \int_0^{\pi}\int_{-1}^{1} C_{T1}\left(\frac{w_1}{u_\infty}\right)^2 \left(\frac{\eta}{\cos\delta}\right) d\zeta d\theta. \tag{33}$$

Similarly for the downstream actuator disk with the corresponding C_{T3}, C_{N3} and ω_3 values. The effective power coefficient of the VAWT is the sum of both upstream and downstream actuator disk power coefficients,

$$C_P = C_{p1} + C_{p2}. \tag{34}$$

VAWTGUI

VAWTGUI is an interactive MATLAB interface used in the prediction of the performance of VAWTs based on the MS and DMS models developed in MATLAB. Figure 7 shows the resultant GUI developed with MATLAB. The program is called VAWTGUI, and it can be categorized into four panels.

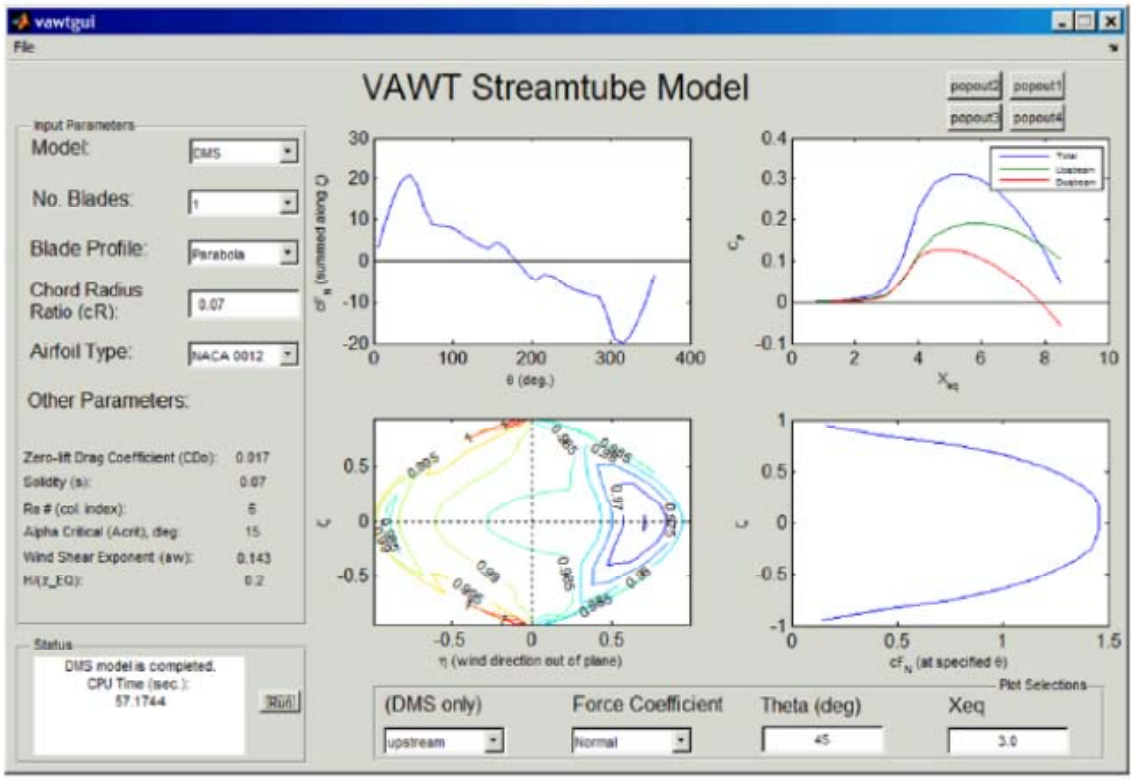

Figure 7. VAWTGUI layout.

Input Parameters

There are five options that can be changed frequently, most of which are restricted to a few drop down options. The first option is the selection between the MS or the DMS model. The MS model is only able to deliver two of the four possible plots in the display. Next is the number of blades. Only up to three blades are available because they are the most commonly found VAWT designs. Options to apply more blades could easily be added. However, caution must be taken with the plotting commands. The following selection is the rotor blade's vertical profile, with two default shapes available. In addition, there is an option to insert a user defined blade profile based on coordinates specified in the text file *input profile:txt*. The input format is shown

in the example below, where line 1 is the surface area constant, S^+, which is the ratio of the actual rotor swept area to the product of R and H.

$$\begin{array}{llll} line1 & 2.0 & & \\ line2 & 0.05 & 1.0 & 0.0 \\ \vdots & \vdots & \vdots & \vdots \end{array}$$

Consequently, the two default shapes also have their own S^+ values. Beginning from line 2 to the end of the file are coordinate points that composes a user-defined profile shape. From the first to the third column are ζ, η, and δ respectively. When this option is selected, the number of coordinate points specified in *input profile:txt* is not affected by *input gui:txt* as N_s is assigned as the number of coordinate points read.

The fourth selection is the ratio of chord length to the largest radius R. Lastly, the fifth is the airfoil type. NACA 0012, NACA 0015 and NACA 0018 are the three default airfoils available. These airfoil data are found in the text _les with the naming convention *naca00xxlif t:txt* (lift coefficient) or *naca00xxdrag:txt* (drag coefficient). Each of these text _les has eleven columns and data. The first column is the angle of attack α, ranging from 0 to 360 degrees. The remaining columns are the lift or drag coefficients based on different Reynolds number values. From column two to eleven, the Reynolds numbers are, multiplied by 10^6, 0.01, 0.02, 0.4, 0.8, 1.6, 3.6, 0.7, 1.0, 2.0, 5.0 and 10.0.

There are a few variables listed below which cannot be changed from the GUI interface. These variables would typically remain constant when studying the performance of different turbines. Solidity is the product of number of blades and the chord radius ratio, while the rest were extracted from an input text file called *input gui:txt.* The order of input within the text file is listed as follows.

- N_s - Number of blade element nodes in the direction of ζ
- N_c - Number of tip speed ratios to evaluate
- Re_i - Column index number in the airfoil data text file, indicating the corresponding Reynolds number. $Re_i = 1$ begins from column 2 in the text file
- A_{crit} - Critical angle of attack, under which the zero-lift drag coefficient is considered
- incr - Increment used when sampling Nc tip speed ratios
- C_{D0} - Zero-lift drag coefficient
- *aw* - Wind shear exponent, assuming the wind velocity profile followed a power law function
- *Hz* - The ratio of the turbine height to the height measured from the ground to the turbine equator (half height)

All five selections under the *Input Parameter* panel can only be modified before program execution.

Status

The status panel consists of a *Run* push button, and a display text box. The program is run when the *Run* button is clicked, or when the MATLAB file *vawtgui:m* is executed on the command window. Once the program is run, no changes in the status text box until the program is terminated. If the model is run successfully, the display indicates its completion with the CPU run time. Otherwise, it prompts the user to check the MATLAB command window for errors.

Plot Displays

Upon completion of the streamtube model calculations, the results are displayed on the four plot axes. The corresponding plots are as follows, clockwise from top right:

- Power coefficient (C_p) vs. tip speed ratio (X_{eq})
- ζ vs. individual force coefficient (cF_N or cFT) at a specified angular location (θ)
- Contour plot of the interference factor (a). Option to change to display both surface and contour plots.
- Sum of force coefficient (cF_N or cFT) along ζ vs. angular location θ

On the top right corner are four push buttons corresponding to the location of the four plots. These are pop-up buttons, which enable plots to be displayed as standalone windows. The MS model is only able to deliver results for the first and third plots.

Plot Selections

Once the model is completed, the Plot Selection panel enables the results to be displayed based on four different selections. These options are the up-/downstream contour plot, the normal/tangential force coefficients, θ and X_{eq}. The values of θ and X_{eq} entered must correspond to the exact array values used in the calculations. If within the program, θ = [5, 15, 25, …], then entering θ = 12 will result in a blank plot because no result is available for that input. The same applies to X_{eq}.

Functions & Subroutines

VAWTGUI is a MATLAB GUI run by two files, *vawtgui:m* and *vawtgui:f ig*. While *vawtgui:f ig* is where the layouts are built, Figure 7, all coding pertaining to the streamtube models are called as subroutines from *vawtgui:m* in Figure 8.

Vawt.m is the main program that performs the streamtube models. Within *vawtgui.m, vawt.m* is equivalent to a subroutine. The program begins by selecting whether to implement the MS or DMS model. For the MS model, the program begins with a loop running through the values of tip speed ratios. Then, it is followed by inner loops of either azimuth angle or vertical location where their sequence does not matter. The purpose of these loops is to iterate for the interference factor *a*, and other corresponding values at a specific blade element location. This is done by calling the function *findfx.m* in a while loop until the interference factor is converged. The final interference factor and other matching variables are then used to determine the power coefficient of the VAWT. For the DMS model, the same process is done separately for the up- and downstream actuator disks. The force coefficients are determined explicitly in DMS before being used to calculate the power coefficients. The resultant power coefficients for the up- and downstream actuator disks are added together to give the effective the power coefficient.

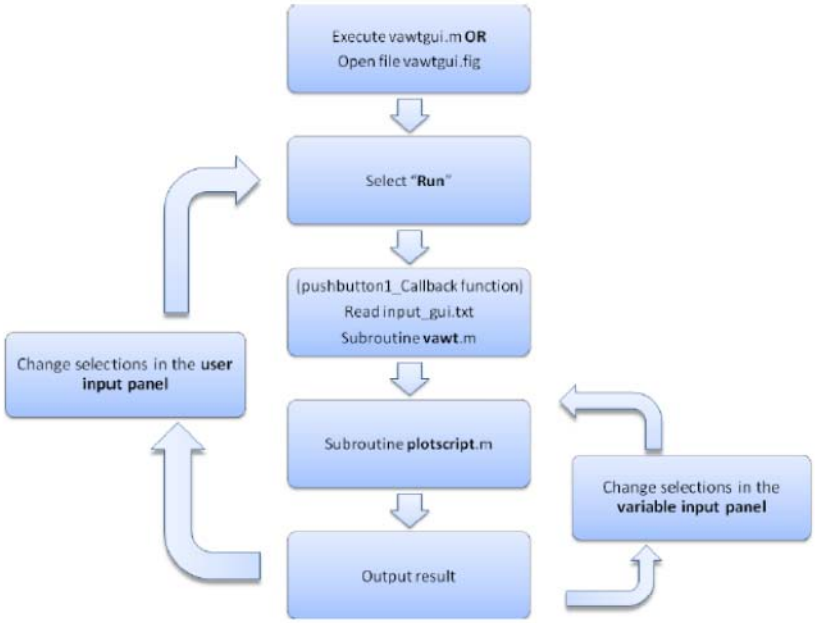

Figure 8. Execution process of VAWTGUI.

Findfx.m is a function that determines the interference factor at a given blade element location. It first determines the angle of attack, the relative velocity, and the relevant lift and drag properties of the airfoil. Depending on whether it was called from MS, DMS or *findFNFT.m*, the subsequent results are delivered. *Findfx.m*'s application in MS and DMS model is as part of the iteration procedure to determine the interference factor. However, its application in *findFNFT.m* is to apply the values from MS and DMS to determine the matching force coefficients. The reason for calculating the airfoil lift and drag properties again is that, saving the values as a vector slowed the iteration process in MS and DMS. It was more efficient to recalculate them in the search for the force coefficients.

FindFNFT.m is a function that determines the force coefficients at a given blade element location. Within the function itself, numerical integration along the vertical direction of the subsequent blade element is carried out. The function itself is called three times for a given blade element, at $\theta - \Delta\theta/2$ and $\theta + \Delta\theta/2$.

Plotscript.m is another subroutine within vawtgui.m that performs the plotting function. It is called immediately upon completion of either the MS or DMS model. It also serves to update plots when selections are changed within the variable parameter panel. Part of *plotscript.m* is hard coded to enable results for only one, two or three bladed VAWTs to be displayed. For turbines with more than one rotor blade, the results from the additional blades are simply a phase shift from the first by the angular distance between them. The resultant contribution from all the blades is done through superposition.

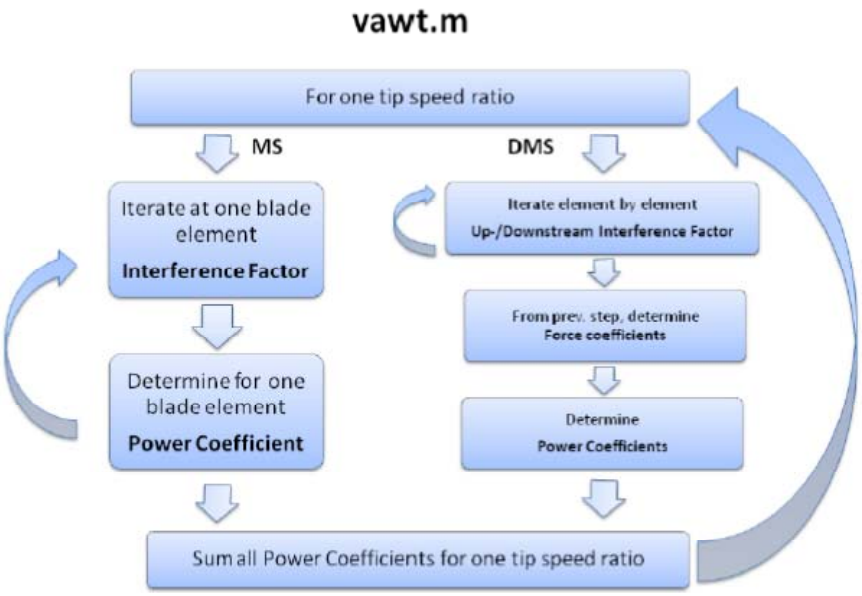

Figure 9. Execution process of vawt.m.

Then, numerical integration is carried out in the angular direction (Figure 10). The integration method used is Simpson's method.

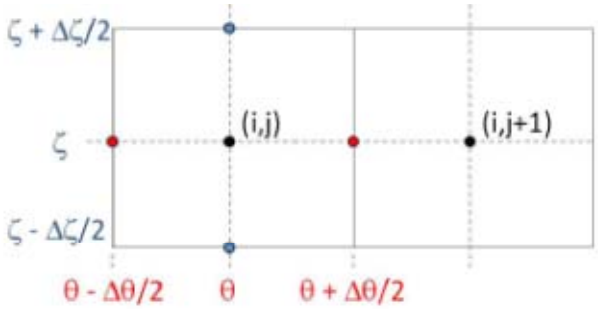

Figure 10. A grid representation of two blade elements, where the nodes (i,j) and (i,j+1) were located at the center of the elements. The red dots were pseudo-nodes for integration at (i,j) along the angular direction, whereas the blue dots were that in the direction of ζ.

RESULTS

The performance trends predicted using VAWTGUI is presented to demonstrate the results. Various aspects of the VAWT are compared with the following reference case.

Reference Case

Model	DMS
Blades	1
Profile	Parabola
Chord Radius Ratio (c/R)	0.07
Airfoil	NACA 0018

Power Coefficient vs. Tip Speed Ratio

The overall performance trends of a VAWT can be represented by the power coefficient versus the tip speed ratio (C_P vs. X_{eq}). The maximum power coefficient of the reference case occurs at 5:0 < X_{eq} < 6:0 for both MS and DMS model. However, the MS model only assumed one actuator disk and resulted in an under-estimation of the work extraction, Figure 11. Therefore, the DMS provides a better prediction of VAWT performance.

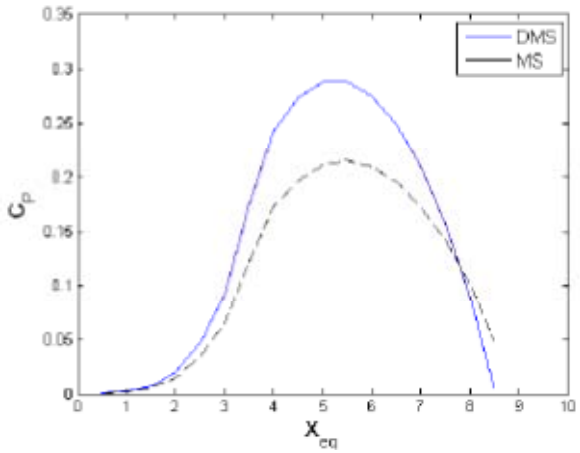

Figure 11. Comparison between reference case and MS model.

VAWTs are frequently found in a three-bladed configuration. Figure 12 shows increased maximum power coefficient achievable with 3-bladed VAWTS. As a result, greater power extraction is possible at the optimum tip speed ratio. This optimum tip speed ratio is, however, lower than that of the one-bladed configuration. Consequently, the operational domain of tip speed ratios also decreased with more blades, Figure 12.

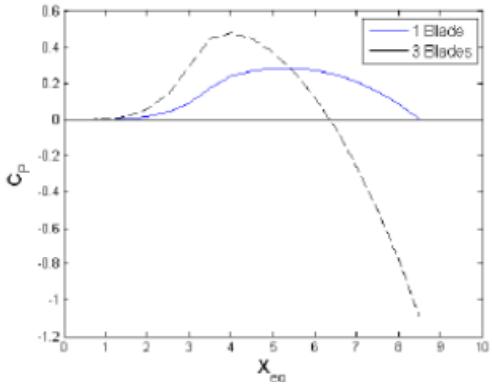

Figure 12. Comparison between reference case and 3-bladed parabolic rotor VAWT.

Figures 13 and 14 illustrate the one period variation of the forces acting on the rotor blade for the reference case and the straight blade rotor. The periodic behavior is very similar for these two rotors, with the straight blade rotor having a larger magnitude forces.

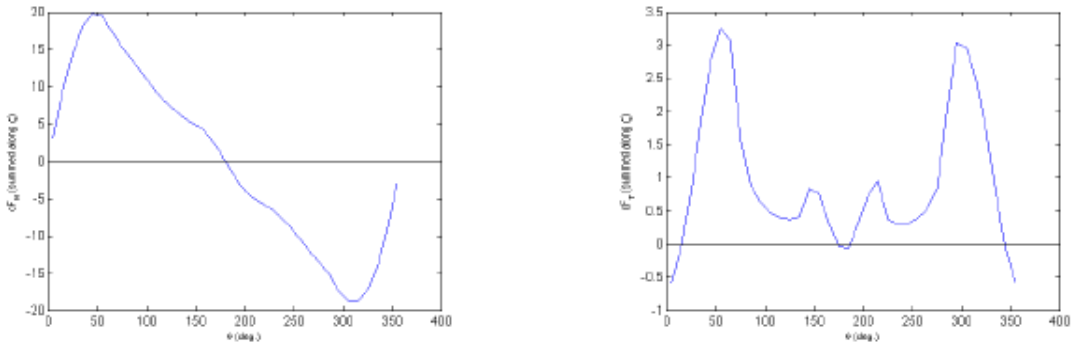

Normal Tangential

Figure 13. Force coefficient (periodic): reference case at X_{eq} = 3:0.

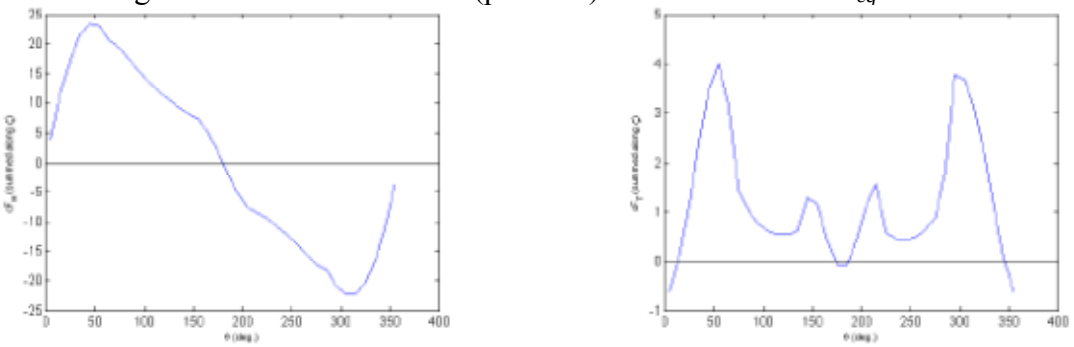

Normal Tangential

Figure 14. Force coefficient (periodic): straight rotor blade at X_{eq} = 3:0.

The force coefficients vary in both the positive and negative region. In the perspective of F_N^+, the rotor blade experiences force acting inward and outward during a revolution. On the other hand, F_T^+ also acts both against and for the direction of rotation. When acting against the rotation, the VAWT generates a counter torque that decelerates the rotor. It is possible to reduce the time in a revolution where the rotor experiences counter torque. This is done with a three-bladed rotor operating at higher tip speed ratios. Multiple rotor blades increase the overall force acting on the VAWT, but not enough to eliminate the counter torque. Figure 15 shows that at higher tip speed ratios, the force coefficients were maintained in the positive region throughout the revolution.

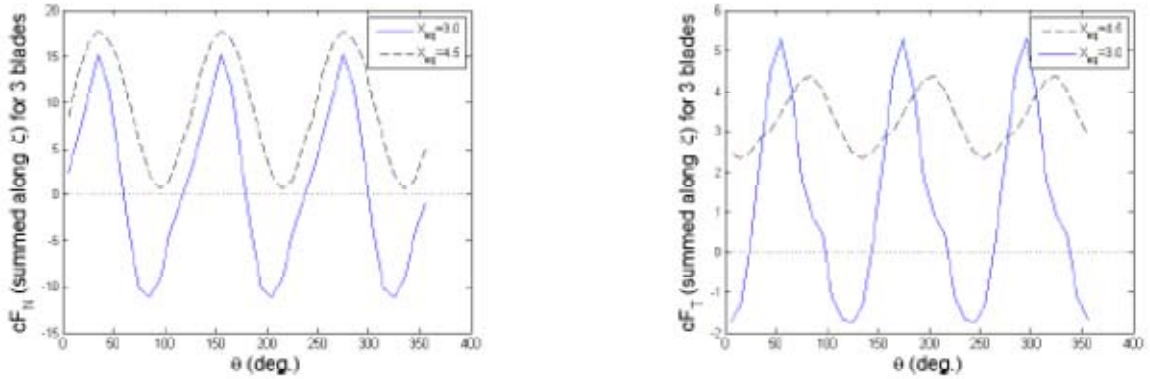

(a) Normal (b) Tangential

Figure 15. Combined force coefficient from three rotor blades (periodic) at different X_{eq} values.

APPENDIX B. Urban Wind Simulation at Purdue Calumet

Model Description:

The CFD modeling starts with geometry model construction. Based on geometry model computational meshes will be generated. Then the input condition and boundary conditions will be applied to the CFD model. After running the CFD models, numerical results will be obtained. Numerical results will then be validated with experimental data. Once the accuracy of the simulation results is checked to be acceptable, post-processing of the results can be developed. Figure 1 shows the numerical modeling flowchart.

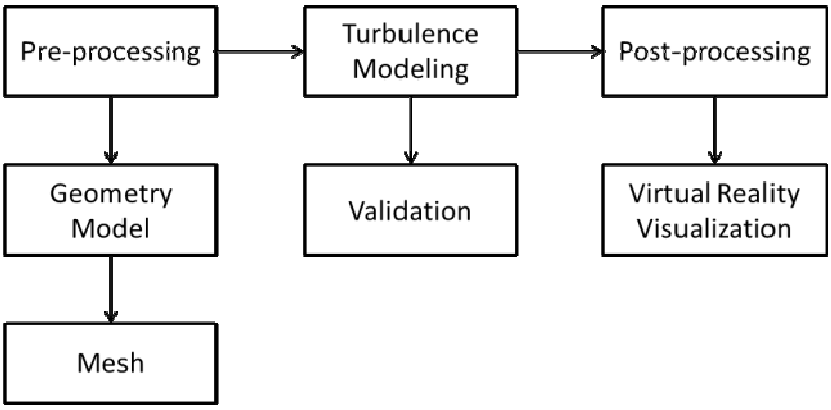

Figure 1. Numerical Modelilng Flowchart

Pre-processing: GAMBIT© was used to build the 3-D geometry. Student Union and Library building (SUL) located at Purdue University Calumet campus is the target building for assessing the wind condition, constructing the 3-D wind fields, and siting the VAWT. In order to considering the neighboring building effects for urban wind environment, all the nearby buildings along with SUL are modeled. The geometry for the simulation is shown in Figure 2.

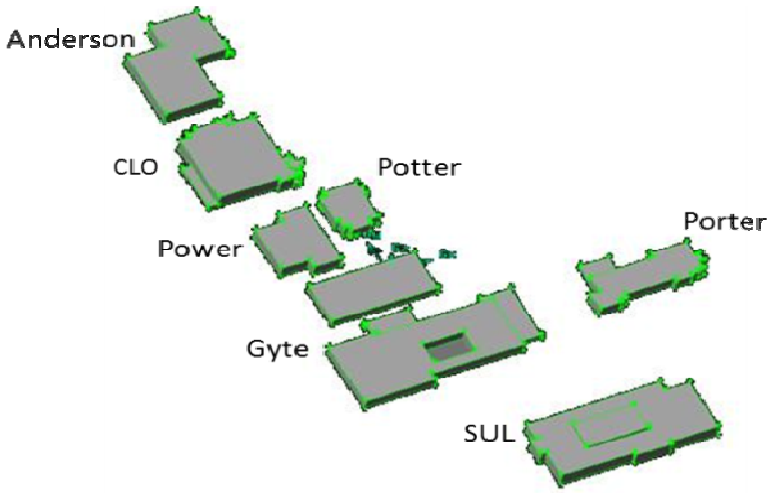

FIGURE 2. BIRD'S-EYE VIEW OF THE GEOMETRY MODEL

By using GAMBIT©, computational meshes can be generated. Mesh size function was also applied in order to get finer mesh elements round the focus at the same time keep the total elements number under the computer memory capacity limit. Mesh independent study was

carried to prove the results are independent of mesh scale. The mesh scales were 3,254,051, 3,980,159 and 4,591,782, and were used to prove that the results were independent of the mesh scale. Final mesh selected for the simulation was 3,254,051.

Turbulence Modeling: The k-epsilon turbulence model was adopted as flow solver because it has been extensively tested and calibrated for flows around bluff bodies and structures. Incompressible flow was chosen as material type. Although air is compressible in reality, in the simulation it was set as incompressible flow based on the assumption that the density is not correlated with the wind speed. The error introduced by this assumption on a constant pressure surface is less than 5%. In order to represent the high wind energy area more vividly, a set of User Defined Function (UDF) codes were input into FLUENT© in the simulation. UDF was employed to define the inlet velocity profile that is applied to the inlet surfaces of the test domain as initial condition. After the simulation is converged, run a paragraph of UDF code to calculate WPD in the test domain.

The wind directions with the higher probability were chosen as the prevailing winds for the simulation from statistical analysis by using Weibull and Rayleigh distribution.. Northeast, West-southwest and their relevant wind speeds were applied separately as input wind conditions for two CFD simulation cases of 3-D suburban wind flows over buildings on the PUC campus.

Simulations were considered as converged when the residual for momentum, energy are less than 10^{-6}. Validation was achieved by comparing the simulation results with the wind data recorded by the sensor on top of the SUL building. Ten cases with different input wind data were calculated to do validation. Selected two test cases are listed in Table 1 and 2. The error range is 0.91% to 13.67%. Based on the validation cases, the overall simulation results were acceptable.

TABLE 1 VALIDATION RESULTS FOR CASE 1

9/17/2011 9:24	Sensor 1		Sensor 2		Sensor 3	
Measurement	3.31 m/s	126°	3.00 m/s	120°	3.04 m/s	126°
Simulation Result	3.34 m/s	120°	3.41 m/s	114°	3.43 m/s	121°
Error	0.91%	4.76%	13.67%	5.00%	12.83%	3.97%

TABLE 2 VALIDATION RESULTS FOR CASE 2

10/15/2011 15:59	Sensor 1		Sensor 2		Sensor 3	
Measurement	5.05 m/s	282°	4.73 m/s	125°	4.25 m/s	131°
Simulation Result	5.27 m/s	290°	4.98 m/s	132°	4.51 m/s	134°
Error	4.36%	2.84%	5.29%	5.6%	6.12%	2.29%

Post-processing Post-processing was first generated by ParaView, which is a multi-platform data analysis and visualization application. ParaView can be used to quickly build visualizations to analyze data. The data exploration can be done interactively in 3-D. For this thesis, some 3-D fluid data exploration of wind velocity magnitude, turbulence intensity and WPD were shown by streamlines, contour plots, and cutting planes which all obtained by ParaView. 3-D visualization

results were displayed in the immersive VR system. Users watch the streamline around the buildings on all aspects by using a controller to achieve that walking, flying, rotation about all 3 axes. Furthermore, flowing vectors can simulate the moving action of wind, providing insights on direction and magnitude.

Governing equations for turbulent model

Transport equations for standard k -epsilon model:

for turbulent kinetic energy k

$$\frac{\partial}{\partial t}(\rho k) + \frac{\partial y}{\partial x_i}(\rho k u_i) = \frac{\partial}{\partial x_j}\left[\left(\mu + \frac{\mu_t}{\sigma_k}\right)\frac{\partial k}{\partial x_j}\right] + P_k + P_b - \rho\epsilon - Y_M + S_k \quad (1)$$

for dissipation ϵ

$$\frac{\partial}{\partial t}(\rho\epsilon) + \frac{\partial y}{\partial x_i}(\rho\epsilon u_i) = \frac{\partial}{\partial x_j}[\left(\mu + \frac{\mu_t}{\sigma_\epsilon}\right)\frac{\partial \epsilon}{\partial x_j}] + C_{1\epsilon}\frac{\epsilon}{k}(P_k + C_{3\epsilon}P_b) - C_{2\epsilon}\rho\frac{\epsilon^2}{k} + S_\epsilon \quad (2)$$

where μ_t is turbulent viscosity,

P_k is the generation of turbulence kinetic energy due to the mean velocity gradients,

S is the modulus of the mean rate-of-strain tensor,

P_b is the generation of turbulence kinetic energy due to buoyancy,

$C_{1\epsilon}, C_{2\epsilon}, \sigma_k, \sigma_\epsilon$ are model constants. $C_{1\epsilon} = 1.44,\ C_{2\epsilon} = 1.92,\ \sigma_k = 1.0,\ \sigma_\epsilon = 1.3.$

For the calculation, the realizable k-epsilon turbulence model with the default parameters is used "since this model has superior performance for flows involving separation and predicts the spreading of planar and round jets more accurately, than the standard k-epsilon model and is reasonably fast and stable". Transport equations for realizable k-epsilon turbulence model:

for turbulent kinetic energy k

$$\frac{\partial}{\partial t}(\rho k) + \frac{\partial y}{\partial x_j}(\rho k u_j) = \frac{\partial}{\partial x_j}\left[\left(\mu + \frac{\mu_t}{\sigma_k}\right)\frac{\partial k}{\partial x_j}\right] + P_k + P_b - \rho\epsilon - Y_M + S_k \quad (3)$$

for dissipation ϵ

$$\frac{\partial}{\partial t}(\rho\epsilon) + \frac{\partial y}{\partial x_j}(\rho\epsilon u_j) = \frac{\partial}{\partial x_j}\left[\left(\mu + \frac{\mu_t}{\sigma_\epsilon}\right)\frac{\partial \epsilon}{\partial x_j}\right] + \rho C_1 S_\epsilon - C_2\rho\frac{\epsilon^2}{k+\sqrt{\vartheta\epsilon}} + C_{1\epsilon}\frac{\epsilon}{k}C_{3\epsilon}P_b + S_\epsilon \quad (4)$$

where $C_1 = \max\left[0.43, \frac{\eta}{\eta+5}\right], \eta = S\frac{k}{\epsilon}$,

$C_{1\epsilon}, C_{2\epsilon}, \sigma_k, \sigma_\epsilon$ are model constants. $C_{1\epsilon} = 1.44,\ C_2 = 1.9,\ \sigma_k = 1.0,\ \sigma_\epsilon = 1.2.$

Simulation Results

Streamlines round the building arrays are shown in Figure 3.

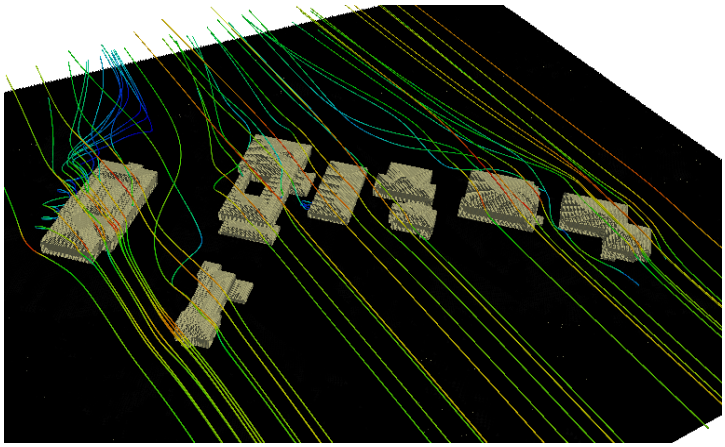

FIGURE 3 STREAMLINES AROUND BUILDINGS ON PUC CAMPUS.

Countour plots for wind velocity, turbulent intensity and WPD are shown in Figures 4 and 5.

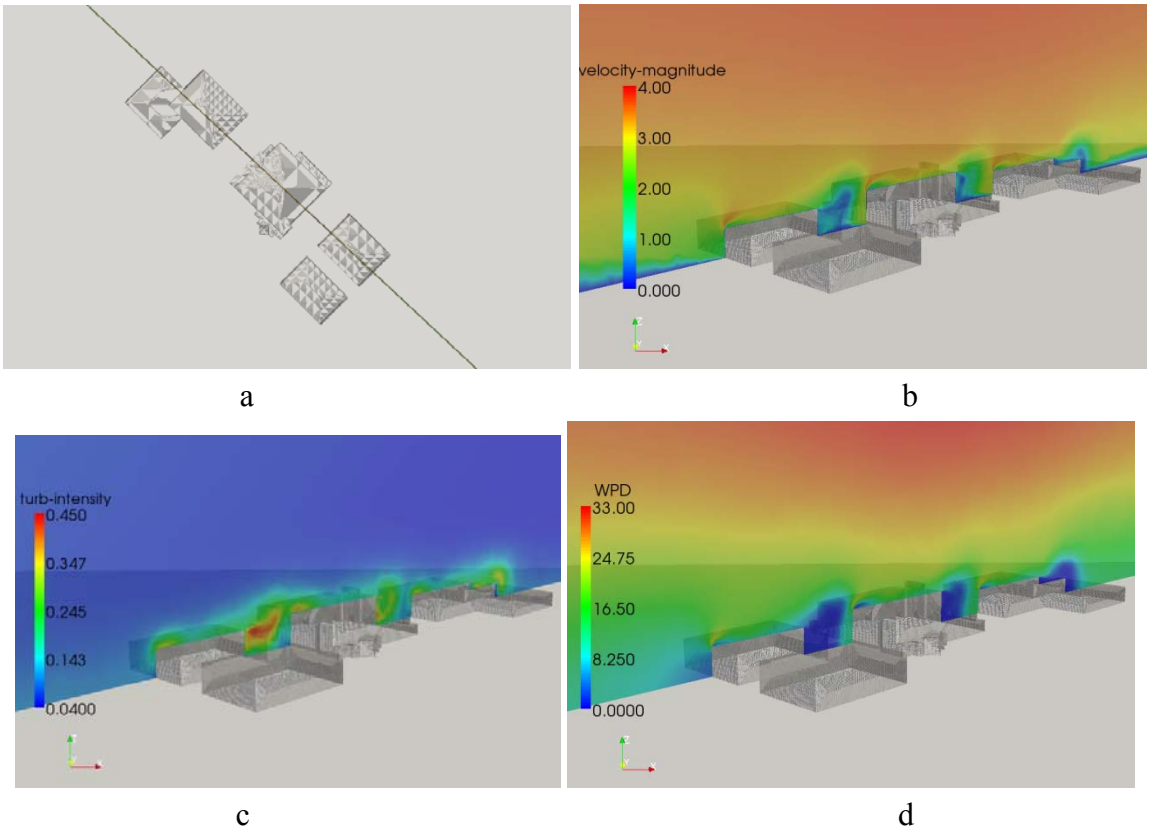

Figure 3. Side View of Contours of Wind Velocity, Turbulence Intensity and Wind Power Density on Vertical Stratifications (a) Location of the Selected Plane (b) Contours of Wind Velocity (c) Contours of Turbulence Intensity (d) Contours of Wind Power Density

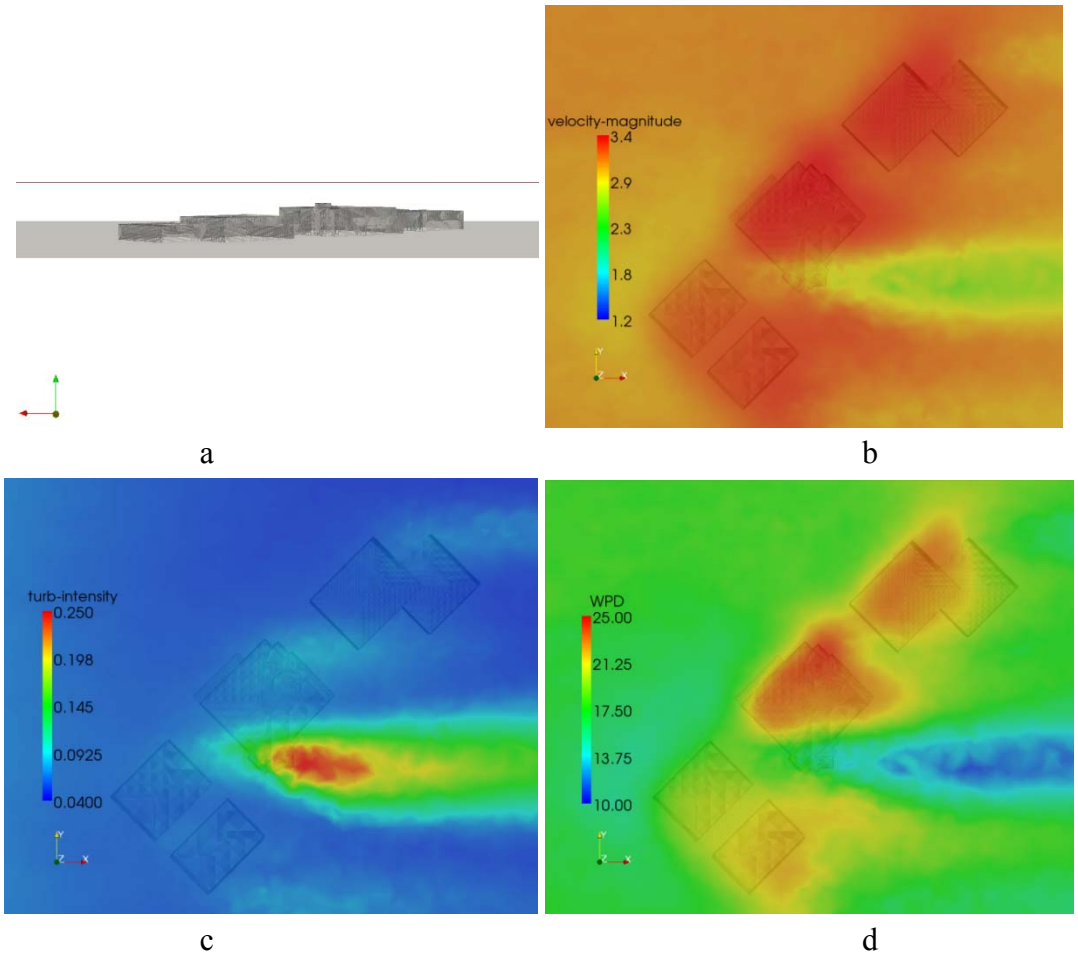

Figure 4. Top View of Contours of Wind Velocity, Turbulence Intensity and Wind Power Density on Vertical Stratifications (a) Location of the Selected Plane (b) Contours of Wind Velocity (c) Contours of Turbulence Intensity (d) Contours of Wind Power Density

APPENDIX C. Rooftop VAWT, Turbine Damage & Modal Testing

This appendix describes the vertical axis wind turbines acquired, instrumented and installed on the roof top of building at Purdue Calumet and Purdue West Lafayette (Kepner Lab) and modal dynamic testing.

An EddyGT vertical axis wind turbine (VAWT) was installed on a two meter tower on the roof of the Student Union Library Building (SUL) at Purdue Calumet, Figure 3. Two of the three anemometers used for measuring wind speed are also shown. A similar wind turbine was installed at Kepner Labs, Purdue West Lafayette.

Figure 3. Wind turbine and anemometers with vanes on roof of SUL building.

1. EXPERIMENTAL HAWT TEST APPARATUS

Modern utility-scale wind turbines are equipped with several types of sensors for monitoring the wind resource as well as mechanical and electrical variables of interest in the turbine. The performance and reliability of wind turbines are largely governed by the nature of the wind loads that act on the turbine rotor blades. The ability to characterize these loads in real time is advantageous for implementing control algorithms that increase energy capture, which is the primary short-term measure of wind turbine performance. An equally important measure of performance is long-term wind turbine reliability. Reliability is related to the structural integrity of the blade root, low speed shaft, yaw joint, and other load bearing components (Adams, White, Rumsey, & Farrar, 2011). A more complete awareness of the temporal and spatial variations in the wind loads that act upon the turbine rotor would allow operators to implement advanced control and maintenance strategies. Such information could also provide an understanding of why similar turbines in the same wind farm experience different failure patterns. The methodologies presented in this chapter characterize how the rotor forced response changes due to yaw and pitch set-point errors and how these changes affect the sensitivity of blade measurements to damage mechanisms. This understanding can be applied to improve energy capture while simultaneously facilitating turbine health management.

Literature Review: Performance Losses Due to Yaw and Pitch Control Errors

Utility-scale wind turbines are equipped with anemometers and wind vanes that are located on the nacelle behind the rotor disk to characterize inflow wind conditions. However, this measurement position is not ideal for sensing wind speed due to interference that is created by the blades and nacelle. Furthermore, the wind speed often varies across the rotor disk due to

vertical and horizontal wind shear as a result of the atmospheric boundary layer and other phenomena such as wake flow, but a single cup anemometer and wind vane positioned on the nacelle is incapable of measuring these variations. Wind direction data that is gathered by these sensors is used in part to control the yaw position, but this data yields an incomplete perspective of the force distribution on the rotor, which is of most interest for increasing energy capture and monitoring the structural integrity of the turbine. Because of these sensor errors, turbines often suffer from a lack of alignment with the oncoming wind flow; this is known as yaw error. This condition leads to a decrease in energy capture and large fatigue loads on the turbine (Burton, 2001). Improper yaw alignment has been shown to create a local rotor blade angle of attack near stall. The addition of tower shadow effects and the cyclic separation and reattachment of flow over the rotor blades create large aerodynamic loads beyond static stall values (Robinson, Hand, Simms, & Schreck, 1999). The source of yaw control errors can be contributed to several different factors such as hysteresis in drive components, improper yaw sensor mesh, development of backlash in yaw position sensors and long time constants between sensor responses and drive action. Wind turbines can experience yaw error routinely due to the dynamic nature of the wind as it continuously changes direction (Burton, 2001). If winds have high directional variance, yaw error is almost unavoidable especially on short time scales; however, a small increase in yaw response time could significantly improve energy capture by decreasing the turbine response time constant to variations in wind direction.

The development of an active yaw control algorithm has been explored in the literature using the maximum generated power as a means of determining the maximum wind speed direction based on a Hill Climbing Control (HCC) program (Farret, Pfitscher, & Bemardon, 2000). This method relies on continuous changes in yaw angle resulting in large time constants for correct perpendicular yaw alignment and an inability to align in non-steady state wind flow. Other methods utilize costly Doppler LIDAR (Light Detection and Ranging) systems, which apply lasers for three-dimensional mapping of the wind inflow to a turbine. These systems focus on the wind state and do not identify the loads experienced by the rotor blades.

In addition to yaw control errors, wind turbines can also suffer from pitch control errors. The use of active pitch control is common for power regulation. A pitch-controlled wind turbine uses the power output of the generator to determine the necessary pitch action. When power output increases beyond the rated capacity of the turbine's generator, a command is sent from the Supervisory Command and Data Acquisition (SCADA) system to the blade pitch mechanism to immediately turn (pitch) the rotor blades out of the wind. Conversely, as power output drops (i.e. wind speed decreases) the blades are turned back into the wind. This turning action along the longitudinal axis (pitch axis) is controlled by an electronic or hydraulic pitch motor and gear system. Generally, blades are pitched a few degrees every time the wind changes in order to maintain the optimum angle of attack to maximize the power output for all wind speeds. There are also active stall controlled and passive stall controlled wind turbines with different mechanisms for manipulating the blade pitch set point.

Pitch control is the predominant means of control in current utility-scale wind turbines and is highly sensitive to power output. Even a small change in pitch angle (on the order of 2 degrees of less) has a major impact on the performance and health of a wind turbine. The sensitivity to turbine performance is well illustrated by Burton 2001. The sources of pitch error are similar to those for yaw error and include hysteresis in pitch drive components, development of backlash in pitch position sensors and improper installation of the rotor blade in the field.

Power deficits, however, are not solely the result of incorrectly pitched blades. Yaw error, pitch error, rotor or drivetrain damage, and wind and weather conditions can all lead to reduced power levels. Figure 1-1 demonstrates this result in a 1 kW horizontal axis wind turbine; note that for normalized power output in the range of 70% and above, the reduction from 100% power can be due to either pitch error or yaw error. In order to distinguish between the two, it is proposed that the blade dynamic response be analyzed rather than relying on point measurements of wind speed, wind direction, and generator power for yaw and pitch control. In addition to being able to more precisely determine the wind loading conditions on the blades, structural dynamic analysis can be applied to monitor the health of the turbine components.

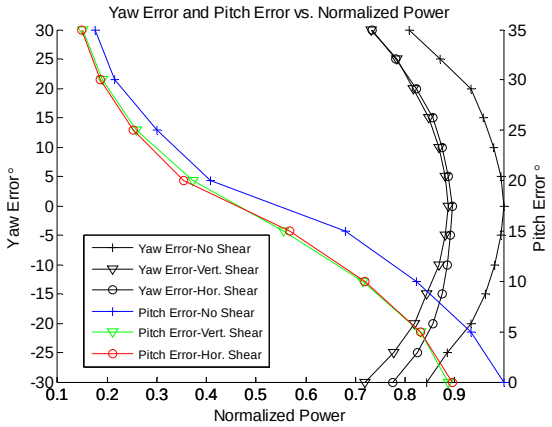

Figure 1-1: Experimental Wind Turbine Yaw and Pitch Error vs. Normalized Generator Power Output

Literature Review: Wind Turbine Damage Mechanisms and Failures

The premise of this chapter is that short-term (energy based) and long-term (reliability based) measures of performance of wind turbines are interrelated via the rotor response. It has been shown that an increase in turbine power output as wind turbines have grown in size is indeed correlated with a decrease in turbine reliability (Echavarria, Hahn, van Bussel, & Tomiyama, 2008). A doubling of the rated power of a turbine from 500 kW or less to more than 1000 kW has doubled the annual rate of reliability incidents. Additionally, the rated power of most utility-scale wind turbines places these machines into the reliability incident-prone category. This failure rate is partly the result of new designs for larger turbines due to the high demand for wind energy. Turbines at a rated power less than 500 kW have existed for 20 years or more and have experienced multiple design iterations to mature the technology.

Wind turbine blades account for approximately 7% of unforeseen malfunctions or failure, according to Hahn et al., 2007. While this percentage is not particularly high compared to other subsystems like the gearbox and bearings, turbine blades account for 15-20% of the total turbine cost. Blade damage is also the most expensive damage to repair and has the longest repair time (Flemming & Troels, 2003). Additionally, blade failure leads to secondary component damage in the entire system if prompt repair action is not taken, resulting in greater monetary losses (Ciang, Lee, & Bang, 2009). Blades can become damaged in various ways due to their complex geometry and materials. Turbine blades are generally fiber-reinforced composites with the majority of wind turbine blades being made of glass fiber/epoxy, glass fiber/polyester, wood/epoxy or carbon fiber/epoxy composites (Jureczko, Pawlak, & Mezyk, 2005).

Gearboxes account for approximately 4% of failures according to Hahn et al., 2007. It is believed that most gearbox failures do not begin as gear failures or gear-tooth design deficiencies. The observed failures appear to initiate at several specific bearing locations under certain applications, which may later advance into the gear teeth as bearing debris and excess clearances cause surface wear and misalignments (Musial, Butterfield, & Mcniff, 2007). More than 15% of these failures take place in the first five years (Mcniff, 2006). These failures occur in spite of the fact that most gearboxes have been designed and developed using the best bearing-design practices available (Musial, Butterfield, & Mcniff, 2007). It is speculated that the primary source of gearbox failure is due to the large bending moments applied at the low speed shaft from the rotor hub. These loads are produced by the complex rotor dynamics, which are a consequence of wind loading intensity and variability (White, Adams, Rumsey, & Zayas, 2009).

Another reliability concern for wind turbine rotor blades is blade ice accretion. As the number of wind turbines installed in cold weather climates or regions with cold and wet winters increases, blade ice accretion becomes a major reliability concern (Seifert, 2003). Winter often brings the most favorable wind conditions, but downtime due to blade icing or related damage due to blade icing must be avoided. Without effective ice detection and removal, wind turbines can suffer power reductions as high as 30% per year (Tammelin & Seifert, 2001). In addition to the economic loss, an example of related damage due to blade icing includes increased wind loading experienced by the rotor blade due to a decrease in aerodynamic performance and a rotor imbalance that can severely affect the drivetrain by means of undesirable torsional loads (Seifert, 2003).

An equally important concern of ice accretion is ice throw. As ice accumulates on the rotor blade in operation, shear and centrifugal forces act on the amassed ice, eventually leading to ice throw. It is most critical to detect ice accretion when the turbine is operating in an idle-speed condition. Here, the aerodynamic and centrifugal forces are small, as the rotational speed of the turbine is near zero. This permits the leading edge of the rotor blade to accumulate more ice at the stagnation point of the airfoil. When wind conditions become favorable for power production the rotational speed increases, the angle of attack changes and large masses of ice are shed (Tammelin & Seifert, 2001). According to Cattin et al., 2009, ice throw fragments up to 16 inches in length and weighing up to two pounds have been recorded over 300 feet from the nearest wind turbine. Ice throw of this magnitude pose a risk to civil structures and human life.

To improve the longevity of wind turbines, the sources of reliability shortcomings must be identified. It has been shown that variations in the rotor speed are one of the foremost causes of drivetrain failure (Hyers, McGowan, Sullivan, Manwell, & Syrett, 2006). One of the many sources of these cyclic torsional perturbations is the once per revolution (1 rot^{-1}) speed fluctuation encountered during aerodynamic asymmetry (Hameed, Hong, Cho, Ahn, & Song, 2009). These torsional oscillations affect not only the gearbox, but they adversely affect the health of blades, bearings, electric generators, and all other torsional components. One such source of aerodynamic asymmetries is yaw error, as discussed in the previous section, which occurs when the rotor blades encounter cyclic variations in the blade's angle of attack causing torsional vibrations at 1 rot^{-1} (Burton, 2001).

Literature Review: Damage Detection Methods in Rotor Blades

Damage detection methods have been applied to wind turbines in offline testing. For example, acoustic emission sensors have been used to detect the initiation and propagation of

cracks in blades, but the effectiveness of this method requires that the sensor location be relatively close to the damage location (Beattie, 1997). Fiber Bragg grating (FBG) strain gauges have been installed along the entire span of rotor blades to detect cracks. FBGs are immune to electromagnetic interference, and are lightweight; however, they lack the durability of other packaged sensor devices (Zayas, Roach, Rumsey, Allan, & Horsley, 2007). Digital image correlation (DIC) techniques have been used to determine real-time blade displacement and the global structural integrity by comparing operational video frames with a baseline image (Van Hemelrijck, Smits, & Philippidis, 2006). However, these systems are expensive and one system can only monitor a single turbine.

Capacitive accelerometers have also been implemented on utility scale wind turbines to measure the dynamic response of the blades (White, Adams, Rumsey, & Zayas, 2009). The ability to measure both static and dynamic acceleration was shown to provide a means for estimating the deflection of the blade as well as the variations in wind loads acting upon the blade. Modal impact testing of blades is commonly used to estimate the modal frequencies and modal deflection shapes in non-rotating blades (White J. R., 2010; Larsen, Hansen, Baumgart, & Carlen, 2002; Ghoshal, Dundaresan, Shulz, & Pai, 2000). Many other researchers have focused on using vibration response measurements from wind turbine rotor blades for the purpose of detecting and monitoring the growth of damage in the blades. For example, various algorithms for detecting damage in wind turbine blades were tested by measuring and processing data using piezoceramic sensor patches (Ghoshal, Dundaresan, Shulz, & Pai, 2000; Luczak, et al., 2010). However, the effects of operational loading on damage detection were not analyzed in these studies.

There are currently no standard solutions on the market for reliable ice detection that can be used as a control input for the turbine's supervisory system. Some measures to prevent icing have been successfully used and deicing methods are in development. However, not all methods operate continuously and there is a need for reliable ice detection to facilitate the activation of the deicing system (Homola, Nicklasson, & Sundsbo, 2006). Various sensors have been tested but have not performed satisfactorily. Homola et al. (2006) reviewed 29 methods of ice detection that included direct and indirect methods. The study concluded that only four methods were suitable for ice detection, but with limitations: 1) Infrared spectroscopy is limited to monitoring one section of the blade and requires the installation of fiber optic cables in the blade; 2) a flexible resonating diaphragm was shown to be effective but requires installation at multiple points inside the blade; 3) ultrasound has been proven effective at detecting ice on aircraft but has not been implemented in wind turbine blades and is not well suited for retro-fitting; 4) a change in capacitance was also measured using wires mounted in the surface of the blade.

Summary of Literature Review

Overall, predictive maintenance of rotor blades and other turbine subsystems can significantly reduce the cost of wind farm maintenance by as much as 50% when compared to the current reactive maintenances approach (Barber & Golbeck, 2010). This chapter examines the use of dynamic-based sensing within wind turbine rotor blades to facilitate both better maintenance and better control decision-making strategies. The ability to continuously monitor blades during operation has benefits both in terms of the wind farm power output (by identifying changes in the control set points to maximize energy capture) and blade health (by identifying damage that can be repaired early or blade damage that will necessitate blade replacement to

avoid the loss of other turbine subsystems). The detection of damage in operational blades is a form of condition monitoring. Operational modal analysis is one method for acquiring and processing data from the blade to estimate dynamic properties for use in damage detection and control. Figure 1-2 illustrates the dynamics-based approach that is described and applied in the remainder of this chapter.

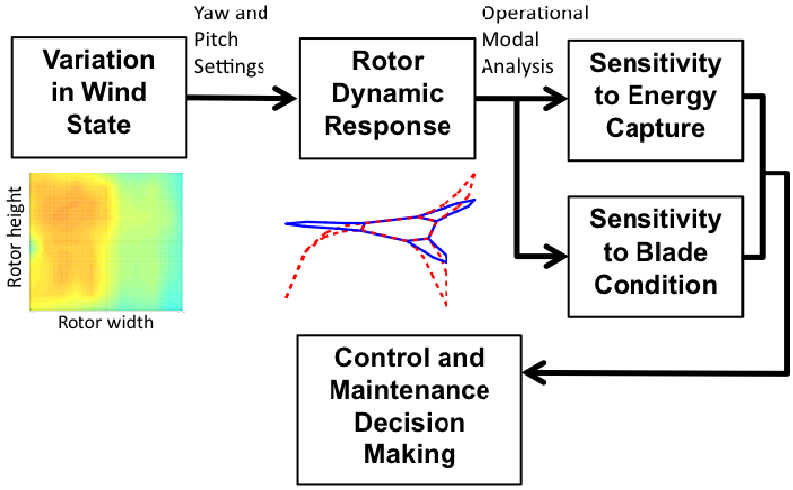

Figure 1-2: Illustration of technical focus of chapter on the identification and use of rotor structural response for control and maintenance decision-making.

2. EXPERIMENTAL HAWT TEST APPARATUS

Test Equipment

The operational data analyzed in this chapter was acquired using the small scale horizontal axis wind turbine test apparatus that is described in this section. The test apparatus is comprised of the test-bed enclosure and the instrumentation contained within the test-bed. Table 2-1 lists the major test equipment components and corresponding specifications.

The centerpiece of the test apparatus is a Whisper 100™ 2.1 meter rotor diameter wind turbine, which is manufactured by Southwest Windpower®. This small-scale wind energy converter is assumed to be analogous to a utility-scale wind turbine because both the small-scale and utility-scale turbines use the same physics to convert the kinetic energy of the wind into electricity. To observe the structural dynamics of the rotor, tri-axial Silicon Designs® 2460-050 DC biased accelerometers were mounted in several key locations. Each turbine blade had one of these transducers attached to the low pressure the blade using LOCTITE™ 454 industrial instant adhesive at a distance of 14 inches from the blade tip. A non-mechanical means of attaching the sensor, as opposed to a fastener that would have required the blade to be machined, was used to preserve the structural behavior and integrity of the relatively thin blade.

Another DC tri-axial accelerometer (PCB® 3713B1150G) was mounted on the nacelle of the wind turbine. This accelerometer was used to observe the forced response of the turbine outside the rotor blades in a non-rotating reference frame. A cup anemometer was used to collect operational wind speeds during testing. The wind speed transducer was mounted on the nacelle of the turbine behind the rotor. This placement was not ideal for measuring wind speed, but did allow for repeatable measurements and does not interrupt the inflow to the rotor disk. To accurately measure the rotational speed of the wind turbine, an optical tachometer was mounted

to the side of the nacelle. Reflective tape was applied to each blade at the rotor hub for use with the tachometer. In addition to the sensors mentioned above, the voltage output of the turbine was also collected from the Whisper Power Controller. This controller rectifies 3-phase AC power from the turbine generator to a DC voltage output.

Table 2-1: Major test components and specifications of the wind turbine test-bed.

Component	**Quantity**	**Specifications**
Whisper 100 Wind Turbine	1	SWWP, 2.1 m rotor dia., 900W at 12.5 m/s
Whisper Power Controller	1	12V power output, over speed regulation
DC Tri-axial Accelerometer (Blade mounted)	3	SDInc, Model 2460, 80mV/g, +-50g pk, 0 to 2k Hz frequency range, 8-32V DC operation
DC Tri-axial Accelerometer (Nacelle mounted)	1	PCB®, Model 3713B1150G, 40mV/g, +- 50g pk, 0 to 1k Hz frequency range, 6-30V DC
Cup Anemometer	1	Omega®, WMS-21 Wind Speed Transducer
Optical Tachometer	1	Banner Engineering Corp., Mini-Beam® SM312LVQDP, Retro-reflective
Slip Ring	1	Electro-Miniatures Corp., Model 2175, 24 circuit, 1-Amp/Circuit, Variable Speed
cDAQ-9172 Chassis	1	National Instruments™, holds eight I/O modules, USB 2.0-compliant, two 32-bit counter/timer chips
NI® 9234 Input Module	4	4 channel, 24-bit resolution; 102 dB dynamic range; Software-selectable AC/DC coupling; Software-selectable IEPE signal conditioning
NI® 9215 Input Module	1	4 channel,+-10V 16-bit simultaneous analog input, 60VDC CAT I Ch-to-Earth Isolation
DC Power Supply	2	TENMA® 72-6628 Variable Output DC Power Supply

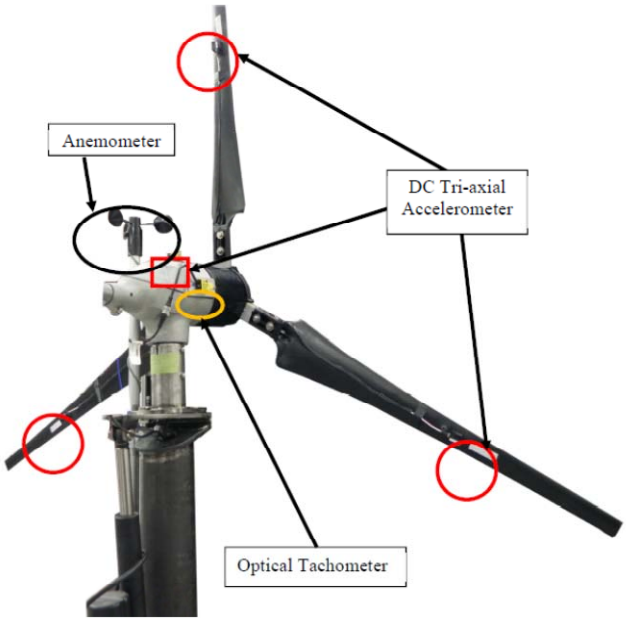

Figure 2-1: Whisper100 HAWT test apparatus with major components labeled.

To transmit the DC accelerometer signals from the rotor blades, a slip ring was customized to fit inside a hollow portion of the turbine nacelle, which housed the rotor shaft. Figure 2-2

illustrates the rotor shaft and bearing assembly that were attached to the slip ring via a flexible coupling. The slip ring was rigidly fastened to an aluminum collar inside the nacelle. The coupling union was made of neoprene, which offered shock and vibration damping from the heavy rotor shaft to help extend the life of the slip ring. The slip ring enabled 12 channels to be powered and transmitted from the rotating to the non-rotating reference frame: 9 channels were used for the DC tri-axial accelerometers (3 channels for accelerometer per blade) and 1 channel was used for common DC voltage to power the DC tri-axial accelerometers.

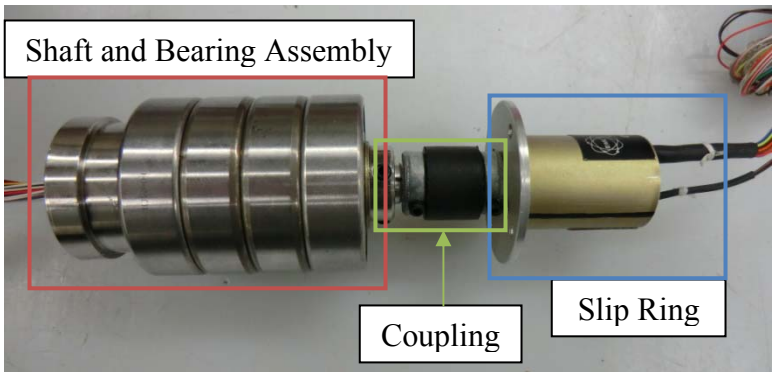

Figure 2-2: Slip ring attached to rotor shaft and bearing assembly by a flexible coupling.

Pitch and Yaw Control Features

The test apparatus was used to set the yaw and pitch to any desired angle. The yaw set point was adjusted by loosening a pair of gear clamps on the turbine tower and then pivoting the nacelle about the yaw axis to the desired degree marker on the yaw joint. The mechanism for setting these angles is pictured in Figure 2-3. Once the desired yaw angle was reached, the gear clamps were tightened to hold the yaw position. Yawed flow was tested in this manner. When the yaw degree mark was set to zero, the wind turbine rotor disk was perpendicular to the incoming wind flow resulting in no yaw error. When the turbine's yaw position was adjusted to any degree mark greater than or less than 0°, the turbine experienced the effects of yaw error.

Error! Reference source not found.. Yaw set point control fixture. (a) downwind and (b) upwind side of tower.

Similarly, the pitch angle of each rotor blade was adjusted by loosening the mounting bolts at the plate interface of the pitch fixture located near the rotor hub and then turning the blade about the pitch axis to the desired angle. Figure 2-4 shows the installed pitch fixture and a detailed view of the bolted plate interface with degree marks. The pitch fixture was an aluminum bolt-on attachment that was designed to fit the wind turbine. Positive pitch angles were achieved when the leading edge of the blade was turned toward the wind inflow thereby increasing the angle of attack and decreasing the aerodynamic efficiency of the blade. A zero degree pitch angle indicates no pitch error.

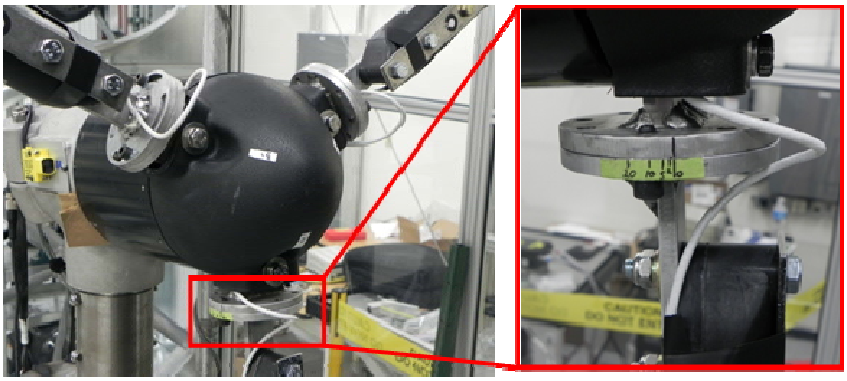

Figure 2-3: Rotor blade pitch control fixture (a) rotor blade hub and fixture; (b) detail view of plate interface and degree marks of variable pitch fixture.

Test-Bed Enclosure

The test-bed enclosure is pictured in Figure 2-4 from the front-side. The Whisper 100 turbine is located inside the enclosure. The test-bed was built on a framework of I-beams (pictured in Figure 2-4). The overall footprint of the test-bed was approximately 15x9.5ft. The rectangular steel I-beam frame was mounted on four heavy-duty spring hinge casters at each corner to allow the test-bed to be mobile. A floor jack was mounted next to each caster to support the test-bed weight during operational testing. To make the turbine accessible to the user, a plywood floor was installed.

A 9x9ft polycarbonate honeycomb core by Hexcel® with ¼ inch cell size (left side of Figure 2-4) was installed at the inlet of the test chamber. The stabilizer core served two functions: (1) develop directional flow down the test chamber and (2) create a quasi-laminar flow state. This core created a nearly uniform airflow over the entire rotor disk that was free of transients due to gusting or lateral velocity components. Airflow was generated at the opposite end of the test frame using four 7.5 hp belt-driven, axial fans (with 48 in blade diameter) that were each capable of moving 30,000 cubic feet of air per minute. The capacity of the fans was sufficient to generate wind speeds within the operating standards of the wind turbine (4-15 mph). To maintain safety, the exit of each fan was guarded with a heavy gauge sheet metal shroud that was covered with wire mesh to allow for uninterrupted exit flow. The airflow rate was controlled by adjusting the rotational speed of the four fans using a Schneider Electric® Square D® E-Flex™ adjustable speed drive controller that was connected to three phase 440V. The motor controller allowed for precise control of the fan speed by 0.1 Hz increments from 0Hz to 60Hz (3600 rpm). To contain generated airflow and to maintain safe operation, an enclosure was fabricated from 2 inch 80/20® Inc. and ¼ inch clear polycarbonate panels.

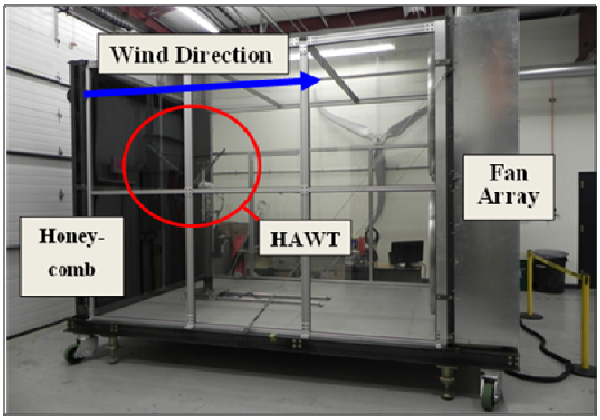

Figure 2-4: Final design of the 2.1 m rotor diameter HAWT dynamics and control test-bed.

Data Acquisition Hardware and Methodology

Operational data was acquired using a National Instruments™ cDAQ-9172 chassis with multiple input modules inserted in the chassis. Three of the four NI 9234 input modules were used to acquire the 12 channels of acceleration data. The fourth NI 9234 input module was used to collect the signal from the optical tachometer. The NI 9215 input module was used to acquire the cup anemometer signal from the digital readout and the voltage output signal of the wind turbine from the power controller. Figure 2-5 shows the DAQ with input modules, DC power supplies, and anemometer digital readout.

The benefit of DC coupled accelerometers, and the reason they were chosen over AC coupled accelerometers, is demonstrated in the differences between the blade responses that are plotted in Figure 2-6. The DC coupled sensor provided accurate readings of both the quasi-static (<5 Hz) and dynamic acceleration components of the blade at the sensor attachment location (White J. R., 2010).

Figure 2-5: DAQ hardware, DC power supplies (2), and cup anemometer digital readout.

Sample Data Set

A sample forced response time history of approximately eight turbine revolutions is plotted in Figure 2-6. The tachometer/keyphasor signal was processed to remove all noise to produce a square wave that oscillates with a magnitude between 0 and 1. In Figure 2-6, the accelerometer

data is plotted in units of g's (1 g = 9.81 m/s^2). The largest DC offset (signal mean) is observed in the span (x) direction due to the centripetal acceleration along the radial axis. Three contiguous one revolution samples are representative of the data segment lengths that were used in the synchronous averaging procedure.

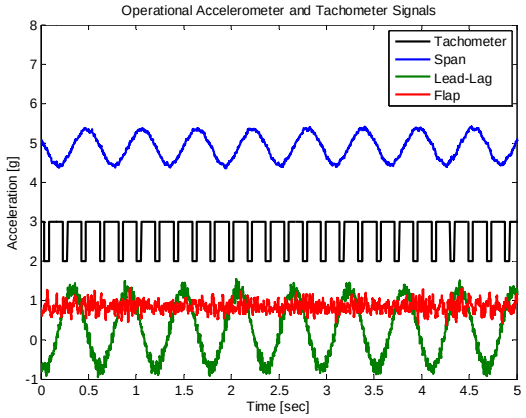

Figure 2-6: Sample time history from tri-axial accelerometer and processed tach signal

Wind Shear Characterization

To characterize how the rotor forced response of the turbine changed due to yaw and pitch set-point errors and how these changes affected the sensitivity of blade measurements to damage mechanisms, it was important to quantify the forcing function acting on the rotor disk. To do this, wind speed measurements were taken at the inlet of the test-bed enclosure to quantify the wind profile for horizontal and vertical wind shear as well as a uniform wind condition. A 10 by 10 matrix of wind speeds totaling 100 discrete wind speed data points were sampled using the cup anemometer placed 6 inches from the honeycomb. The data was linearly interpolated between the sampled points and a color bar was added to better highlight the variation in wind speed. The resulting profile for a non-shear wind condition is plotted in Figure 2-7. The transparent disk when overlaid on the velocity contour map represents the area of the rotor disk during operation and the arrow indicates the direction of rotation.

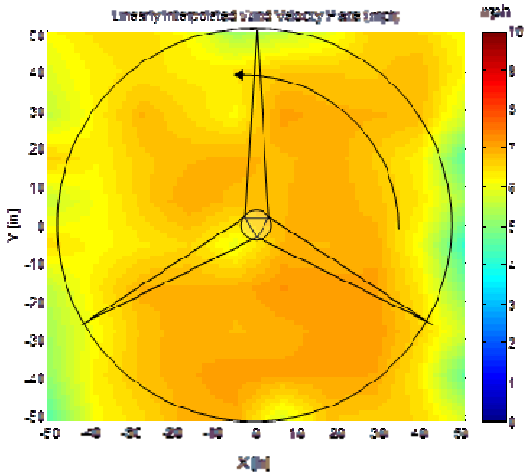

Figure 2-8: Measured wind profile for the uniform wind condition at 35 Hz fan speed.

To create a vertical and horizontal wind shear condition, screening material was used to shape the wind inflow at the inlet of the test chamber. For the horizontal (side) shear condition, the screening material was used to restrict airflow on the right side enclosure inlet and create a horizontal gradient in wind speed. For the vertical wind shear condition, the screening material was used to restrict airflow on the lower half of the enclosure inlet and create a vertical gradient in wind speed. The resulting wind speed contours for the negative side shear condition and vertical shear condition are plotted in Figure 2-0.

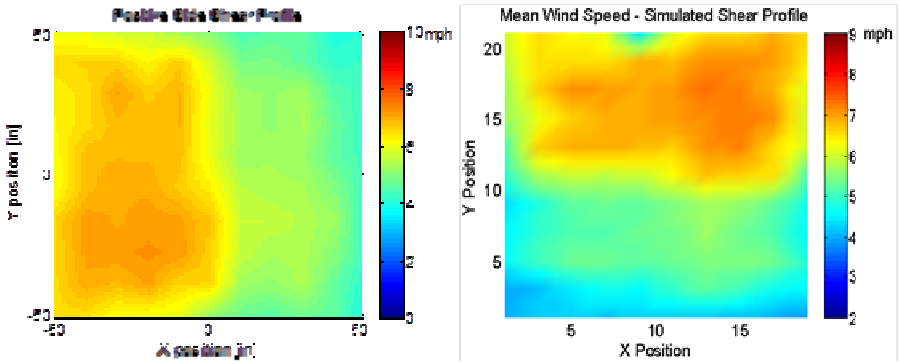

Figure 2-9: Measured wind profile for the side (horizontal) shear condition and the vertical shear condition at 35 Hz fan speed.

Operational Testing Procedures

A total of 189 tests were conducted, as outlined in Table 2-2. In each test, the fan speed was held constant at 35Hz or 2100 rpm to generate wind speeds of approximately 7 mph. The test duration was ten minutes and began when the rotor had reached its steady state rotational speed. The test data was later segmented into an ensemble of ten, one-minute duration consecutive data sets to allow for the application of statistical analysis. Damage conditions 1, 2, and 3 in Table 2-2 correspond to no damage, blade ice accretion, and a blade root crack, respectively. The damage conditions were tested through a range of yaw error angles, pitch error angles, and wind states to determine how the blade dynamic response changes due to both variations in the wind state and damage to the rotor. Note that for pitch error testing, only a single blade was pitched away from 0°, representing the case in which (a) a blade was bolted on in the incorrect position during installation, or (b) a single blade has developed hysteresis in its pitch drive components or backlash in its pitch position sensors. This blade was the same blade that was damaged during those tests. The pristine, or undamaged, turbine test data served not only as a baseline reference when applying damage detection algorithms, but was also used to estimate yaw and pitch errors based on the analysis of the blade acceleration measurements.

Table 2-2: Outline Of Tests Conducted.

Test Parameter	Wind State	Error Angles	Damage Condition
Yaw Error	Uniform	-30° to 30° in 5° increments	1, 2, 3
Yaw Error	Vertical Shear	-30° to 30° in 5° increments	1, 2, 3
Yaw Error	Horizontal Shear	-30° to 30° in 5° increments	1, 2, 3
Pitch Error	Uniform	0° to 35° in 5° increments	1, 2, 3
Pitch Error	Vertical Shear	0° to 35° in 5° increments	1, 2, 3
Pitch Error	Horizontal Shear	0° to 35° in 5° increments	1, 2, 3

To simulate ice accretion, thin gauge sheet metal was cut to match the shape of blade profile and then fixed to the leading edge and high-pressure side of each blade with masking tape. This added material was meant to disrupt the aerodynamic performance of the airfoil as well as to add distributed mass to the blades. The added mass was designed to be 1/20th of the blade mass, which was an amount determined using the dimensions of a Vestas AL40 wind turbine blade and the density of ice to mimic a realistic icing event. However, icing events arise from many complex meteorological events that result in a wide variety of ice formations. The simulated ice accretion in this case does not emulate the surface roughness of ice nor the changes in ice accumulation during operation. A blade root crack was simulated by inserting rubber grommets between the joining plates of the pitch adjustment fixture, thereby decreasing the stiffness in the joint, especially in the flap direction. Figure 2-10 shows the grommets and the resulting gap between the pitch adjustment plates; this gap was measured each time the pitch was varied during testing to ensure that the stiffness was constant for each pitch angle.

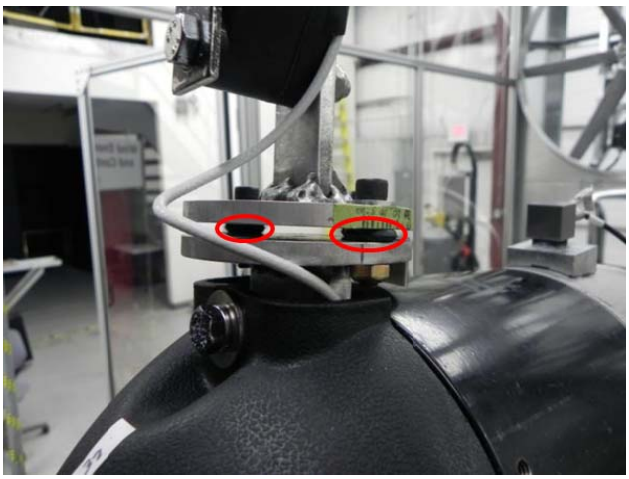

Figure 2-10: Rubber Grommets for Simulated Root Crack.

MODAL ANALYSIS OF THE WIND TURBINE ROTOR BLADES

Wind turbine rotor blade modes of vibration are excited by wind loads to a greater or lesser degree depending on both the frequency of wind loading and the spatial distribution of that loading. The first step taken to identify changes in the operating state of the wind turbine rotor was to characterize the free dynamic response of the three-bladed rotor system. Knowledge of the free response of the rotor is critical when attempting to monitor the health of the blades because the operational response is a convolution of the blade free response characteristics and the blade forcing function. The mode shapes and resonant frequencies of the rotor dictate the modes of vibration that will be most sensitive to changes in the turbine's operating state (i.e. changes in wind state and/or changes in yaw and pitch set point) and blade damage condition.

Experimental Approach for Modal Testing

To identify the free response characteristics of the wind turbine rotor system, a modal impact test was performed. A multi-reference modal impact test was conducted using three measurement degrees of freedom (DOF) that were local to each rotor blade's coordinate system. The measurement degrees of freedom are denoted as follows: X: span, Y: lead-lag and Z: flap (flap is measured perpendicular to the blade surface). Figure 2-11 illustrates the local degrees of

freedom of a rotor blade. In total, there were nine reference channels of data, which were acquired using an Agilent E8401A VXI mainframe that was paired with an E1432A module, which sampled at 51.2 kHz. A PCB Piezotronics modally tuned hammer (model 086C01, nominal sensitivity 50 mV/lbf) was used to apply and measure the impulsive forces in the direction pendicular to the blade at each point indicated. The modal test grid consisted of 27 impact points that followed the geometry of the blade. This impact grid offered sufficient spatial resolution to clearly identify and distinguish mode shapes. A threshold force window was applied to the force time history to minimize the noise on the force data outside the applied force pulse. After applying five modal impacts at each location and measuring both the impact force and response time histories corresponding to these impacts, the single–input, multiple-output frequency response functions were estimated for the five averages using the H1 algorithm to minimize the effects of noise on the response measurements (Adams D. E., 2007). Ordinary coherence functions were also estimated to determine the quality of fit of the frequency response function models.

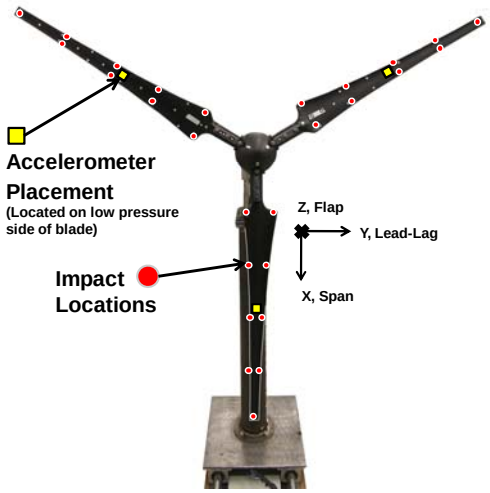

Figure 2-11: Details of accelerometer placement, input and output measurement degrees of freedom and local blade degrees of freedom on the Whisper 100 wind turbine.

Experimental Results from Modal Impact Testing

The multiple-input, multiple-output frequency response function data were analyzed using the Complex Mode Indicator Function, or CMIF (Shih, Tsuei, Allemang, & Brown, 1989). The CMIF is mathematically well suited to identify closely spaced modal frequencies by using the singular value decomposition of the normal matrix that was produced using the matrix of frequency response function data. The results of this computation are illustrated in Figure 2-12. The top three spectral lines of this plot were used to identify degenerate modes of vibration with repeated roots and pseudo-repeated roots. At frequencies shared by these three spectral lines, multiple roots are said to exist. One of the more dominant modes was identified at 8.59 Hz for which there were three roots corresponding to this single mode of vibration; consequently, there were three modal deflection shapes associated with this mode of vibration.

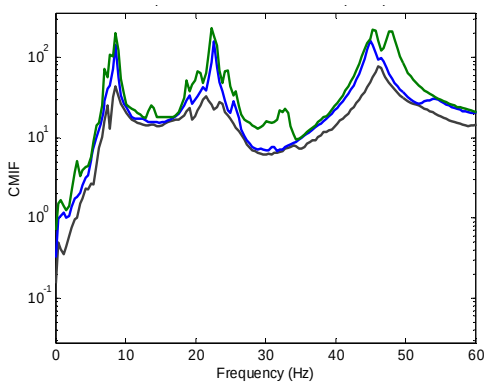

Figure 2-12: CMIF plot used to identify natural frequencies of turbine rotor and hub assembly

Table 2-3 provides a summary of the damped natural frequencies represented by each peak and multiple peaks found in the CMIF plot. The mode shape descriptions were developed by observing the animated mode shapes. The mode at 8.59 Hz is a pure first bending mode with a large magnitude of response as seen in Figure 2-12.

Table 2-3: Summary of turbine modes of vibration identified using CMIF.

ω_d (Hz)	Mode Shape Description
3.13	1st bending – Asymmetric bending + slight blade torsion w/ hub rocking
7.03 (2 roots)	1st bending – Asymmetric bending w/ one blade in 1st bending and other blades bending w/ hub rocking
7.81 (2 roots)	1st bending – All roots w/ asymmetric blade motion w/ different phase on each root, slight rocking of hub
8.59 (3 roots)	1st bending – Asymmetric bending, no rocking of hub. Two blades bend in phase and the third blade is out of phase
13.67	1st bending – Asymmetric bending + slight blade torsion w/hub motion in and out of rotor plane in phase with bend
18.75 (3 roots)	1st bending – Asymmetric bending w/ hub rocking. Two blades bend in phase and the third blade is out of phase
20.31	1st bending – Pseudo repeated root of 18.75Hz
22.27 (2 roots)	1st bending – Asymmetric bending w/hub motion in and out of rotor plane
24.61	1st bending – Asymmetric bending w/blade torsion

Modal Deflection Shapes of Wind Turbine Rotor Blades

To better categorize the free response behavior, the mode shapes were animated and the behavior of each mode shape was observed. The descriptions provided in Table 2-3 were based on the animation. Figure 2-13 shows the three modal deflection shapes associated with the damped natural frequency near 8.6 Hz (3 roots). These deflection shapes illustrate the phase difference between blades in the modal deflections for the case of a repeated root. Figure 2-13 (a) and (b) exhibit first bending with two blades bending in phase and the third blade bending out of phase. It is believed this mode of vibration and its associated deflection patterns are related to the asymmetric loading that is experienced during operation such as during horizontal or vertical

wind shear inflow conditions. Figure 2-13 (c) exhibits symmetric bending in which all three blades move in phase. This mode shape is often called an umbrella mode.

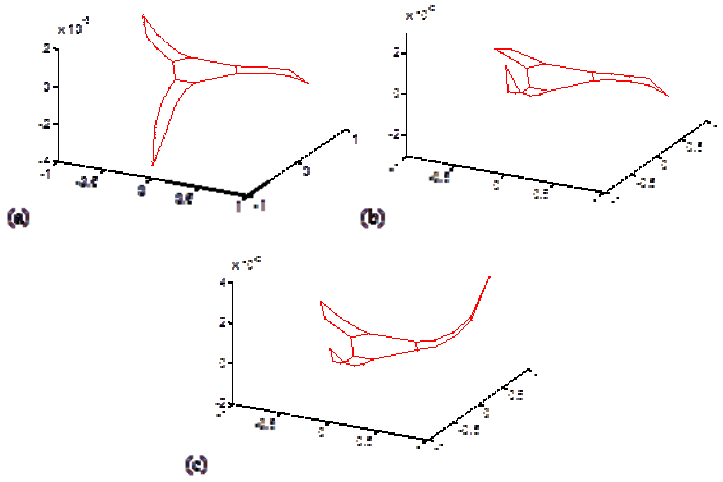

Figure 2-13: Deflection shapes for modes of vibration near 8.6 Hz showing phase difference between repeated roots. Axes: x, y and deflection amplitude. (a) Asymmetric bending. (b) Asymmetric bending of second root. (c) Symmetric bending of third root.

DATA ANALYSIS APPROACHES

Cyclic averaging

Accelerometer measurement data will contain some level of random noise. To improve the accuracy with which the time and frequency data can be analyzed, time-synchronous averaging is applied. Blocks of time-sampled data are synchronized using the optical tachometer pulses so that they each begin at the same angular position of the rotor to eliminate the randomness associated with the differences in phase of the blocks of data that are averaged. Components of the signal that are synchronized with the trigger, which is the optical tachometer pulse in this case, are retained, while random noise is averaged out. A block size of three rotations of the rotor is used throughout this analysis so that the averaged time history is long enough to achieve sufficient frequency resolution, which is equal to the inverse of the time history length.

Operational Modal Analysis (OMA)

The velocity field on the wind plane at the inlet to the rotor disk is experimentally measured for each wind shear condition, but the force distribution along the blades is unknown. In order to generate frequency response functions (FRFs) from the accelerometer data that is acquired from the rotor blades, operational modal analysis (OMA) is applied. The two primary assumptions in OMA are: (1) the power spectrum of the input force is broadband and smooth, i.e. has no poles or zeroes in the frequency range of interest, and (2) the forcing function is spatially distributed in a uniform manner (Chauhan, Martell, Allemang, & Brown, 2007). Assumption (1) is not particularly applicable to wind-excited structures because the power spectrum of wind is generally dominated by low-frequency components (Burton, 2001). In general, rotating machinery is self-excited at harmonics of the operating speed (Rau, 1995), and these harmonics are clearly evident in the OMA frequency response functions that are measured from the turbine being tested in this chapter. Assumption (2) is reasonable for a rotating wind turbine, and the

measured wind planes in Figure 2-8 and Figure 2-9 demonstrate the spatial uniformity of the wind speed across the rotor disk inlet

The OMA procedure consists of first computing the autocorrelation of the synchronously averaged time response for each channel of data. The result is two-sided, containing a positive exponential portion corresponding to the negative poles of the power spectrum, and a decaying exponential portion corresponding to the positive poles (Chauhan, et. al, 2007). Since both parts of the autocorrelation contain the same information, the positive exponential part is set to zero, essentially zero-padding the time signal. The resulting function is treated as an impulse response function, the discrete Fourier transform of which is the OMA frequency response function. In dynamic systems, the impulse response and frequency response functions are related through the Fourier transform in this manner. Figure 2-14 schematically describes the OMA process.

Figure 2-14: OMA Data Processing Flowchart (Yutzy, 2011).

The discrete Fourier transform is carried out in the order domain, which measures frequency relative to the rotational position rather than absolute time (rotations^{-1} rather than seconds^{-1}). This order domain approach is convenient for analyzing the dynamics of rotating machinery for two reasons: 1) as stated previously, these systems are typically self-excited at harmonics of the rotational frequency, and 2) variation of the independent parameters throughout testing, such as yaw and pitch error, affects the rotational speed of the rotor; therefore, analysis in the order domain allows for comparisons to be made between these unequal-speed data sets.

Feature Extraction

In each experiment conducted, a feature with variable name x is extracted from the processed data to indicate a change in the parameter being studied. In practice, such features are calculated from raw data and then used by the operator to implement control or maintenance decisions.

Yaw Error

Due to fluctuations in aerodynamic loading, yaw error is most prevalent in accelerometer data at a once-per-revolution frequency: 1 rot^{-1} in the order domain (Yutzy, 2011). The result of integrating the OMA FRF from 0.5 to 1.5 rot^{-1} has been shown to be an indicator of yaw error, even in the presence of horizontal and vertical wind shear (Yutzy, 2011). The yaw error data throughout this chapter is analyzed using the following procedure:

1.) The OMA FRF is calculated for each measurement channel including the flap, lead-lag, and span directions on each blade.
2.) The OMA FRFs of blade degree of freedom groups (i.e., the flap, lead-lag, and span groups) are averaged, resulting in one OMA FRF for each direction associated with the three blade degrees of freedom.
3.) Each of the averaged OMA FRFs are integrated from 0.5 to 1.5 rot^{-1}.
4.) The integration results, one for each degree of freedom, are the feature values, x.

Pitch Error

Recall that only a single blade underwent pitch error during testing. The blade flap responses couple with the fore-aft acceleration response of the nacelle, and that coupling varies

depending on the pitch angle of each blade. In order to calculate the feature value for pitch error, the following procedure is used:

1.) The cross-power spectrum is calculated between each blade's de-meaned, time-synchronously averaged flap acceleration response and the fore-aft acceleration response measured on the nacelle housing. The discrete Fourier transform is performed in the order domain.
2.) The peak in each cross-power spectrum magnitude closest to 1 rot^{-1} is found.
3.) The pitched blade has a higher magnitude of response in the cross power spectrum at 1 rot^{-1} than the other two blades. The feature is the sum of the difference of the peak value in the pitched blade's cross power spectrum at 1 rot^{-1} with the other two blades' peak values, normalized by the sum of the non-pitched blade's peak response. This normalization accounts for relative magnitude differences due to reduced rotor speed in the high pitch-angle tests. Mathematically, the feature value, x, is:

$$x = \frac{[(p_3 - p_1) + (p_3 - p_2)]}{p_1 + p_2} \quad \text{Eq 1}$$

where p_3 = peak in pitched blade's cross power spectrum magnitude at 1 rot^{-1}
p_1 = peak in non-pitched blade one's cross power spectrum magnitude at 1 rot^{-1}
p_2 = peak in non-pitched blade two's cross power spectrum magnitude at 1 rot^{-1}

Blade Damage Detection

For damage detection, the time-synchronously averaged operational response data is analyzed in the frequency domain. The averaged linear spectra are calculated using the discrete Fourier transform. Figure 4-2 (a) shows an example of the linear spectra magnitude for the case of blade ice accretion and undamaged blades. Many of the peaks in the linear spectra occur at frequencies that correspond to the modes of vibration. The information gleaned in the modal analysis of the rotor blades helps develop an understanding of which modes are excited during operation. Mode shape analysis is used to identify frequencies in the operational data that correspond to asymmetric bending modes such as modes at 3.1 Hz and 8.6 Hz, but any frequency with a known mode of interest can be evaluated. Trends in the dynamic response at these frequencies can be exploited to reveal a change in the rotor blade condition and how the ability to observe that condition varies with yaw angle.

To evaluate these trends, the mode (frequency) of interest selected in the processed operating frequency spectra and the maximum value of the magnitude of the DC acceleration is recorded for a single degree of freedom for each blade within the frequency band. This procedure is carried out for each minute of the 10 min data set and the 10 values are averaged to provide one value for each blade at each yaw angle. The figures below illustrate the frequency banding process, where the frequency of interest is 3.1 Hz. The linear spectra are then bound from 2 to 4 Hz and the maximum acceleration value is found for each blade on this interval.

The magnitude of the acceleration for each blade is used to compare the change in response due to a damage condition and a yaw angle in various wind regimes. In the case of blade root damage, the responses of the blades are compared by finding the difference in response between blade pairs. In this study, Blade 3 is made to experience a reduction in stiffness at the root boundary condition. The reduction in stiffness should cause a change in operational response of this blade and is measured against the healthy blades; Blades 1 and 2.

For this damage case, the difference in response between Blades 1 and 3 should, therefore, be greater than the difference between Blades 1 and 2.

For the case of ice accretion, the magnitude of acceleration is again used to track changes in operating response of each blade at a particular frequency of interest. Here, the magnitude of the response when ice is present on the rotor blades is compared to the magnitude of the response for un-iced blades by calculating the percent error between the historical baseline response and the iced blade response.

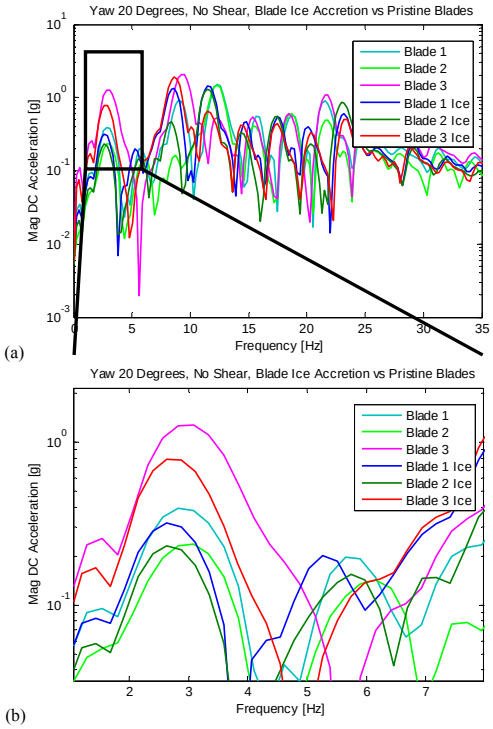

Figure 2-15: Example of frequency bounding process. (a) Linear spectra of blade ice accretion and pristine blades for Flap DOF at 20° yaw angle. (b) Detailed view at frequency of interest.

Statistical Modeling

Ten one-minute duration tests are conducted for each test scenario, allowing for the calculation of ten feature values for each test condition. Each test condition is defined in terms of the corresponding yaw or pitch error, blade damage/condition, and wind shear profile. Statistical analysis is applied using hypothesis testing to determine how variations in the wind load affect the sensitivity to yaw or pitch error and the sensitivity to rotor damage/condition. The feature, x, is normalized to obtain its standard score according to

$$\frac{x - \mu}{\sigma} \qquad \text{Eq 2}$$

where μ and σ are the estimated mean and standard deviation of x, respectively. The standard score is how many standard deviations x is above or below its mean. Because Equation 3 is normalized by σ, changes in x are more readily detected when the feature has little variance for a given operating condition. If x is assumed to be equal to $\mu \pm 3\sigma$, then the level of change in x from the mean value corresponds to a 99% confidence interval, i.e. the analyst is 99% certain that the feature has undergone a biased change even in the presence of natural variations in x

(Adams, White, Rumsey, & Farrar, 2011). When this value of *x* is substituted into Equation 1 and then normalized, the following result is obtained,

$$\left|\frac{x}{\mu} - 1\right| = \frac{3\sigma}{\mu} \qquad \text{Eq 3}$$

expressing how much of a shift in *x* is required to detect a statistically significant change in the feature mean with 99% confidence. For example, if *x* in the flap direction for yaw error exhibits a σ/μ of 0.02, then a 6% change in *x* (3*0.02) is required to achieve 99% confidence that a change due to yaw error has occurred. Therefore, the result of Equation 2 represents a measurement of the sensitivity of *x*: if it is small, then the sensitivity is high, and that is desirable in terms of condition monitoring because it means that, even amidst variations in wind loading and other factors, a small change in *x* indicates a significant change in the feature.

EXPERIMENTAL RESULTS AND DISCUSSION

Yaw Error Detection

The yaw error feature is calculated in each of the blade degrees of freedom for the three different wind conditions. These feature values are first plotted versus the yaw error angle to produce one curve for each wind condition and rotor blade measurement degree of freedom in Figure 2-16, Figure 2-18, and Figure 2-20. Each of these figures has an accompanying sensitivity curve, which is a plot of the percent change in the feature that is required to detect yaw error with 99% confidence, which is equivalent to $3\sigma_x/\mu_x$. A low value on these curves indicates a high sensitivity of the feature at that particular yaw error and wind plane shear condition. For instance, in Figure 2-17, the value on the vertical shear sensitivity curve at +10° yaw error is 5%, while the value on the no-shear sensitivity curve is 15%. Thus, it can be said that under a vertically sheared wind profile, only a 5% change in the feature, *x*, from its mean value is required to detect a yaw error of +10°, but under a uniform wind velocity distribution, a 15% change in the mean value of the feature is required to detect the same +10° yaw error.

Yaw Error Feature: Flap DOF

Several important findings in the presence of yaw error can be extracted from the plots of the flap measurement degree of freedom response and sensitivity seen in Figure 2-16 and Figure 2-17.

-First, as expected, the power extracted from the wind in the test cases involving wind shear is lower than the corresponding case involving no wind shear (Figure 2-16). Generator power is also reduced due to yaw error.

- Second, Figure 2-16 shows that the feature is symmetric about 0° yaw error for the uniform (no-shear) wind condition, whereas the vertical and horizontal wind shears produce asymmetric curves. Asymmetry can be helpful from a controls standpoint because each yaw error can then be associated with a unique feature value. For instance, if the wind turbine is in a uniform flow and the normalized flap response feature value is 0.5, the yaw error could be either +5° or -10°. If, however, the wind profile is characterized by vertical shear, that same normalized feature value of 0.5 would indicate approximately a +8° yaw error.

- Third, it is observed that wind shear does not hinder but rather enhances the ability to detect yaw error. This increase in sensitivity in the presence of wind shear is clearly evident in

Figure 2-17 because the wind shear curves are much smaller in magnitude and, therefore, much larger in sensitivity as explained previously. The reason why wind shear does not interfere with the feature calculation is that it tends to affect the 3 rot^{-1} blade dynamics (Yutzy, 2011); therefore, it does not affect the integration of the OMA FRF over the 0.5 to 1.5 rot^{-1} range.

- Fourth, under horizontal wind shear the sensitivity decreases (the % change in x required to detect a change in the feature value with 99% confidence increases) as the turbine is yawed into the side of the inlet plane with higher velocity wind (positive yaw error). Horizontal wind shear can be particularly prevalent in wind farms due to the presence of wake flows from upstream turbine rotors, which produce velocity deficits on downstream turbine rotors.

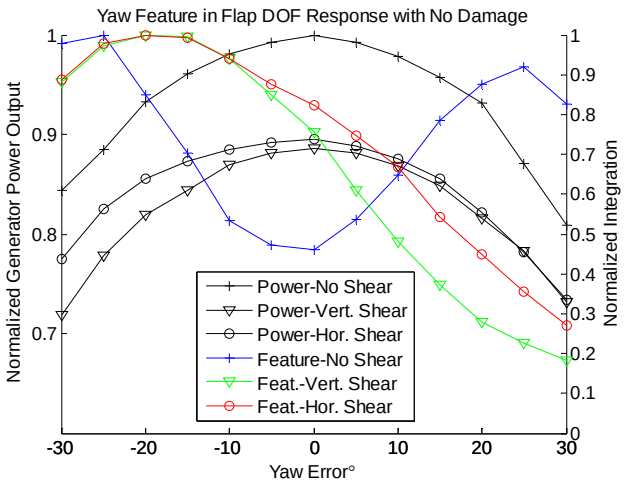

Figure 2-16: Normalized Yaw Feature and Power vs. Yaw Error Angle for Flap DOF

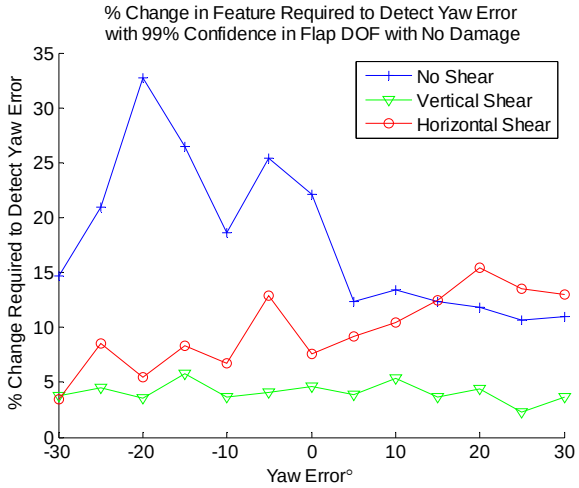

Figure 2-17: Sensitivity of Yaw Feature vs. Yaw Error Angle for Flap DOF

Yaw Error Feature: Lead-Lag DOF

Figure 2-18 shows that in the lead-lag DOF, the feature is nearly symmetric about 0° yaw error, regardless of wind shear condition. Furthermore, Figure 2-19 indicates that the feature sensitivity is two orders of magnitude higher in the lead-lag direction than in the flap direction of Figure 2-17, likely because the blade undergoes only relatively small deflection in the stiffer lead-lag direction, and thus experiences less variation due to factors other than yaw error. So not only is the standard deviation of the lead-lag measurements lower, but a higher proportion of the variation in this direction is due to yaw error compared to the flap direction.

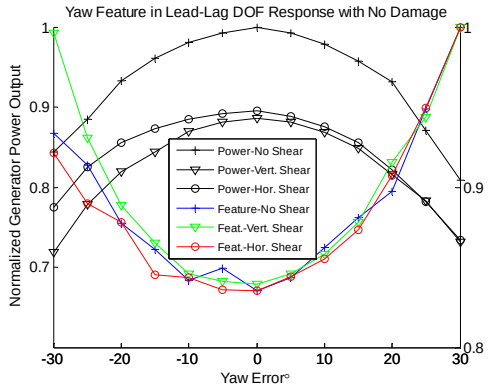

Figure 2-18: Normalized Yaw Feature and Power vs. Yaw Error Angle for Lead-Lag DOF

Figure 2-19: Sensitivity of Yaw Feature vs. Yaw Error Angle for Lead-Lag DOF

Yaw Error Feature: Span DOF

The span DOF exhibits similar feature curves as the lead-lag DOF in the vertical and horizontal shear conditions, but the uniform flow condition produces a nearly-flat feature curve between ±20°, which is not desirable because it means that a wide range of yaw errors can have nearly the same feature value. Furthermore, while the feature curves are similar for the vertical and horizontal shear cases, Figure 2-21 shows that the feature for span is more sensitive in vertical shear, especially for larger yaw errors.

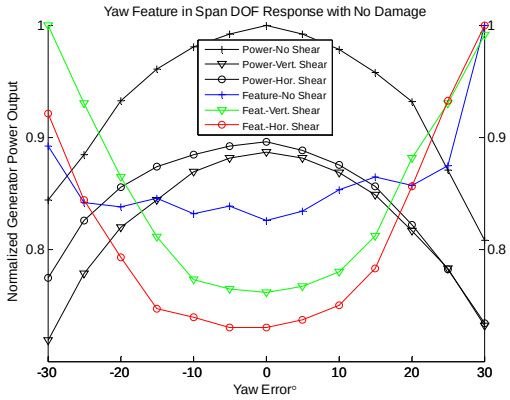

Figure 2-20: Normalized Yaw Feature and Power vs. Yaw Error Angle for Span DOF

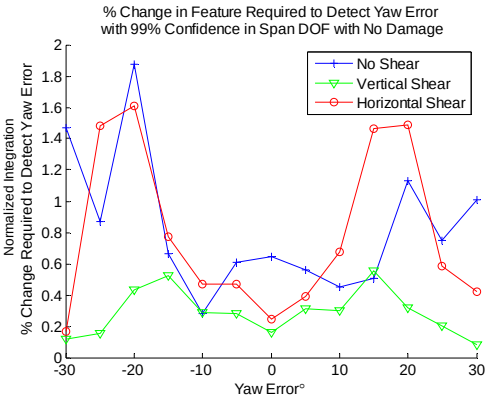

Figure 2-21: Sensitivity of Yaw Feature vs. Yaw Error Angle for Span DOF

Pitch Error Detection

The method was effective at detecting pitch error in the cases of uniform and vertical wind shear conditions, as shown in Figure 2-22. Interestingly, the two feature curves are nearly identical, which can be beneficial in terms of control because the method will work consistently regardless of whether there is uniform or vertically-sheared wind flow. Under the horizontal wind shear condition, the trend followed closely for pitch errors of 15° or higher, but was not as reliable for pitch errors of 0° and 5°, at which the feature value became negative. One possible explanation for this different behavior in horizontal wind shear is that due to the severe wind

profile that was used, the cross-power spectra at the smaller pitch angles were dominated by the 3 rot^{-1} frequency component, so the blade-to-blade differences in the dynamics at $1/rot^{-1}$ were not as pronounced.

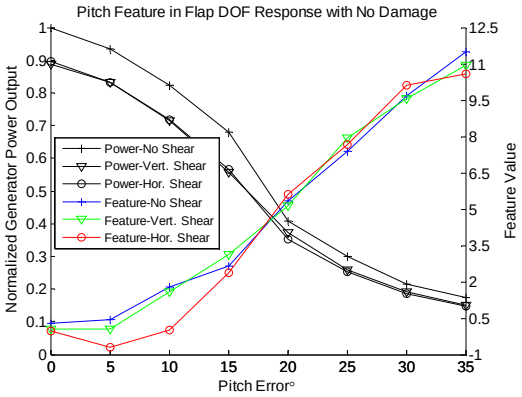

Figure 2-22: Feature Value and Power Curves for Uniform and Vertical Shear Wind Conditions

Note that the other blade DOFs, lead-lag and span, did not exhibit any significant trends in their cross power spectra with any of the nacelle DOFs and therefore were not effective in pitch error detection using this method.

The sensitivity of the pitch feature was very low for 0° and 5°, especially in the vertical and horizontal wind shear cases (Figure 5-8), meaning that a large change in the mean value of the feature is required to detect low pitch errors. This occurred because for low pitch errors, the low mean value of the feature, which is near zero at zero pitch error, is on the order of the standard deviation. Figure 2-24 shows that the sensitivity of this measurement above ten degrees pitch error is fairly high.

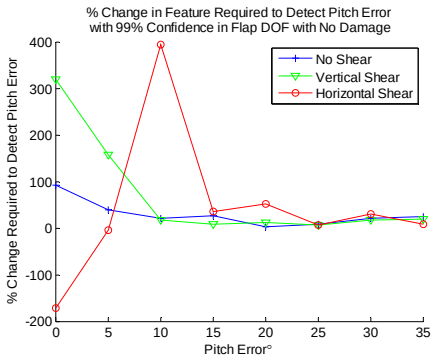

Figure 2-23: Pitch Error Sensitivity

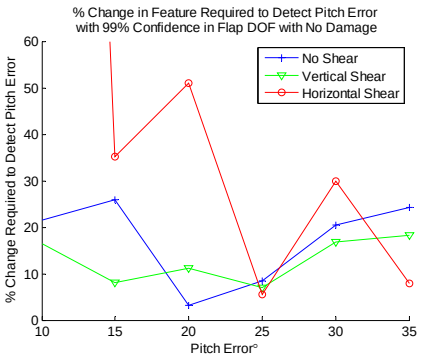

Figure 2-24: Pitch Error Sensitivity (10° to 35°)

Ice Accretion Detection

By using this approach, the change in response due to blade ice accretion was readily identified. The frequency of most interest for damage detection was found to be 3.1Hz; therefore, all damage results correspond to the change in the magnitude of acceleration in the 2 to 4 Hz frequency band of the linear spectra. In the order domain this frequency corresponds to 1 rot^{-1} response of the turbine rotor-dynamics. Additionally, the lead-lag DOF revealed the greatest sensitivity to changes in the rotor-dynamics due to ice accretion.

Detection of Ice Accretion In the Presence of Yaw Error

Figure 2-25 shows the percent change in the magnitude of response in the edge-wise (lead-lag) direction for each blade plotted vs. yaw angle. This plot reveals that ice accretion causes an increase in the edge-wise response in the case of uniform wind flow for all yaw angles. The response of Blade 3 is slightly higher but the overall change in response of each blade is appreciable. For low yaw angles the response of each blade has increased by 15% to 18%. As yaw error increases the percent change in response magnitude for each blade decreases, making the ability to detect ice accretion in the presence of severe yaw error more challenging.

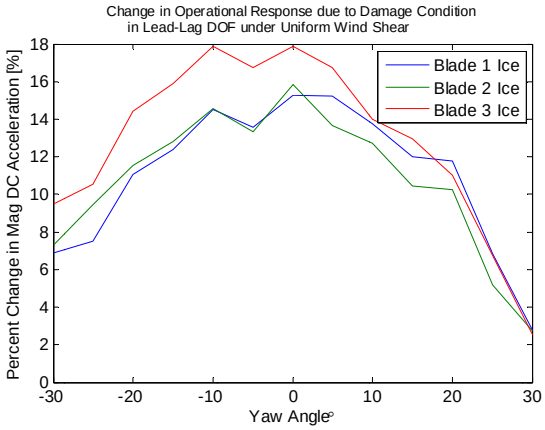

Figure 2-25: Edge-wise percent change in the magnitude of acceleration for each blade vs. yaw angle at 1 rot^{-1} with ice accretion in uniform wind flow.

A similar trend is observed when operating in vertical shear flow. Figure 5-11 illustrates that simulated ice accretion causes the edge-wise response to increase significantly for all three blades. This figure also reveals a large measure of symmetry about 0° yaw position. Similarly, the same increase in response is observed when operating in horizontal shear flow, as illustrated in Figure 2-27. These results suggest that the damage condition can be identified regardless of the wind profile. This result is important for the application of utility-scale wind turbines where vertical and horizontal wind shear conditions can be prominent in wind farms.

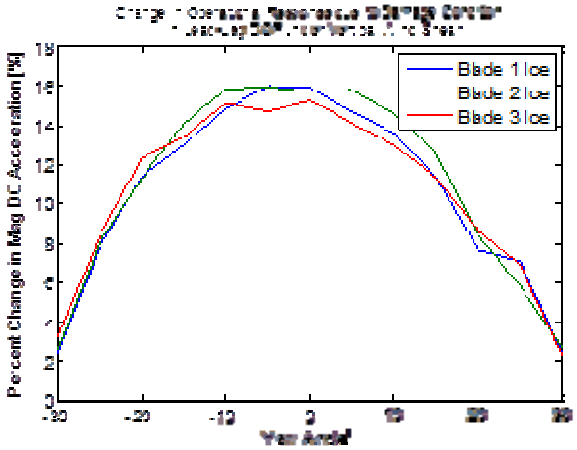

Figure 2-26: Edge-wise change in acceleration for each blade with ice accretion in vertical shear flow

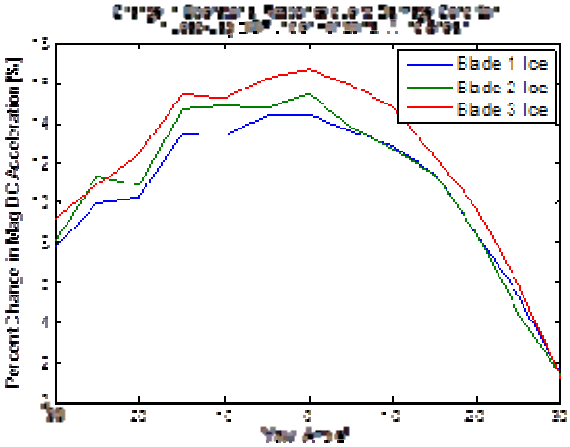

Figure 2-27: Edge-wise change in acceleration for each blade with ice accretion in horizontal shear flow

Detection of Ice Accretion In the Presence of Pitch Error

For the case of pitch error, similar results and trends observed in yaw error were revealed. Figure 5-13 shows the percent change in the magnitude of response in the edge-wise (lead-lag) direction for each blade plotted vs. pitch angle. This plot reveals that ice accretion causes a significant increase in the edge-wise response of each blade across all yaw angles in the case of uniform wind flow. The response of Blade 2 is slightly lower than Blades 1 and 3; however, the overall percent change in the response of each blade exceeded 35% at low pitch angles from 0° to 5°. As pitch error increases the percent change in response magnitude for each blade decreases. For 35° pitch error the percent change in the magnitude of response for all blades coalesces near 26%. This is a desirable result that suggested ice accretion can be detected regardless of the pitch error angle when the wind turbine is operating in uniform wind flow.

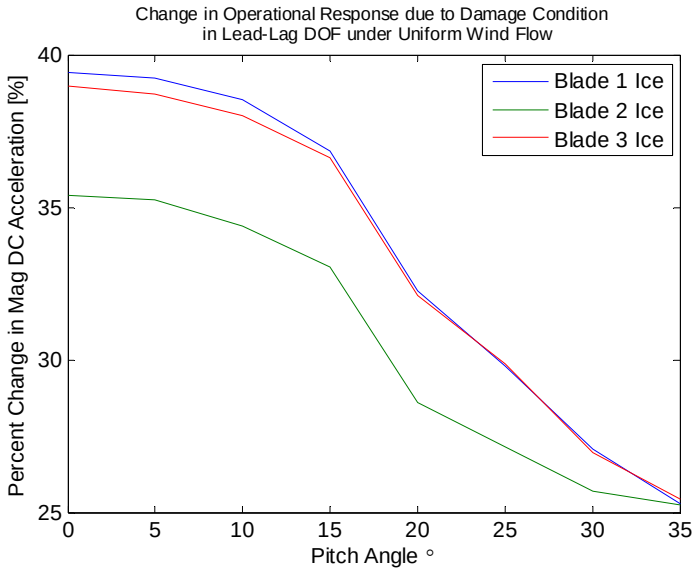

Figure 2-28: Edge-wise percent change in the magnitude of acceleration for each blade vs. pitch angle at 1 rot^{-1} with ice accretion in uniform wind flow.

For the case of a turbine operating in vertical and horizontal shear regimes, the trends observed in Figure 5-13 are similar. Figure 2-29 and Figure 2-30 show the percent change in the magnitude of response in the edge-wise (lead-lag) direction for each blade plotted vs. pitch angle when operating in vertical shear and horizontal shear, respectively. Again, the overall percent change in the response of each blade exceeded 35% at low pitch angles from 0° to 5° and for increasing pitch error the percent change in the magnitude of response of all blades coalesce near 26%. As with detection of ice accretion in the presence of yaw error, these results suggest that the damage condition can be identified regardless of the wind profile or pitch error.

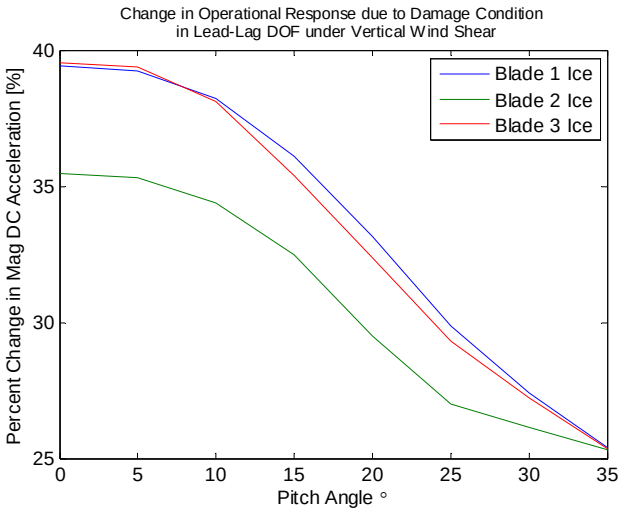

Figure 2-29: Edge-wise percent change in the magnitude of acceleration for each blade vs. pitch angle with ice accretion in vertical shear flow.

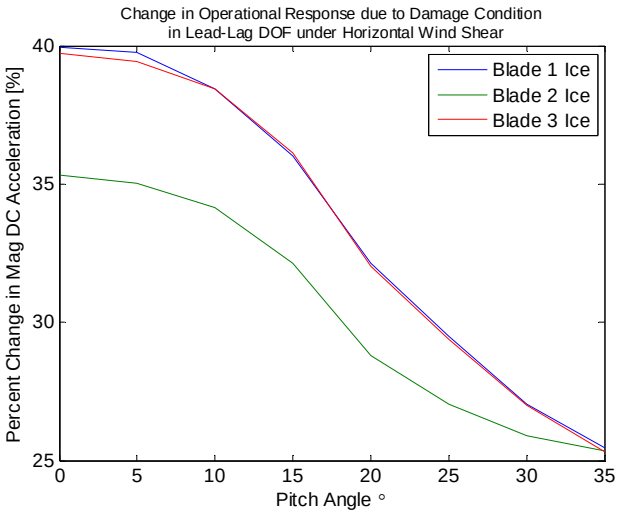

Figure 2-30: Edge-wise percent change in the magnitude of acceleration for each blade vs. pitch angle with ice accretion in horizontal shear flow.

Damage Detection

In the case of blade root damage, the method was applied and revealed that the flap degree of freedom near 7 Hz emphasized the change in response due to the damage condition. In the order domain this frequency corresponds to 2 rot^{-1} dynamics of the turbine. Recalling Figure 2-9, the rotor experiences a 2 rot^{-1} oscillation in wind speed as it moves through one full rotation. At this rotational frequency the reduced stiffness in the root of the blade is most sensitive to the 2 rot^{-1} fluctuations in the flap DOF; therefore all damage results correspond to the change in the magnitude of acceleration between blades at this order.

Root Damage Detection in the Presence of Yaw Error

Figure 2-31 shows the change in blade-to-blade response ratio for varying yaw error when operating in a uniform wind flow. The damaged blade (Blade 3) causes the blue and green curves to exhibit the largest changes whereas there is negligible change near zero yaw error for the undamaged blade-to-blade response ratio (red curve). The undamaged blade-to-blade response ratio exhibits symmetry about zero yaw with a slight increase in response due to the change in yaw position near -10° and 15°. Figure 2-32 shows a similar trend for the blade-to-blade response ratio when operating under vertical wind shear. In this wind regime the 2 rot^{-1} dynamics are more pronounced due to the shear profile. Again, the blue and green curves exhibit the largest changes whereas there is negligible change for the undamaged blade-to-blade response ratio (red curve). Similar traits are observed in Figure 2-33 for a turbine operating under horizontal wind shear. However, the curves now increase for negative yaw error and the undamaged blade-to-blade response (red curve) has lost the symmetry about zero yaw, but does maintain an appreciably smaller magnitude when compared to the blade-to-blade response ratio with damage present. Recalling Figure 2-9, at negative yaw error for horizontal wind shear the rotor plane is oriented in an increased wind flow and therefore experiences an increase in response for negative yaw error. The increased blade-to-blade response ratio for negative yaw error is an artifact of the horizontal wind shear and yaw position combined. Regardless, the blade-to-blade response ratio method identifies root damage in the presence of yaw error. The

advantage of this method is that no historical baseline response data is needed to make these comparisons to determine if damage is present.

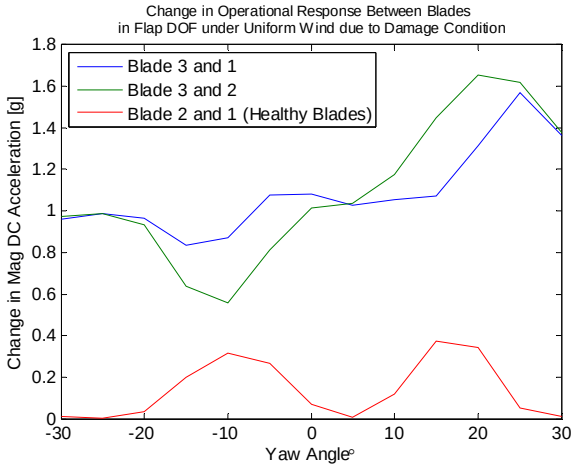

Figure 2-31: Comparison of the change in operational response between blades vs. yaw angle at 2 rot^{-1} for the flap DOF in uniform wind flow when damage is present in a single rotor blade (Blade 3).

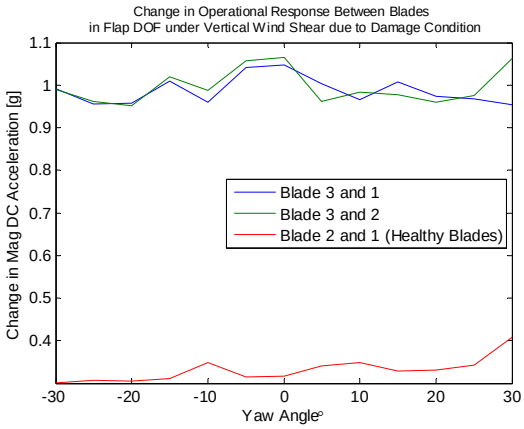

Figure 2-32: Comparison of change in operational response between blades vs. yaw angle for the flap DOF in vertical shear wind flow when damage is present in a single blade (Blade 3).

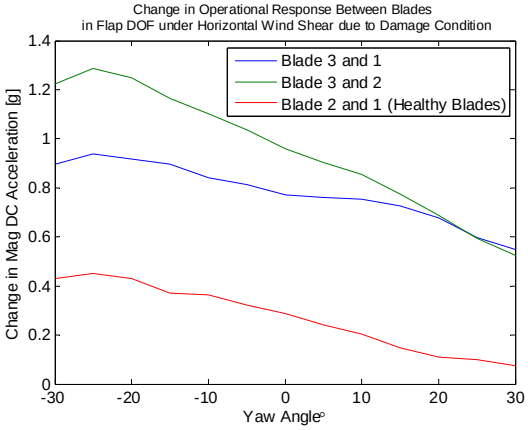

Figure 2-33: Comparison of change in operational response between blades vs. yaw angle for the flap DOF in horizontal shear flow when damage is present in a single blade (Blade 3).

Root Damage Detection in the Presence of Pitch Error

As with yaw error, similar trends are observed in the blade-to-blade response ratios to identify damage in the presence of changing pitch angle. Upon first inspection of the blade-to-blade response ratios for each wind regime an obvious trend emerged; the change in response amplitude for the blade pairs with the damaged blade (Blade 3) increased significantly beyond a 15° pitch angle. To understand if this trend was due to the damage condition of Blade 3 or due to the change in pitch of Blade 3, the blade-to-blade response ratios were plotted for the case of no damage and only the pitch angle of Blade 3 was altered. Figure 5-19 shows the results of this plot. The figure reveals that for pitch angles from 0° to 15° the change in the blade-to-blade

response ratios for all blade pairs is negligible; i.e. damage is not present. However, for pitch angles beyond 15° the blade-to-blade response ratios for the blade pairs with the pitched blade (Blade 3) increases significantly. This demonstrates a reduced sensitivity of this methods ability to determine damage in the presence of pitch angles beyond 15°. This observation is exemplified in Figure 2-35. This figure shows the change in blade-to-blade response ratio for increased pitch error when operating in a uniform wind flow. The damaged blade (Blade 3) causes the blue and green curves to exhibit the largest changes whereas there is negligible change for the undamaged blade-to-blade response ratio (red curve). At pitch angles greater than 15° the change in the blade-to-blade response ratio is dominated by the change in pitch angle of Blade 3. Figure 2-36 shows a similar trend for the blade-to-blade response ratio when operating under vertical wind shear and in Figure 2-37 for a turbine operating under horizontal wind shear. Again, the blue and green curves exhibit the largest changes whereas there is negligible change for the undamaged blade-to-blade response ratio (red curve).

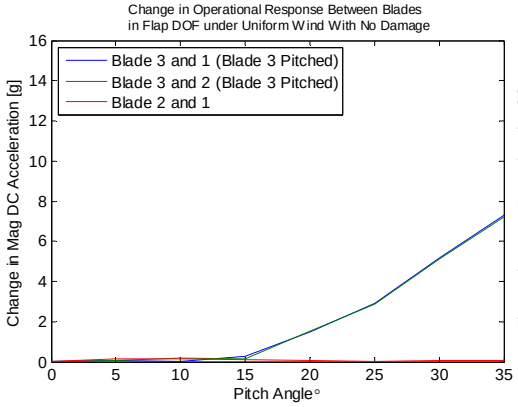

Figure 2-34: Comparison of the change in operational response between blades vs. pitch angle at 2 rot^{-1} for the flap DOF in uniform wind flow without the presence of damage.

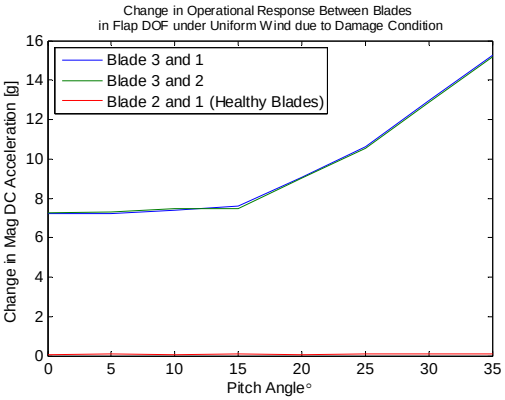

Figure 2-35: Comparison of change in operational response between blades vs. pitch angle at 2 rot^{-1} for flap DOF in horizontal shear flow when damage present in single blade (Blade 3).

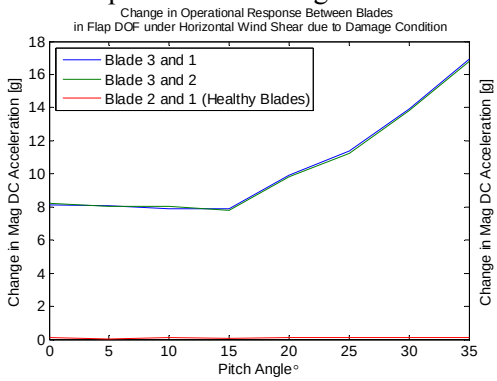

Figure 2-36: Comparison of change in operational response between blades vs. pitch angle for flap in horizontal shear when damage in Blade 3

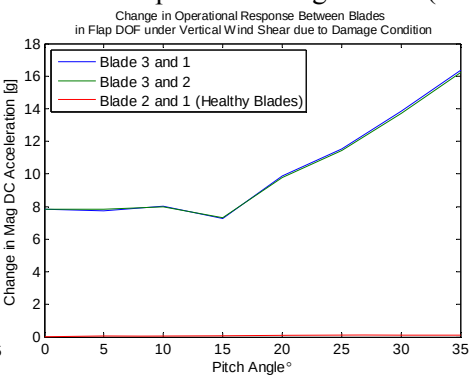

Figure 2-37: Comparison of change in operational response between blades vs. pitch angle for flap in vertical shear flow when damage in Blade 3

CONCLUSIONS

Experiments were conducted on a small horizontal axis wind turbine by controlling the inflow conditions and measuring the inertial response of the rotor blades as a function of yaw

error, pitch error, and simulated damage conditions (ice accretion and blade root crack). Using cyclic averaging in conjunction with operational modal analysis techniques, it was demonstrated that the sensitivity of the measured blade flap and lead-lag acceleration responses to yaw error was larger in the presence of vertical wind shear than in the case of uniform flow, but smaller in the presence of horizontal wind shear. It was also shown using these same operational blade acceleration measurements that the presence of either horizontal or vertical shear inflow conditions makes it possible to distinguish between positive and negative yaw error, which would be important for controlling yaw error in practice. In contrast, the measured blade acceleration responses did not exhibit a significant sensitivity to a single blade pitch error. Although the small-scale wind turbine blade that was tested has a substantially different aerodynamic profile than a utility-scale blade, the measurement technique and data analysis methodology are general and can translate well to utility-scale blades.

It was also shown that ice accretion could be detected using the lead-lag operational blade acceleration measurements at a frequency of one per revolution regardless of the yaw error and regardless of the inflow condition (vertical or horizontal wind shear). The percent change in the lead-lag acceleration response at this frequency was 35%. Likewise, the percent change in the lead-lag response was again 35% for pitch errors less than 5 degrees, and the presence of ice could be detected regardless of pitch error. For the case of a simulated blade root crack, the flap acceleration response of the blade showed the most sensitivity to the simulated damage. The presence of the faulty blade could be detected regardless of the yaw/pitch error and regardless of the inflow conditions.

The results of this investigation indicate that blade operational acceleration responses in conjunction with operational modal analysis techniques are a promising means of detecting and characterizing yaw error and certain blade damage conditions. The experiments demonstrate that the data analysis procedure is capable of extracting features that can detect errors in yaw and pitch as well as simulated damage conditions despite significant variations in the wind inflow conditions, which is an important finding given that such variations are prevalent in utility-scale wind farms.

REFERENCES

Adams, D. E. (2007). *Health Monitoring of Structural Materials and Components.* Chichester, UK: John Wiley & Sons, Ltd.

Adams, D. E., White, J., Rumsey, M., & Farrar, C. (2011, May). Structural health monitoring of wind turbines: method and application to a HAWT. *Wind Energy, 14*(4), 603-623.

Barber, S., & Golbeck, P. (2010). *Wind Turbine Maintenanceand Condition Monitoring.* World Wind Energy Association.

Beattie, A. G. (1997). Acoustic Emission Monitoring of a Wind Turbine Blade during Fatigue Test. *Prof of AIAA*, (p. 10).

Burton, T. D. (2001). *Wind Energy Handbook.* John Wiley and Sons.

Chauhan, S., Martell, R., Allemang, R. J., & Brown, D. L. (2007). Unified Matrix Polynomial Approach for Operational Modal Analysis. *IMAX-XXV.* Orlando.

Ciang, C. C., Lee, J., & Bang, H. (2009). Structural Health Monitoring for a Wind Turbine System: a review of damage detection methods. *Meas. Sci. Technol*, 20.

Echavarria, E., Hahn, B., van Bussel, G. W., & Tomiyama, T. (2008, August). Reliability of wind turbine technology through time. *Journal of Solar Energy Engineering, 130*.

Farret, F. A., Pfitscher, L. L., & Bemardon, D. P. (2000). Active yaw control with sensorless wind speed and direction measurements for horizontal axis wind turbines. *Proceedings of the Third IEEE International Caracas Conference on Devices, Circuits and Systems* (pp. I25/1-I25/6). IEEE.

Flemming, M. L., & Troels, D. (2003). New lightning qualification test procedure for large turbine blades. *International Conference Lightning and Static Electricity*, (pp. 36.1-10). Blackpool.

Ghoshal, A., Dundaresan, M. J., Shulz, M. J., & Pai, P. F. (2000). Structural Health Monitoring Techniques for Wind Turbine Blades. *Journal of Wind Engineering and Industrial Aerodynamics*, 85.

Hahn, B., Durstewitz, M., & Rohrig, K. (2007). *Wind Energy (Reliability of Wind Turbines Experiences of 15 Years with 1,500 W) ed J Peinke et al, Springer, Berlin.* Berlin: Springer.

Hameed, Z., Hong, Y. S., Cho, Y. M., Ahn, S. H., & Song, C. K. (2009). Condition monitoring and fault detection of wind turbines and related algorithms: a review. *Renewable and Sustainable Energy Reviews*, 1-39.

Homola, M. C., Nicklasson, P. J., & Sundsbo, P. A. (2006). Ice sensors for wind turbines. *Cold Regions Science and Technology*, 125-131.

Hyers, R. W., McGowan, J. G., Sullivan, K. L., Manwell, J. F., & Syrett, B. C. (2006). Condition monitoring and prognosis of utility scale wind turbines. *Energy Materials, 1*(3), 187-203.

Jureczko, M., Pawlak, M., & Mezyk, A. (2005). Optimisation of Wind Turbine Blades. *Journal of Material Processing Technology 167*, 463-471.

Larsen, G. C., Hansen, M. H., Baumgart, A., & Carlen, I. (2002). *Modal Analysis of Wind Turbine Blades.* Denmark: Riso National Laboratory.

Luczak, M., Peeters, B., Dohler, M., Mevel, L., Ostachowicz, W., Malinowski, P., et al. (2010). Damage Detection of Wind Turbine Blade Panels Using Three Different SHM Techniques. *Proc. of IMAC-XXVIII.* Jacksonville.

Mcniff, B. (2006). *Wind Turbine Gearbox Relability.* Albuquerque, NM: Sandia National Labs.

Musial, W., Butterfield, S., & Mcniff, B. (2007). Improving Wind Turbine Gearbox Reliability. *2007 European Wind Energy Conference.* Milan, Italy.

Rau, S. S. (1995). *Mechanical Vibrations.* Addison-Wesley Publishing Company.

Robinson, M. C., Hand, M. M., Simms, D. A., & Schreck, S. J. (1999). Horizontal axis turbine aerodynamics: three dimensional, unsteady, and separated flow influences. *3rd ASME/JSME Joint Fluids Engineering Conference.* San Fransisco, CA.

Seifert, H. (2003). *Technical Requirements for Rotor Blades Operating in Cold Climate.* Wilhelmshaven: Deutsches Windenerdie-Institut.

Shih, C. Y., Tsuei, Y. G., Allemang, R. J., & Brown, D. L. (1989). Complex Mode Indicator Function and its Applications to Spatial Domain Parameter Estimation. *Proc. of IMAC-VII.* Las Vegas.

Tammelin, B., & Seifert, H. (2001). Large Wind Turbines Go Into Cold Climate Regions. *European Wind Energy Conference.* Copenhagen.

Van Hemelrijck, D., Smits, A., & Philippidis, J. (2006). Study of the Behaviour of Glass Fibre Reinforced Epoxy Composite System used for Wind Turbine Rotor Blades under Biaxial Load Conditions. *Proc. of Eur. Wind Energy Conf. Exhibition 2006.* Athens.

White, J. R. (2010). *Operational monitoring of horizontal axis wind turbines with inertial measurements.* West Lafayette, IN: Purdue University.

White, J., Adams, D. E., Rumsey, M., & Zayas, J. (2009). Measurement of Operational Loading and Deflections with a Smart Turbine Rotor Blade. *Windpower.* Chicago.

Yutzy, J. (2011). *Characterizing the Structural Dynamic Response of a Horizontal Axis Wind Turbine in a Yawed Flow Field using Rotor and Nacelle-Mounted Inertial Sensors.* West Lafayette: Purdue University.

Zayas, J. R., Roach, D. P., Rumsey, M. A., Allan, W. R., & Horsley, D. A. (2007). Low-Cost Fiber Bragg Grating Interogation System for in situ Assessment of Structures. *Proc. of SPIE, Vol 6529*, (pp. 65293C.1-65293C.12).

APPENDIX D. VAWT and SCADA System at Purdue Calumet

1. Design of Vertical Axis Wind Turbine Platform

The physical components of the system contain the following: VAWT, three phase rectifier, power inverter, high definition camera, weather instruments that include three anemometer/vane combinations and data logger, 3D ultrasonic anemometer, 2D ultrasonic anemometer with relative humidity and air temperature, Supervisory Control And Data Acquisition (SCADA) System, remote inputs and outputs (I/O), power monitor, and a server. The system was designed with an open architecture to make it flexible now and in the future. The design incorporates the following features: expandable inputs and outputs (I/O), interchangeable hardware and sensors, data access from multiple devices and programs, and multiple graphic user interfaces to display data. Refer to the Wind Turbine System Overview Diagram in Figure 1.

1.1 Wind Turbine and Main System Components

An EddyGT vertical axis wind turbine (VAWT) was installed on a two meter tower on the roof of the Student Union Library Building (SUL), see Figure 2. Two of the three anemometers used for measuring wind speed are also shown in Figure 2. The wind turbine electrical system consists of a 1.0 kilo watt three phase permanent magnet synchronous generator (PMSG), a 7.2 KW three-phase rectifier, and a 4.2 KW two input power inverter. The generator is at the base of the wind turbine, see Figure 3. The rectifier and inverter are in the foreground of Figure 4. The power generated by the wind turbine is connected to a single split phase 208 V power grid. In Figure 4, the large gray enclosure houses the majority of the SCADA equipment and the remote I/O enclosure, weather data logger enclosure, and disconnects switches.

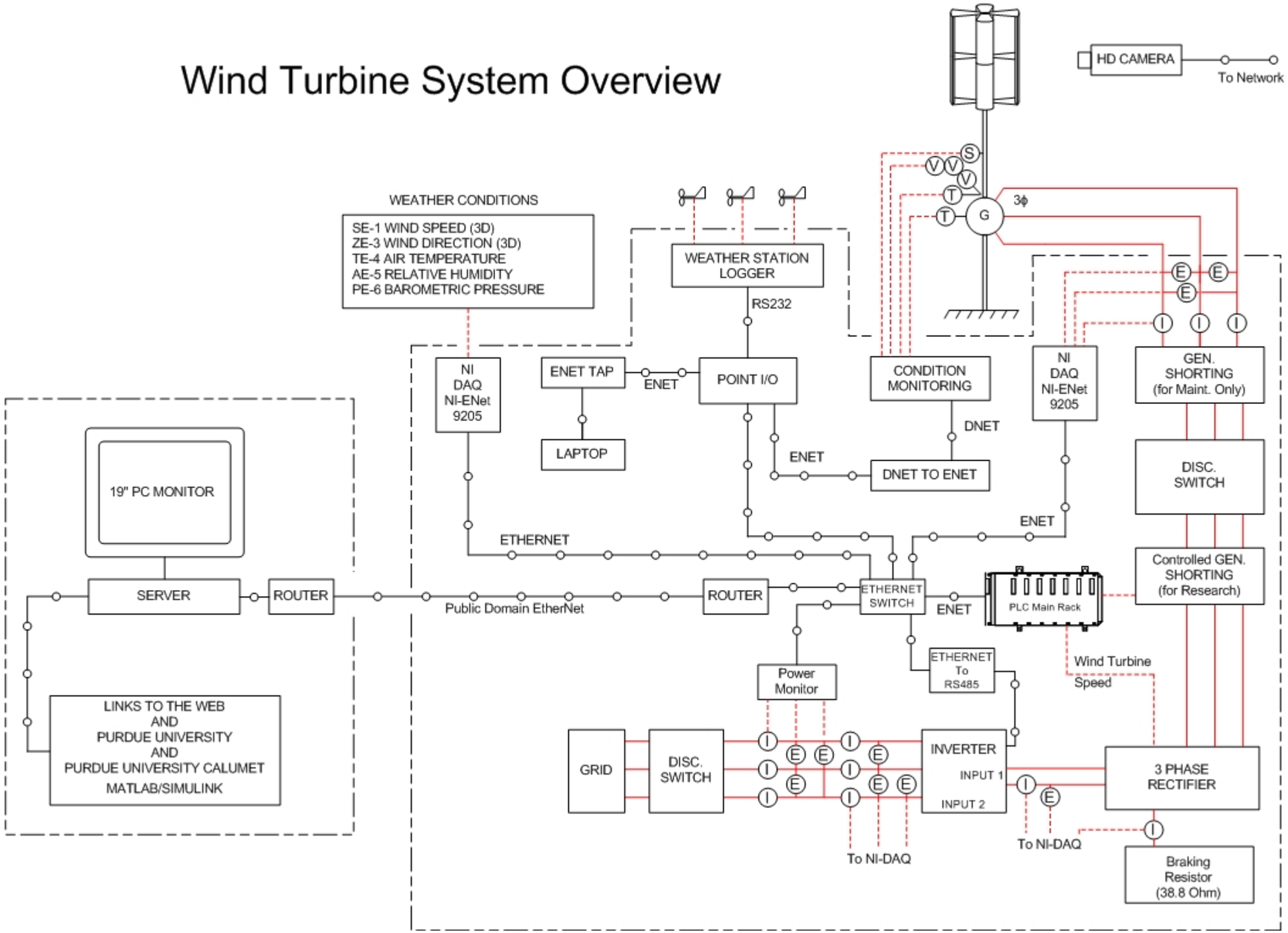

Figure 1: Wind turbine system overview diagram.

Figure 2: Wind turbine and anemometers with vanes on roof of SUL building.

Figure 3: Bottom view of the wind turbine and generator.

Figure 4: Electrical panel below wind turbine.

1.2 Physical Conditions of Wind Turbine

Vibration, shaft speed, and temperature will be monitored by the Allen Bradley condition monitoring system. Vibrations are monitored by three accelerometer sensors placed in the X, Y, and Z axis. Thermocouples are used to monitor temperature and a Hall-Effect speed sensor is used to measure the physical rotational speed of the turbine. The system will determine if an alarm condition occurs or if the wind turbine needs attention. All the data in the Condition Monitoring system is monitored by the programmable logic controller (PLC) allowing it to notify and apply the dynamic brake if necessary. The Condition Monitoring system will benchmark the wind turbines present vibration and analyze any changes in the future.

1.3 Weather Sensors and Data

The system will monitor weather data in real time and also provide a short time duration average. The real time data will be monitored by the National Instrument analog module 9205 that has 16 differential inputs with a sample rate of approximately 7 kilo samples per second per channel. The real time weather data will be used to estimate the available power from the wind and will be later compared to the real time power calculations. The real time weather inputs will come

from the following sensors; 3D Ultrasonic Anemometer (wind speed and direction), 2D Ultrasonic Anemometer (wind speed and direction), Air Temperature, and Relative Humidity. The 3D Ultrasonic anemometers have no moving parts and will give a better representation of the wind speed and direction than the anemometer/vane and will help in the valuation of the wind model.

The average weather data is collected from a weather station data logger. The data logger is a RainWise® WeatherLog that has three combination anemometers and directional vanes connected to it. These anemometers can be easily positioned at different locations and elevations around the wind turbine. The WeatherLog stores a selectable average time duration and logs the time, date, wind speed, wind direction, and wind gust for each anemometer and vane. This data is also monitored and collected by the Allen-Bradley ControlLogix® PLC every second via the RS232 serial port of the WeatherLog to the Allen-Bradley Point I/O RS232 ASCII module.

1.4 Camera Monitoring and Promotion

A high definition Ethernet camera is mounted on the roof to monitor the status of the wind turbine day and night. The camera will also help in promoting wind energy program at Purdue University Calumet, the Department of Electrical and Computer Engineering, the Department of Mechanical Engineering, and the Center for Innovation through Visualization & Simulation (CIVS). The camera is on a separate network so not to overload the data network of the SCADA system.

1.5 Supervisory Control and Data Acquisition (SCADA) System

The SCADA system design consist of Rockwell Automation FactoryTalk® Graphic User Interface (GUI) software (Figure 5), Allen-Bradley; ControlLogix® PLC, Point I/O, Condition Monitoring, Power Monitor PM3000, and their respective software packages. National Instrument ENET-9205 analog modules communicating over Ethernet are used independently from the main SCADA system for real-time data acquisition and graphic user interface, see Figure 6. The GUI can be created using LabVIEW® or MATLAB®, see Figure 7.

At the heart of the SCADA is the Allen-Bradley ControlLogix® PLC with a L62 processor version 19. The PLC processor is programmed with IEC 61131 – 3 Standard which contains the following five programming languages; Ladder (LD), Sequential Function Chart (SFC), Function Block Diagram (FBD) seen in Figure 8, Structured Text (ST), and Instruction List (IL). A MATLAB® modeling programming can be used to program the Allen Bradley's processor, but only in structured text.

The processors database is a 32-bit tag base system having local and global tags which use aliases and values in engineering units, similar to what the distributed control systems use.

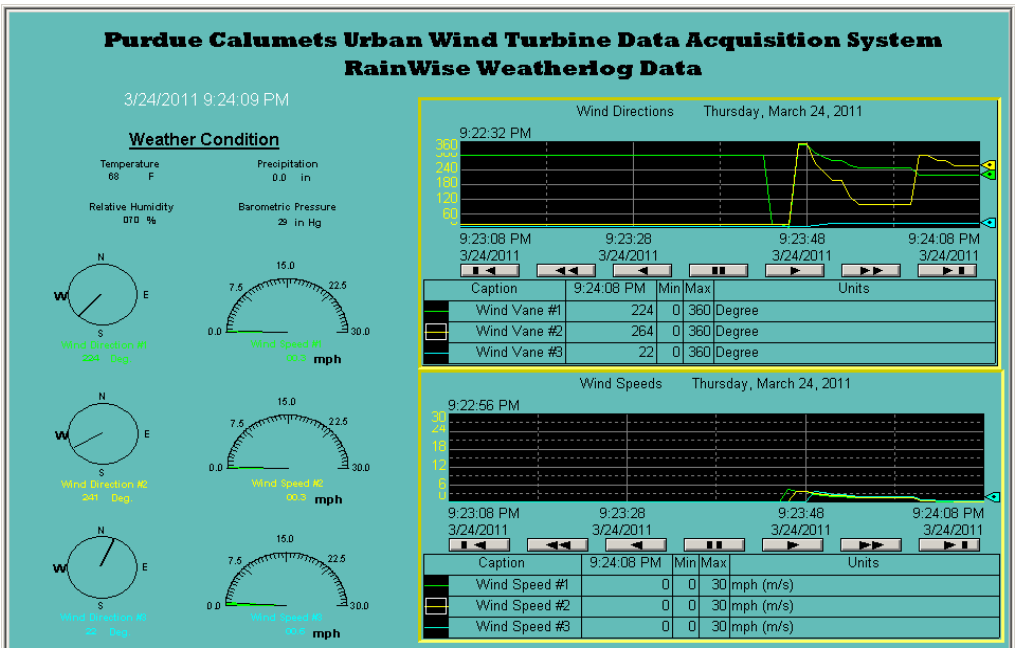

Figure 5: Rockwell Automation FactoryTalk® GUI.

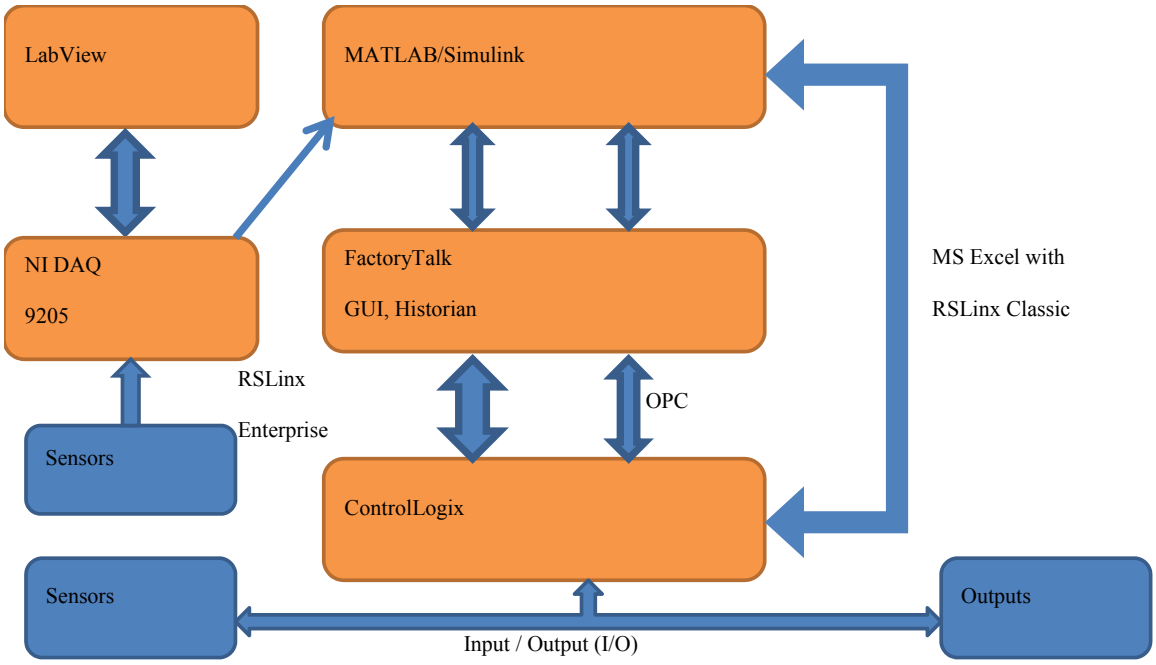

Figure 6: Block diagram of system platform.

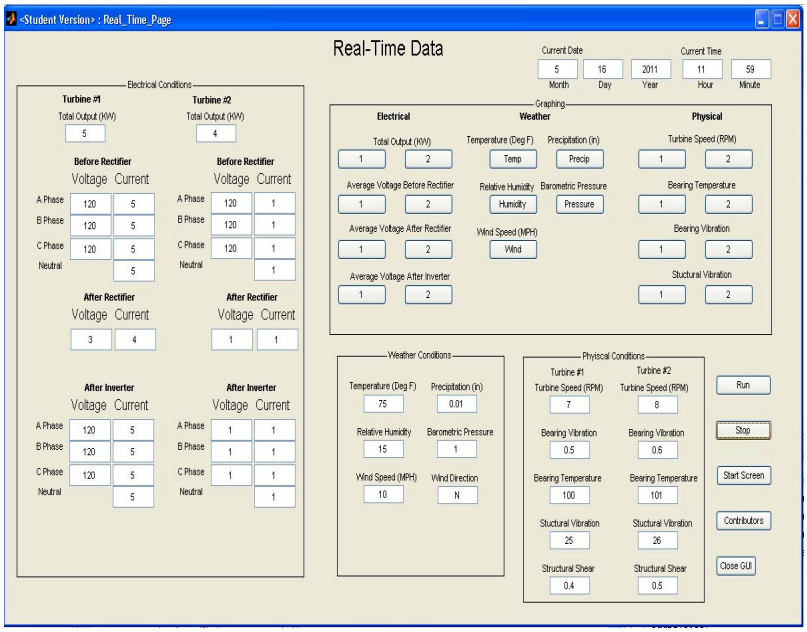

Figure 7: MATLAB® GUI.

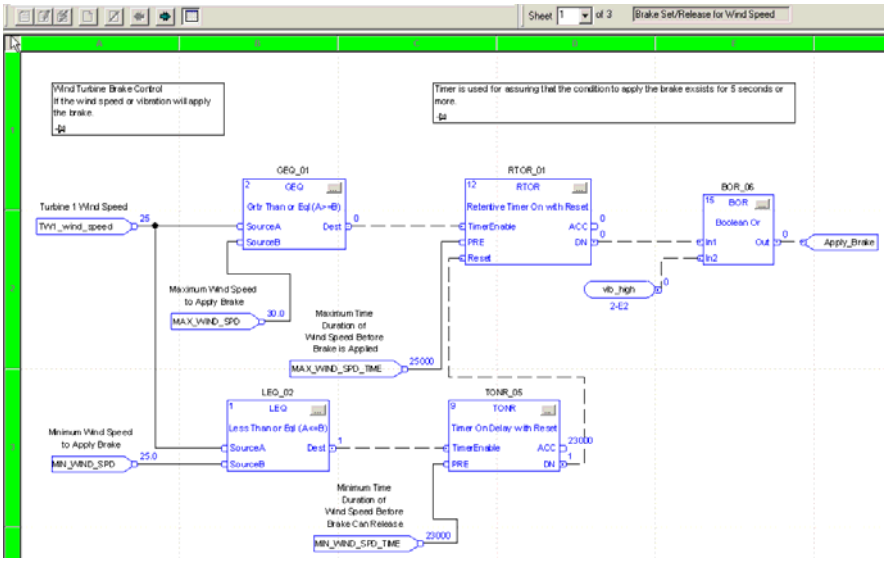

Figure 8: PLC function block programming brake control.

1.6 Communications Network

The communication network configuration is provided through Ethernet, DeviceNet, and Serial communication protocols. All DeviceNet and Serial highways will be converted to Ethernet including Point I/O, Condition Monitoring, and serial connection from power inverter. An Ethernet linear and Star topology is used in this system. The linear topology will connect the remote I/O and Condition Monitoring system to the PLC. The star topology will connect the PLC, power monitoring, National Instrument modules, and power inverter to the campus public domain.

1.7 Electrical Sensors

Hall-Effect current sensors (see Figure 9) are used for real-time current sensing of the three-phase generator, rectifier, load dumping or dynamic braking resistor, and the power inverter.

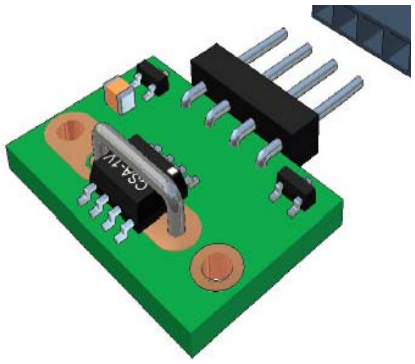

Figure 9: Hall-Effect current sensor.

Three-port voltage isolators are used for the real-time voltage sensing of the three-phase generator, rectifier, and power inverter.

Three current transformers (CT) are used to sense the output current of the power inverter.

1.8 Historical Archiving of data

Due to the flexibility of the system, data can be historically archived by Rockwell Automation FactoryTalk®, MATLAB®, Allen-Bradley RSLinx® linked to Microsoft Excel® spreadsheet, or from the National Instrument hardware and software.

2. The effect of the wind turbine SCADA system on the future curriculum development at Purdue Calumet

2.1 Power Electronics

The platform enhances the Power Electronics course by providing students real-world application experience with three-phase rectifiers and single phase inverters. The wind turbine will be used throughout the semester for an ongoing series of examples. Presented and discussed during lectures will be the three-phase voltage signals produced by the wind turbine's generator at different wind speeds, the DC voltage signal produced by the rectifier, and the single-phase AC signal produced by the inverter. Students will see firsthand how wind turbines create time varying non-ideal three-phase sinusoidal signals, rectifier efficiency and waveform varies with input, and the resulting effect on inverter output. Using MATLAB® and actual wind turbine signals for laboratory and homework assignments, students will determine how the fundamental frequency and harmonics of the voltage signals change with wind speed. They will determine the effect of transients and harmonics on the rectified and inverted signal and the variation of rectifier and inverter efficiency with input. By viewing the variation with wind speed of the VAWT generator's signal students will understand the need for a rectifier and inverter as part of any grid tied wind turbine system. Also, they will better understand that rectifiers and inverters are not ideal.

2.2 Electric Drives

The platform enhances the Electric Drives course by providing students real-time sensor data of the electric generator's output voltages and currents together with the shaft speed measurement. The collected data on the machine side will be used for laboratory assignments to validate and refine the Simulink/MATLAB® models of the permanent magnet synchronous machine in the generator operation mode. The same data will also be used in the laboratory to analyze and derive the machine's specific characteristics and to evaluate its performance.

2.3 Power Systems

The platform enhances the Power Systems course by demonstrating the practical use of power monitoring equipment and software and by providing post processing data for power quality analysis. One of the student projects for this course consists of: using the inverter's current and voltage waveforms at the point of common coupling (on the grid side), exporting it to MATLAB® where a harmonic analysis will be performed, with the final goal being the design of a trap filter in order to mitigate the most significant harmonics that "pollute" the grid. In a second project, the real-time data collected on the machine side will be used for students to draw practical conclusions allowing them to complete an enhanced electric generator redesign. The ability to capture the voltage and current transients caused by wind speed variations, inverter switching operation, and by connecting and disconnecting the wind turbine system to the grid, generates valuable informative data for students learning electric Power Systems. Data displaying these transients will be presented and discussed during lectures.

2.4 Advanced Electric Drives

The platform enhances the Advanced Electric Drives course by providing students with real-time data for validating and refining the models of the wind turbine system consisting of: the wind turbine, electric generator, power electronic converters, and grid system. For a project, students will design an advanced vector control systems for wind turbine power generation.

2.5 Industrial Automation

The platform enhances the Industrial Automation course by providing students with a real world example of a supervisory control and data acquisition system (SCADA), graphic user interface (GUI), communications, open architecture, multiple programming languages, tag base system, I/O systems, sensor selection, and signal conditioning. Homework assignments will be given to enhance the understanding of components at each level of the system and how they communicate within the system. In addition homework concerning sensors selection and required signal conditioning will be assigned. Laboratory experiments and projects will be given to expose the student to programming standard IEC–61131–3 for the programmable logic controller (PLC) and to help the student to understand the philosophy of programming between the GUI and the PLC.

Wind Analysis, Purdue Micro Wind Farm & Simulation

This appendix contains the met tower data, the Purdue Reconfigurable Micro Wind Farm, and the wind farm Simulation.

Met Tower Data

Wind speeds were recorded in West Lafayette, Indiana from October 1st, 2008 to December 31st, 2009 and analyzed to determine the wind speed trends both throughout the year and throughout the day. A Weibull function is fit to the data and its accuracy proven in the quality of the Weibull calculated average wind speed. The five anemometer height locations are used to describe the atmospheric velocity profile, which is studied to understand its trends. The wind speed data is used to calculate performance for both residential and utility-size wind turbines. Two leading manufacturers of small wind turbines are compared at varying hub heights, and three utility size wind turbines from one manufacturer are compared which vary in rotor diameter and generator size.

Data Acquisition

Measurements were taken from the tower using (6) NRG Systems #40C anemometers, (2) NRG #200P wind direction vanes, and an (1) NRG #110S Temperature Sensor with Radiation Shield. Positions for these sensors are displayed in table below, and all wind sensors were installed using a 20" mounting boom. Data was acquired and stored by an NRG Symphonie 12-channel Data Logger.

Sensor	Height (meters)	Orientation (degrees)
Anemometer	50	270
Anemometer	50	180
Anemometer	40	270
Anemometer	30	270
Anemometer	12	180
Anemometer	3	180
Direction Vane	50	0
Direction Vane	40	0
Thermometer	1	N/A

The data set was taken from October 1, 2008 to December 31, 2009. Data points are in the form of ten minute averages performed on each of the sensor channels, calculated from the interval's data set which included data sampled every two seconds. The mean and standard deviation were recorded for this ten minute period, along with the maximum and minimum values for the sensor. The data collection procedure resulted in 144 total data points for each day, with 457 days in the data set viewed.

Data Analysis

For this analysis the ten minute data points were sampled using a moving average scheme with the index value being the center of that bin. The data was placed into bins where divisions of both the number of days and number of hours could be made to group the data. For this analysis, the number of days in a bin range from 1 to 90, and hour divisions used are for a whole

day (24 hours) and down to every hour. This sampling was performed to add insight into the seasonal trends, those that vary with date, and the daily trends, those that vary within each day, of the wind data.

The statistical characteristics of the wind were determined using a Weibull probability estimation. The Weibull function is a two parameter distribution which describes the probability of a certain wind speed occurring. The parameters describe the shape or spread, k, and the scale, c, of the distribution. The shape factor is said to vary from 1.5 to 3 [1] for most wind conditions and describes the variability of the wind.

$$f(V) = \left(\frac{k}{c}\right) \times \left(\frac{V}{c}\right)^{k-1} \times exp\left[-\left(\frac{V}{c}\right)^{k}\right]$$

From this distribution, two important wind speeds are derived; the most probable and the wind speed carrying maximum energy. The most probable wind speed occurs at the peak of the Weibull distribution and is described by the following relation:

$$V_{MP} = c\left(\frac{k-1}{k}\right)^{1/k}$$

The wind speed which carries the maximum energy will always occur at a higher value than the most probable wind speed. The power in the wind is proportional to the wind speed cubed, balancing with the lower frequency of higher wind speeds to produce the energy maximum. This wind speed is of particular interest to the wind turbine designer, and is described by the following relation:

$$V_{MAX,E} = c\left(\frac{k+2}{k}\right)^{1/k}$$

Total power production in the wind can be estimated using this distribution and known parameters for the period of interest as follows (with Γ representing the gamma function):

$$\frac{P_W}{A} = {}^1\!/_2\,\rho \times \Gamma\left[c^3\left(1+\frac{3}{k}\right)\right]$$

The five height locations of the anemometer tower were used to describe the atmospheric velocity profile below the 50 m height. The power law profile shape assumption was used in this calculation due to its simplicity and the relatively low height of the tower. Calculation for this parameter was made in the raw data at each point before sampling. The power coefficient was determined from the 6 data points using a polynomial fitting tool which minimized error in ($\ln V$) and not (V) itself. This analysis was performed with acceptable agreement. The power law profile is as follows:

$$\frac{V}{V_{ref}} = \left(\frac{z}{z_{ref}}\right)^{\propto}$$

The particular interest of this study of the yearly wind conditions is its interplay with wind turbine operation. This determination begins with the wind turbine power calculation, and the normalized performance measures of capacity factor and power coefficient are then derived. Wind turbine power production is calculated using the actual, non-sampled, wind speed and the wind turbine of interest's power curve. For this study two of the leading wind turbines in the "small wind-turbine" classification (<100kW) are compared, along with a generic wind turbine power curve following its accepted definition. This standard power wind turbine power curve is described below [1], where V_C, V_R, V_F, and P_R all describe the wind turbine performance and are

the cut-in speed, rated-speed, cut-out speed, and rated power. The exponent n describes the power relationship and has a value between 2 and 3.

$$P_T(V_W) = \begin{cases} 0 & V_W < V_C \\ P_R\left(\dfrac{{V_W}^n - {V_C}^n}{{V_R}^n - {V_C}^n}\right) & V_C \le V_W \le V_R \\ P_R & V_R < V_W \le V_F \\ 0 & V_W > V_F \end{cases}$$

The performance measure of capacity factor, CF, is simply the percentage of the rated, name-plate, value of power production that is produced over a period of time. This value was calculated from the full data set and then sampled to smooth out the curve as desired and to gain insight into the seasonal and daily trends.

$$CF = \frac{P_T}{P_R}$$

The power coefficient was calculated and sampled in the same manner as capacity factor. This measure is the amount of power produced as a percentage of the total power in the wind. The amount of power in the wind follows the relation in the denominator below. The machine's efficiency of power capture and conversion is measured by this value.

$$C_p = \frac{P_T}{{}^1\!/_2\,\rho A_T {V_W}^3}$$

Results

The data set for the wind speed is reduced through averaging in order to remove some of the inherent stochastic properties of wind and to reveal more of the overall seasonal and daily trends. The averaging scheme was performed and compared with one day, month (30 day), or season (90 day) as the bin size. The one day averages contain much of the stochastic characteristics of the wind, which for the sake of this review is undesirable, making the prediction of overall yearly trends difficult. Monthly and seasonal averages reduce the high variability of the wind to reveal a clear trend for yearly averages of wind speed. The monthly averaging was selected over seasonal averaging due to the presence of some of the higher frequency trends that the seasonal averaging smoothed out. For the remainder of this review, 30 day averages will be used in the plots and tables where applicable. The plots and tables describe the wind data set at 50m if not stated otherwise.

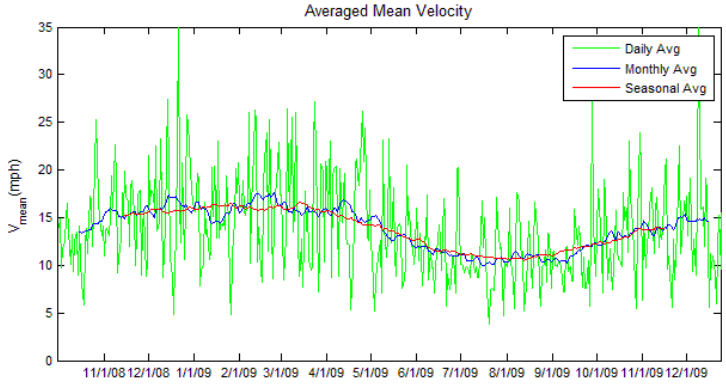

In addition to periodic variation throughout the year there is also a daily variation component superimposed on this predominant trend. The averaging scheme was carried out to also divide the sample bins throughout the day, ranging from 1 to 24 hour selected intervals. The hourly variation is illustrated below with the thick black line displaying the mean velocity when no daily sampling was performed (24 hour bin).

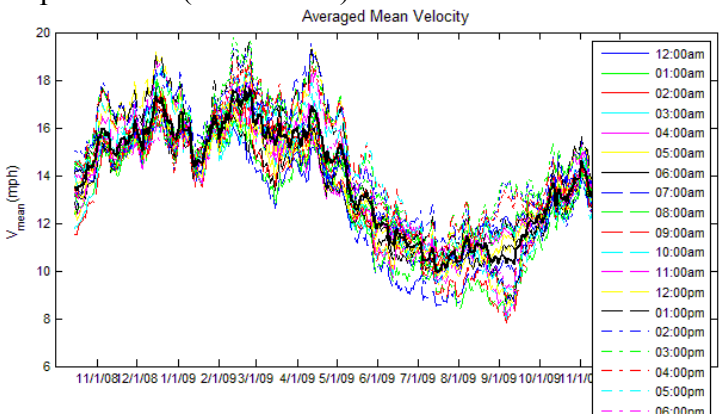

This analysis reveals significant variations in the average wind speed both throughout the year and throughout the day. Daily variations fluctuate throughout the year and range from about 1.5 to 5 mph differences in the average wind speed, with the underlying yearly average varying 7 mph throughout the year. The table below adds insight into the physical properties of the monthly and daily variation. The data representing the month is from the 30 day average whose center is located on the 15th day of that month. The average velocity for that month is given (as displayed by the thick black line in the figure above), and minimum and maximum values for that average were found for each month from the hourly sampled data. The times where the wind is at a minimum and maximum are also given for each month. All of these values were averaged together to yield yearly averaged values. The minimum wind velocity in the day for this area typically occurs early in the morning averaged to 7 a.m. (with the exception of November) and the maximum occurs in the second half of the day averaged to after 4 p.m.

Monthly Averaged Wind Speed Data, 50m (mph)

Month	V,max	t,max	V,min	t,min	V,avg	ΔV,avg
January	15.41	14:00	13.78	0:00	14.46	1.63
February	18.98	22:00	15.64	7:00	17.21	3.33
March	17.00	16:00	12.62	7:00	15.29	4.38
April	19.19	12:00	14.96	1:00	16.67	4.23
May	13.97	17:00	11.39	7:00	12.63	2.58
June	13.42	16:00	9.58	7:00	11.76	3.84
July	11.39	14:00	8.51	7:00	10.00	2.88
August	11.87	14:00	9.65	8:00	11.17	2.22
September	13.36	22:00	9.22	9:00	11.00	4.14
October	14.78	15:00	12.34	8:00	13.23	2.44
November	14.42	22:00	12.78	16:00	13.58	1.64
December	15.86	13:00	13.45	9:00	14.67	2.42
AVERAGE:	14.97	16:25	11.99	7:10	13.47	2.98

The figure below illustrates this trend visually where eight 3-hour samples were taken of the data in order to more easily view the trends. It is observed how the maximum wind speeds throughout the year typically come from the second half of the day, and the minimum wind speeds from the first. The thick black curve of the averaged wind speed with no daily sampling division was also plotted here for comparison.

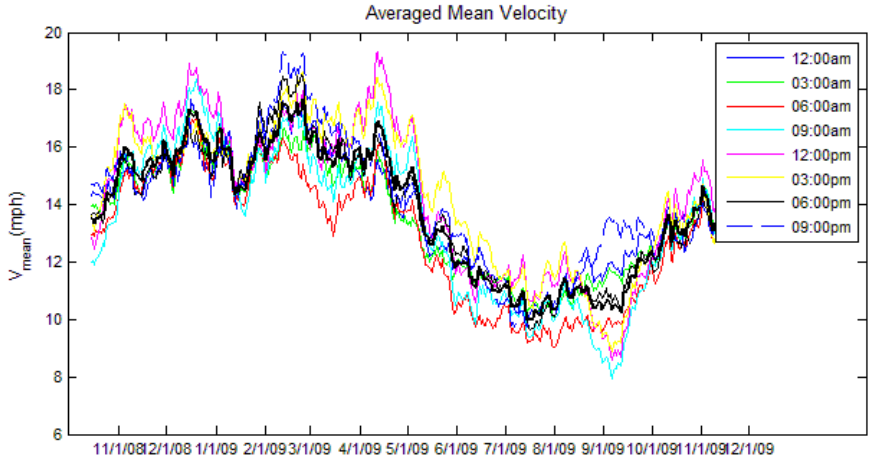

The variability throughout the day differs with the height in the atmosphere as well as seasonally. The monthly summary tables for the four heights not shown above can be found in the Appendix. The daily fluctuations, defined as the difference in the minimum and maximum averaged wind velocity from hourly sampling, are plotted for the five anemometer locations. A trend is observed that these daily fluctuations are stronger closer to the ground.

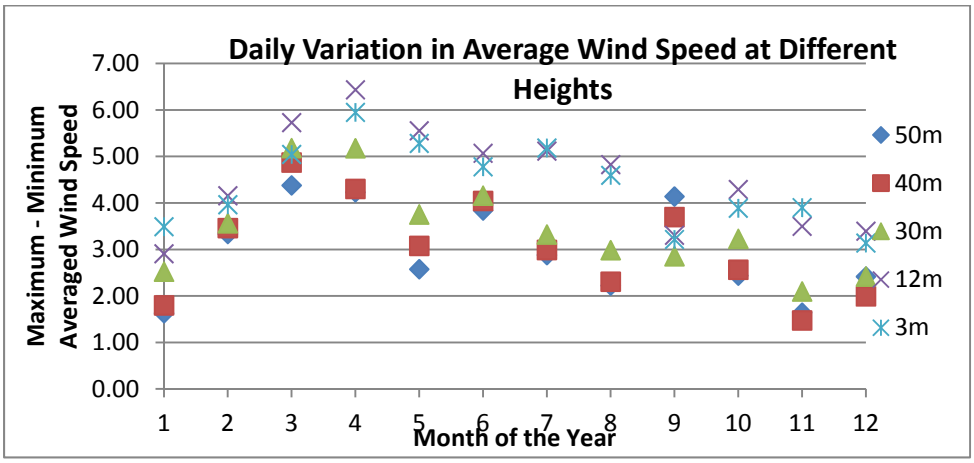

The Weibull probability distribution was applied to the sampled data to prove its reliability in accurately describing the wind speeds in this location. The two parameters to this function were determined, with the shape factor being of particular interest. The shape factor hourly averages were seen to vary from 1.48 to 5.77 throughout the year of interest with significant variation between the months of June and October. This parameter remains within the typical range for wind averaging of 1.5 to 3.0 [1] when not sampling within the day, varying from 1.77 to 3.05 throughout the year.

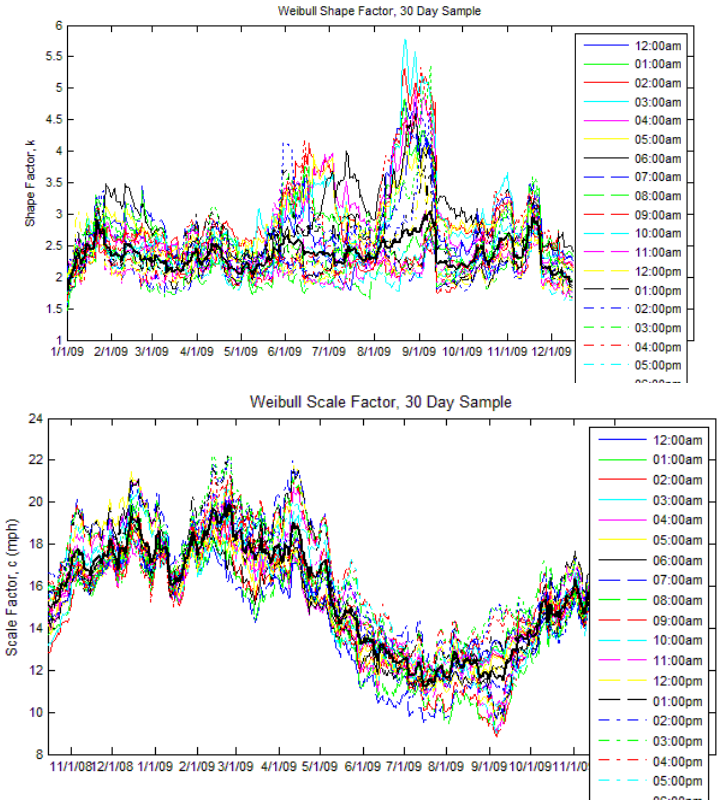

The shape factor determined for each month is summarized below, including the maximum and minimum average values found with 1-hour samples and the time of day where they occur. The shape factor is also given for reference. The monthly shape factors average to 2.49 on the year and vary only by about 0.5 from this mean throughout the year. Unlike with the average wind speed, the shape factor doesn't seem to have any noticeable trends throughout the day for when it is highest and lowest. The corresponding tables at each of the anemometer locations are given in the Appendix for further comparison.

Monthly Weibull Averaged Wind Speed Data, 50m

Month	k,max	t,max	k,min	t,min	k,avg	Δk,avg	c,avg (mph)
January	3.01	19:00	2.25	9:00	2.56	0.76	16.14
February	3.26	6:00	2.13	18:00	2.56	1.13	19.33
March	2.58	2:00	1.72	15:00	2.18	0.86	17.25
April	3.00	22:00	2.20	1:00	2.60	0.80	18.72
May	2.87	3:00	1.84	8:00	2.25	1.03	14.22
June	3.99	23:00	1.81	8:00	2.70	2.18	13.19
July	3.58	6:00	1.81	0:00	2.53	1.77	11.23
August	4.19	2:00	1.91	10:00	2.94	2.27	12.49
September	3.29	6:00	1.79	9:00	2.39	1.50	12.36
October	3.08	3:00	2.01	12:00	2.51	1.07	14.86
November	3.32	23:00	2.16	16:00	2.70	1.16	15.14
December	2.47	6:00	1.63	17:00	1.98	0.84	16.47
AVERAGE:	3.22	10:05	1.94	10:15	2.49	1.28	15.12

The Weibull parameters were used to predict an average wind speed, which is a measure for the distribution's ability to accurately describe the wind data. The figure very nearly resembles that corresponding to the actual data. The error of this estimate compared to the direct average of the wind speed was calculated and is listed for the monthly analysis below. This error is less than 0.85% in each of these months at each anemometer location, with average errors for each location under 0.3%.

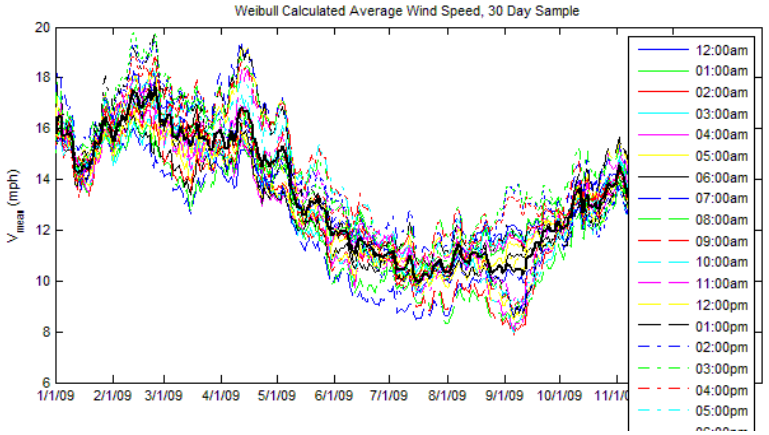

Error (%) in Weibull Average Velocity

Month	50	40	30	12	3
January	0.85	0.10	0.21	0.64	0.02
February	0.22	0.13	0.10	0.13	0.01
March	0.04	0.18	0.15	0.06	0.15
April	0.20	0.00	0.00	0.18	0.02
May	0.21	0.00	0.07	0.15	0.11
June	0.02	0.05	0.05	0.15	0.06
July	0.13	0.05	0.13	0.07	0.28
August	0.05	0.02	0.18	0.03	0.22
September	0.17	0.01	0.07	0.54	0.66
October	0.31	0.03	0.21	0.15	0.06
November	0.78	0.28	0.37	0.37	0.03
December	0.24	0.15	0.10	0.08	0.18
Max Error	0.85	0.28	0.37	0.64	0.66
Avg Error	0.27	0.08	0.14	0.21	0.15

The ability of a distribution to predict the average velocity of the wind is a useful tool for areas where these parameters are known or can be estimated. The prediction of the wind's power density is a more significant value for wind turbines. Power density describes the maximum power contained in the wind and is used to define the wind class environment. The distribution's prediction of velocity has an inherent error which is then multiplied when describing the power density; which is proportional to velocity cubed ($\sim V^3$). The comparison was made between the power density calculated directly from the wind data and that estimated with the three sampling periods chosen: 1, 30, and 90 day. The error in estimating the wind power density remained below a maximum error of about 4% using the Weibull distribution, confirming its acceptable description of this wind data.

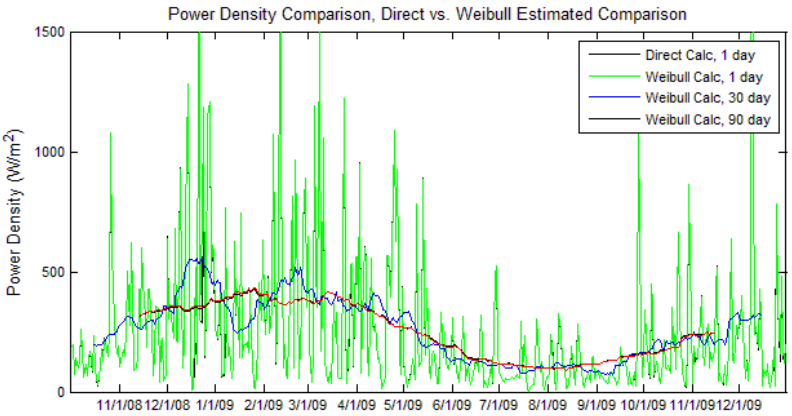

Weibull Averaged Power Density (W/m²)

	50m	40m	30m	12m	3m
ACTUAL	253.0	226.1	187.0	103.0	58.0
1 day	259.2	229.4	189.9	107.2	60.2
%error	2.45%	1.50%	1.57%	4.01%	3.81%
30 day	255.0	226.4	187.6	107.0	59.9
%error	0.79%	0.14%	0.33%	3.86%	3.33%
90 day	252.7	223.8	185.0	105.4	59.4
%error	0.14%	1.01%	1.10%	2.29%	2.49%

The Weibull parameters were used to determine the most probable wind speed and the wind speed carrying the most energy. These figures are added for reference, where a notable comparison should be made between these values and those of the wind turbine power curve. The more significant velocity regarding wind turbines is that at highest energy output (the highest frequency of the cube of the velocity). For the area studied, the most probable wind speed varied seasonally with the yearly average listed for each anemometer height in the figure legend. This yearly average of the most probably wind speed ranged from 5.3 to 12.2mph. The maximum energy wind speed was over twice the most probable wind speed for the 3m and 12m cases, and its yearly average ranged from 13.1 to 20.3mph. The effect of height on the values is notable with the 3m and 12m locations, but far less significant between 30 and 50m. The implications of this result affect the tower height selection for a wind turbine and help to understand the trade-off between power production and the installation height.

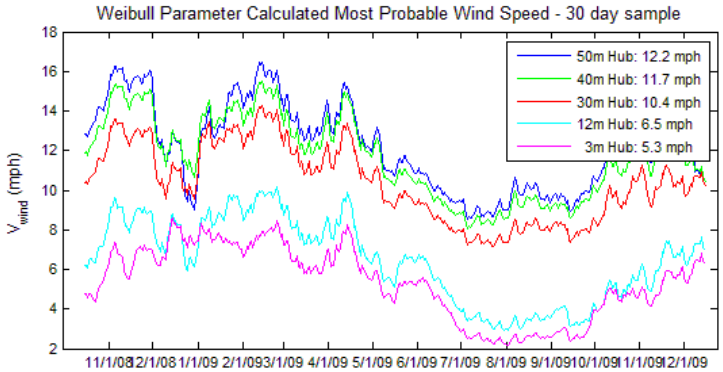

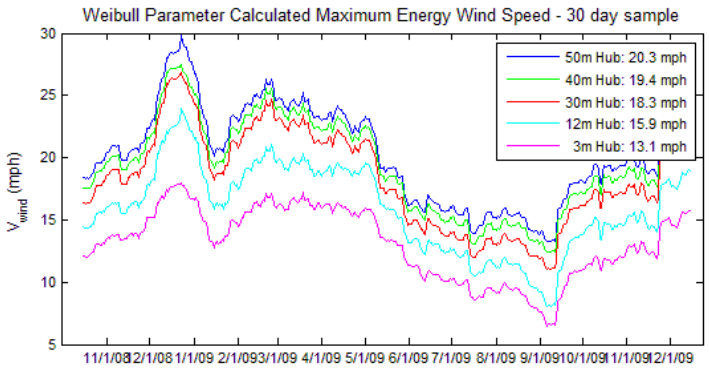

The relationship between the performance of a wind turbine and its hub height is regulated by the atmospheric velocity profile. For this analysis a power law profile was assumed and the velocity profile power coefficient was derived following the procedure previously detailed. This coefficient is illustrated with hourly samples to reveal the nature of the velocity profile throughout the year and day. In this analysis a lower coefficient describes a fuller velocity profile and is associated with turbulence, and a higher coefficient corresponds to a more gradual profile as present with laminar flow conditions. The power coefficient typically lies in the range from 0.05 – 0.5, with 0.14 being a commonly accepted value which is widely applicable to open sites with low surfaces [1].

The plot reveals the dichotomy of this wind variable where there is an upper and lower cluster of hourly averages with minimal transient time between them, around 2 hours. The year of study displays a transition from the high to low cluster at around 6 – 10 am throughout the year, and transitioning up to the high cluster between 4 – 6 pm. These results correlate well with what was found for the average wind speed daily trends which had a minimum occur at 7:10am and maximum at 4:25pm. This correlation means that the velocity profile coefficient is in the low cluster at the minimum wind speeds in the first half day (turbulent conditions) and in the high cluster at the maximum wind speeds in the second half of the day (laminar conditions).

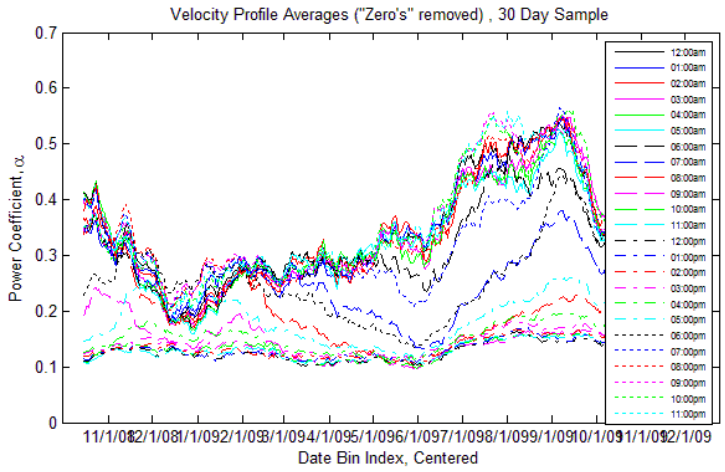

Average monthly wind data was used to show the effect of the velocity profile and how it changes throughout the year. Here the higher wind speed months subscribe to a more turbulent looking profile and lower wind speed months to more laminar looking profiles. The power coefficients were calculated based on these average wind speeds and are listed in the table below.

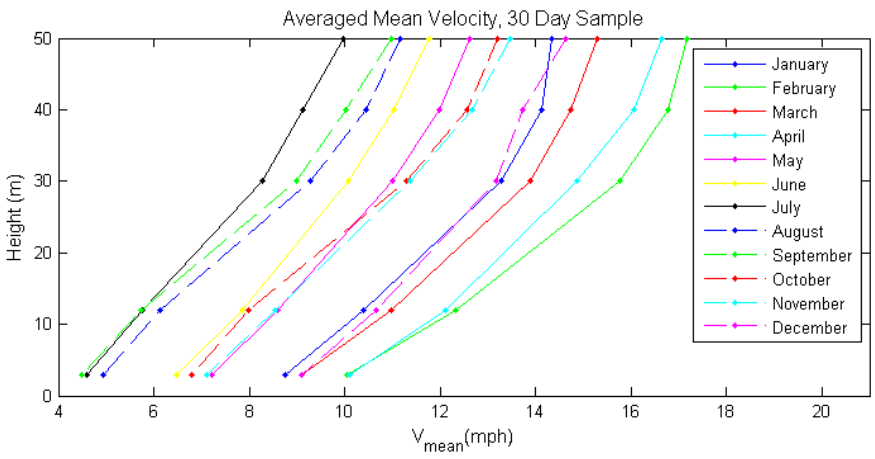

Month	α	Month	α
January	0.19	July	0.28
February	0.2	August	0.3
March	0.19	September	0.33
April	0.18	October	0.25
May	0.2	November	0.23
June	0.21	December	0.17

Purdue Reconfigurable Micro Wind Farm

The Purdue University Micro Reconfigurable Wind Farm consists of four wind turbines mounted on movable carts located in a field north of Zucrow Laboratories. Southwest Windpower Whisper 100 model wind turbines are used in this facility which have a 900W rated power and a 7-ft diameter. The turbines have a hub height of approximately 35-ft above the ground level. Two of the four turbines are instrumented and data collected on the cart. Produced power is used to power the instrumentation with additional power sent to a dump load resistor bank.

Wind farm wind speed is measured with an anemometer mounted at the same height as the turbines 200-ft east of the instrumented turbines. The anemometer is a Lufft two-dimensional sonic anemometer capable of measuring the wind speed in the two horizontal directions at 60 hz. The anemometer will record wind speed and direction during testing. This anemometer is shown in the Figure below.

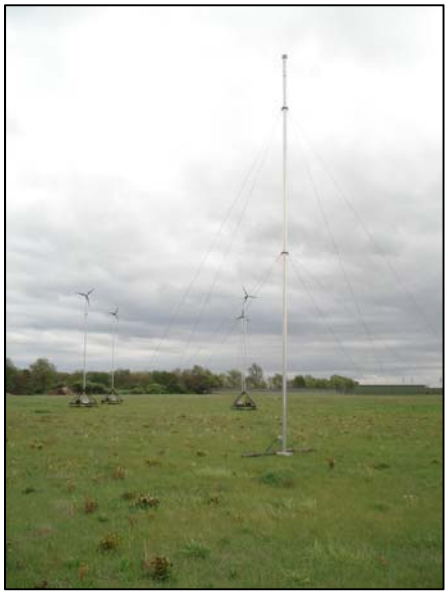

Wind Turbine Performance Instrumentation

Two instrumented wind turbines will be used to measure the performance and load effects on operating in wakes of upstream turbines. Their measurement capabilities are:

Fully Instrumented Turbine

- Rotor aerodynamic torque
- Rotor rotational speed
- (3) DC tri-axial accelerometers on each blade
- DC tri-axial accelerometer mounted in nacelle near bearing set
- Electrical current sent to the battery from the turbine charge controller
- Battery voltage/charging voltage

Secondary Instrumented Turbine

- Rotor aerodynamic torque
- Rotor rotational speed
- Electrical current sent to the battery from the turbine charge controller
- Battery voltage/charging voltage

Wind turbine performance estimation in wake operation

The wake behind a propeller can be calculated analytically with some simplifying assumptions. The first assumption is for one-dimensional, inviscid, steady flow. This assumption treats the wake velocity as a uniform velocity at some deficit value in every region behind the wake. The second major assumption addresses wake expansion and treats this process with a linear approximation. The slope of this approximation is called the wake decay constant, k, and is typically defined to have a value of 0.1.

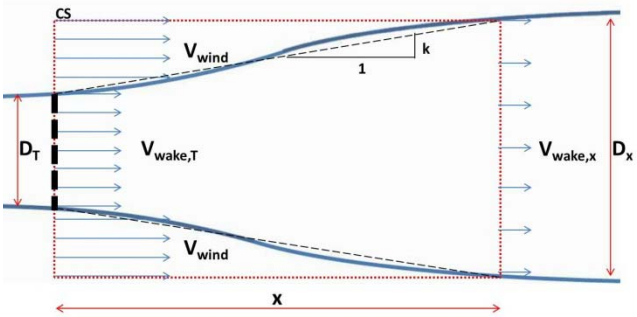

To predict the energy losses arising from operation in the wake of upstream wind turbines, velocity at the location of the downstream profile must be known. The linear wake model can be used to predict that velocity loss, thereby describing the energy loss. Conservation of mass is first used to relate the unknown variables to the known variables. This equation is then reduced by the assumptions as follows:

$$\sum \rho_i V_i A - \rho_e V_e A = 0$$

$$1 - \frac{V_{wake,x}}{V_{wind}} = \left(\frac{D_T}{D_x}\right)^2 \left(\frac{V_{wake,T}}{V_{wind}} - 1\right)$$

The actuator disk analysis described above gives a relation for the velocity just downstream of the rotor plane to the incoming freestream velocity. This relation is put in terms of the thrust coefficient, and is written below using consistent nomenclature:

$$\frac{V_{wake,T}}{V_{wind}} = \sqrt{1 - C_T}$$

Inserting this relation into the equation above yields the wake velocity deficit:

$$1 - \frac{V_{wake,x}}{V_{wind}} = \frac{-1 + \sqrt{1 - C_T}}{\left(1 + 2k\,{}^{x}/_{D}\right)^2}$$

In this equation, maximum velocity losses are associated with a thrust coefficient of 1. As stated above, the thrust coefficient relates to the axial velocity drop from freestream to the rotor plane. A thrust coefficient of one corresponds to complete energy extraction of the incoming freestream, which is never realized. In this analysis, the maximum C_T used was achieved at an axial induction factor of 1/3. Beyond this value the turbine operates in what's known as the turbulent windmill state, where the axial induction factor increases (axial velocity at the rotor plane decreases) but does so with negative results on the power coefficient. This is a very uncommon domain to operate within for a wind turbine, and won't be of interest to this research so it is not considered. The maximum velocity deficit has a direct relationship to the thrust coefficient, which has a direct relationship to the axial induction factor as shown:

$$1 - a = \frac{V_{wake,T}}{V_{wind}} = \sqrt{1 - C_T}$$

Solving this relation using the optimum axial induction factor corresponding to maximum power coefficient, a=1/3, yields a maximum thrust coefficient of $C_{T,max}$=0.55. The thrust coefficient's relationship with wind speed was given generically by Frandsen, and is thought to fit for most modern wind turbines. This relationship is stated below as used in the calculation of the wake velocity deficit to illustrate the dependence on the incoming wind speed. This relationship was used only when the thrust coefficient produced remained below 0.55.

$$C_T = \frac{3.5(2V_{hub} - 3.5)}{V_{hub}^2}$$

The velocity loss as a result of this wake was derived and is illustrated below, with the maximum estimated power loss shown.

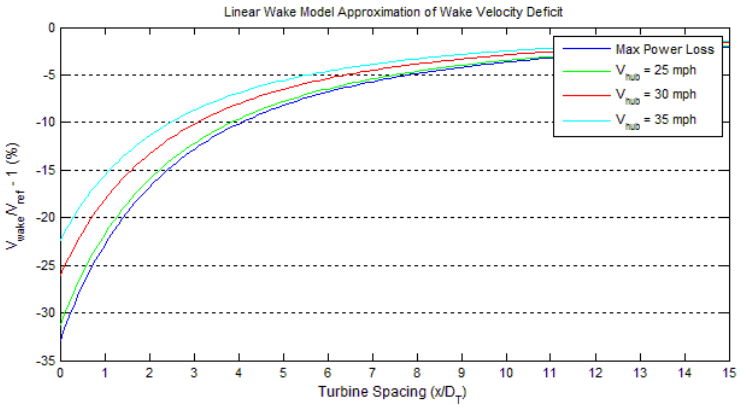

The calculated velocity deficit can be used to determine the power deficit when the turbine power's relationship to the wind speed is known. The generic wind turbine power curve is described below, where V_C, V_R, V_F, and P_R all describe the wind turbine performance and are the cut-in speed, rated-speed, cut-out speed, and rated power. The exponent n describes the power relationship and typically has a value between 2 and 3.

$$P_T(V_W) = \begin{cases} 0 & V_W < V_C \\ P_R\left(\dfrac{{V_W}^n - {V_C}^n}{{V_R}^n - {V_C}^n}\right) & V_C \le V_W \le V_R \\ P_R & V_R < V_W \le V_F \\ 0 & V_W > V_F \end{cases}$$

Using this relationship for the operation range ($V_C \le V_W \le V_R$) of the turbine, a relationship is derived between the velocity deficit and the power deficit as follows:

$$\frac{P_{wake}}{P_{ref}} = \left(\frac{V_{wake}}{V_{ref}}\right)^n$$

For this analysis the exponent, n, is needed and is found for the Southwest Windpower Whisper 100 turbine which will be the experimental subject of the wake performance loss analysis. From the figure below, it is seen that this turbine's power curve more closely follows the n=2 relationship.

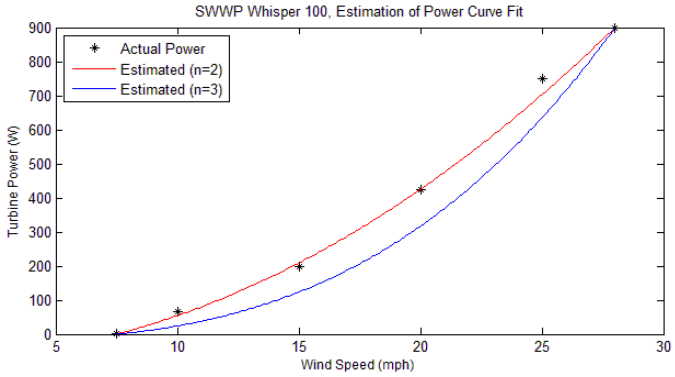

Using this value for n and the relationship from the equation above, the power deficit was determined when operating in a wake from another wind turbine spaced x/D upstream, as illustrated below.

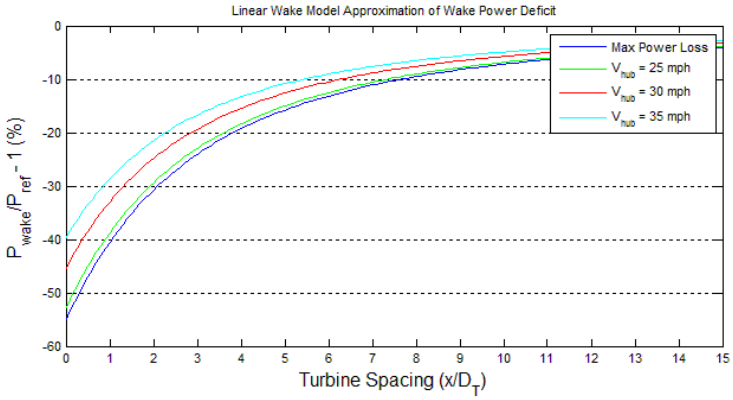

Wind Farm Simulation

Wind turbine wakes are volumes of reduced wind speed and increased turbulence generated downwind of the wind turbines. Power losses due to these wakes are on the order of 10 to 20% of the total power output in large wind farms. In order to understand the flow phenomena and to optimize wind farms, there have been many numerical and experimental simulations of wind farm aerodynamics. While wind farm models adequately predict power losses due to wakes in small wind farms, wakes losses in large wind farms are larger than predicted and wake losses in complex terrain have yet to be fully evaluated, with preliminary evaluations of CFD models suggesting overprediction. The issue is to quantify losses correctly and to understand the discrepancy between how wakes behave in small and large wind farms. There is a gap between engineering solutions and computational fluid dynamics (CFD) models and a bridge is needed between these to provide more detailed information for modeling power losses, for better wind farm and turbine design and for more sophisticated control strategies and load calculations.

The size and evolution of wake structures depends on many factors such as the ambient wind speed and turbulence, wake added turbulence, the turbine characteristics, the terrain and the structure of the boundary-layer relating to atmospheric stratification. Development of a wind farm model requires detailed understanding of the flow and the interaction of complex atmospheric structures with those generated by the wind turbines. The need for reliable wake modeling has been recognized for many years and various models have been developed to simulate turbine wakes. However, the interactions between wind turbines and the atmospheric turbulent boundary layer are not well understood.

The interaction between wind-turbine wakes and atmospheric boundary-layer (ABL) turbulence, and its effects on energy production as well as dynamic loading on downwind turbines, have become important issues in both the wind energy and the atmospheric science communities. Understanding this interaction requires detailed knowledge of wind-turbine wakes and atmospheric turbulence over a wide range of spatial and temporal scales. Accurate prediction of the ABL flow and its interaction with wind turbines as well as turbine-induced wakes is of great importance in optimizing the performance of wind turbines and wind farms. It can be used to maximize the wind energy production and minimize the fatigue loading in the evaluation of wind farm layouts. In addition, numerical simulations can provide valuable quantitative insight into the potential impacts of wind farms on local meteorology.

CFD will be increasingly important in wind turbine wake studies in which the interaction of turbines in wind farms needs to be determined. Numerous complexities exist, including high rotor loading, yawed conditions, complex terrains, with the atomophere also required to be modeled. There are still open issues that need to be addressed in order to guarantee the accuracy of numerical simulations of high-Reynolds number boundary-layer turbulent flow in the ABL and in the turbine-induced wakes. A recent wind-tunnel study (Medici and Alfredsson 2006) has shown that the structure of the wake of a model turbine located in the free-stream flow is substantially changed by the presence of turbulence. More recently, Chamorro and Porté-Agel (2009) carried out a wind-tunnel experiment to study the wake of a miniature wind turbine placed in a boundary layer developed over different surface roughness conditions. They showed that the incoming boundary-layer flow characteristics which are affected by the surface roughness, have a strong effect on the turbine wake dynamics. Considering that wind turbines are always exposed to turbulent boundary-layer flow conditions, it is of interest to test the performance of numerical simulation techniques under such conditions.

Due to the high Reynolds number of the ABL flow, direct numerical simulation (DNS) is impossible, and numerical models require two parameterizations: a turbulence model and a model for the turbine-induced forces. Previous studies of ABL flows through isolated wind turbines or wind farms have modelled the turbulence using a Reynolds-averaged Navier–Stokes (RANS) approach (Ammara et al. 2002; Alinot and Masson 2002; Gómez- Elvira et al. 2005; Kasmi and Masson 2008) or a large-eddy simulation (LES) technique (Jimenez et al. 2007, 2008). In RANS, turbulent fluxes and energy are fully parametrized and, thus, the approach is incapable of predicting turbulent eddy motions. In contrast, LES explicitly resolves all scales of turbulent transport larger than the grid scale, while the smallest scales are parametrized using a subgrid-scale (SGS) model. Due to a large fraction of the turbulence being resolved, LES has become a popular tool for the study of turbulent transport in the ABL flows (e.g., Moeng 1984; Albertson and Parlange 1999; Porté-Agel et al. 2000; Chamecki et al. 2009). However the application of LES for wind turbine wake studies is limited and most of the numerical simulation do not consider the effects of thermal stability and incoming boundary-layer flow characteristics on the wind-turbine wakes.

Generalized actuator disc and related methods, which combine full set Navier Stokes equations with a blade element approach and two-dimensional airfoil data, is a promising technique for studying the dynamics in the wake since the influence of the blades on the flow field is modeled with a limited number of mesh points. This technique has been used for both stand alone turbines and rows of wind turbines. Computations have mostly been carried out assuming steady state or uniform inflow but a few studies have been conducted in simulated atmospheric boundary layers.

Objectives

The objectives of this research are to develop a high order finite volume CFD solver, combine the generalized actuator disc and actuator line methods, provide detailed knowledge of wind-turbine wakes and atmospheric turbulence over a wide range of spatial and temporal scales, provide accurate prediction of the ABL flow and its interaction with wind turbines as well as turbine-induced wakes, gain more insight into the phenomenon of wake interaction and how it affects the external aerodynamic loads on wind turbines in order to maximize wind energy production and minimize fatigue loading in the evaluation of wind farm layouts, and to provide valuable quantitative insight into the potential impacts of wind farms on local meteorology.

Specific research objectives include the following:

- Develop a high order 3D Finite Volume turbulent models, Large Eddy Simulation (LES), for turbine wakes.
- Generate the consistent turblent inflow boundary condition within the atmospheric boundary layer, under both neutral and stably stratified conditions.
- Study the effects of thermal stability and incoming boundary-layer flow characteristics on wind-turbine wakes, with a row of turbines in the streamwise direction considered.
- Investige the charateristics of wind turbine wakes in the wind farm environment
    - Develop a wind turbine wake simulation with an Actuator Disk Model.
    - Develop a wind turbine wake simulation with an Actuator Line Model.

Mathematical Formulation

Navier-Stokes Equations

In this research, the unsteady, three-dimensional, Navier-Stokes equations are numerically integrated. In order to deal with complex geometries, a general curvilinear coordinate system (ξ_1, η, ζ) is adopted.

Filtered Navier-Stokes Equations

Large Eddy Simulation (LES) can be thought of as a compromise between Direct Numerical Simulation (DNS) and the Renolds Averaged Navier-Stokes (RANS) equations. In a DNS, all the relevant scales of turbulence have to be calculated directly whereas in a RANS calculation, all the relevant scales of turbulence need to be modelled. Large eddy simulation (LES) is essentially a simulation that directly solves the large scale motion but approximates the small scale motion using a subgrid-scale (SGS) model, that is, in LES, the flowfield is decomposed into a large-scale or resolved-scale component and a small-scale or subgrid-scale component.

$$\phi = \overline{\phi} + \phi_{sg}$$

The large-scale components are obtained by filtering the entire domain using a grid filter function, G. A filtered variable denoted by an overbar is defined by

$$\overline{\phi} = \int_D \phi(\mathbf{x}') G(\mathbf{x}, \mathbf{x}') d\mathbf{x}'$$

where, D is the fluid domain, and G is the filter function that determines the scale of the resolved eddies.

The filtering operation removes the small-scale or the subgrid-scale turbulence from the Navier-Stokes equations. The resulting equations are then solved directly for the large-scale turbulent motions while the subgrid-scales are computed using a subgrid-scale model such as the Smagorinsky model.

The finite volume discretization itself implicitly provides the filtering operation:

$$\overline{\phi} = \frac{1}{V_{cell}} \int_{V_{cell}} \phi(\mathbf{x}') d\mathbf{x}', \mathbf{x}' \in V_{cell}$$

where V_{cell} is the volume of a computational cell, and the filter function, $G(\mathbf{x}, \mathbf{x}')$ is

$$G(\mathbf{x}, \mathbf{x}') = \begin{cases} 1/V_{cell}, & \mathbf{x}' \in V_{cell} \\ 0, & \mathbf{x}' \text{ otherwise} \end{cases} \tag{1.1}$$

The filtered Navier-Stokes equations take the form:

$$\frac{\partial \overline{\rho}}{\partial t} + \frac{\partial}{\partial x_j}\left(\overline{\rho}\tilde{u}_j\right) = 0 \tag{1.2}$$

$$\frac{\partial}{\partial t}\left(\overline{\rho}\tilde{u}_i\right) + \frac{\partial}{\partial x_j}\left(\overline{\rho}\tilde{u}_j\tilde{u}_i\right) = -\frac{\partial \overline{p}}{\partial x_i} + \frac{\partial \tilde{\sigma}_{ij}}{\partial x_j} - \frac{\partial \tau_{ij}}{\partial x_j} + \frac{\partial}{\partial x_j}\left(\overline{\sigma}_{ij} - \tilde{\sigma}_{ij}\right) + \overline{f}_i \tag{1.3}$$

$$c_v \frac{\partial}{\partial t}\left(\bar{\rho}\tilde{T}\right) + c_v \frac{\partial}{\partial x_j}\left(\bar{\rho}\tilde{u}_j\tilde{T}\right) + \bar{p}\frac{\partial \tilde{u}_j}{\partial x_j} - \tilde{\sigma}_{jk}\frac{\partial \tilde{u}_k}{\partial x_j} + \frac{\partial \tilde{Q}_j}{\partial x_j} + c_v \frac{\partial q_j}{\partial x_j}$$
$$= -\left(\overline{p\frac{\partial u_j}{\partial x_j}} - \bar{p}\frac{\partial \tilde{u}_j}{\partial x_j}\right) + \left(\overline{\sigma_{jk}\frac{\partial u_k}{\partial x_j}} - \bar{\sigma}_{jk}\frac{\partial \tilde{u}_k}{\partial x_j}\right) - \frac{\partial}{\partial x_j}\left(\bar{Q}_j - \tilde{Q}_j\right) \tag{1.4}$$

where the viscous stress tensor due to molecular viscosity is defined by

$$\tilde{\sigma}_{ij} = \tilde{\mu}\left(\frac{\partial \tilde{u}_i}{\partial x_j} + \frac{\partial \tilde{u}_j}{\partial x_i} - \frac{2}{3}\mu\frac{\partial \tilde{u}_k}{\partial x_k}\delta_{ij}\right) \quad \tilde{Q}_j = -\tilde{k}\frac{\partial \tilde{T}}{\partial x_j} \tag{1.5}$$

and the subgrid scale (SGS) stress tensor and heat flux vector are

$$\tau_{ij} \equiv \bar{\rho}\widetilde{u_i u_j} - \rho\tilde{u}_i\tilde{u}_j \qquad q_j \equiv \bar{\rho}\left(\overline{u_j T} - \bar{u}_j T\right)$$

To close the set of equations, the SGS stress terms have to be modeled.

Subgrid-Scale Models

The subgrid-scale stresses resulting from the filtering operation are unknown, and require modeling. By employing the Boussinesq hypothesis as in the RANS models, the SGS turbulent stresses are computed from

$$\tau_{ij} = \underbrace{\tau_{ij} - \frac{1}{3}\tau_{kk}\delta_{ij}}_{\text{deviatoric}} + \underbrace{\frac{1}{3}\tau_{kk}\delta_{ij}}_{\text{isotropic}} \qquad \tau_{ij} - \frac{1}{3}\tau_{kk}\delta_{ij} = -\mu_t \bar{S}_{ij} \tag{1.6}$$

where μ_t is the subgrid-scale turbulent viscosity, the isotropic part of the subgrid-scale stresses τ_{kk} is not modeled for incompressible flow but added to the filtered static pressure term, or simply neglected, and $\bar{S}_{ij}$ is the rate-of-strain tensor for the resolved scale defined by

$$\bar{S}_{ij} \equiv \frac{1}{2}\left(\frac{\partial \bar{u}_i}{\partial x_j} + \frac{\partial \bar{u}_j}{\partial x_i}\right) \tag{1.7}$$

Smagorinsky-Lilly Model

The eddy-viscosity is modeled by

$$\mu_t = \rho L_s^2 \left|\bar{S}\right|$$

where L_s is the mixing length for subgrid scales, $\left|\bar{S}\right| \equiv \sqrt{2\bar{S}_{ij}\bar{S}_{ij}}$, and L_s is computed in Fluent using

$$L_s = \min\left(\kappa d, C_s \Delta\right)$$

where, κ is the von $Ka'rma'n$ constant, d is the distance to the closest wall, C_s is the Smagorinsky constant, and Δ is the local grid scale, and Δ is computed in Fluent according to the volume of the computational cell using $\Delta = V^{1/3}$.

The dynamic subgrid-scale kinetic energy model

The subgrid-scale kinetic energy is defined as

$$k_{sgs} = \frac{1}{2}\left(\overline{u_k^2} - \overline{u}_k^2\right)$$

The SGS eddy viscosity, μ_t is computed using k_{sgs} as

$$\mu_t = C_k k_{sgs}^{1/2} \Delta f$$

where Δf is the filter-size computed from $\Delta f \equiv V^{1/3}$.

The SGS stress can then be written as

$$\tau_{ij} - \frac{2}{3} k_{sgs} = -2\mu_t \overline{S}_{ij}$$

k_{sgs} is obtained by solving its transport equation

$$\frac{\partial \overline{k}_{sgs}}{\partial t} + \frac{\partial}{\partial x_j}\left(\overline{u}_j \overline{k}_{sgs}\right) = \tau_{ij}\frac{\partial \overline{u}_i}{\partial x_j} - C_\varepsilon \frac{k_{sgs}^{3/2}}{\partial x_j} - \frac{\partial}{\partial x_j}\left(\frac{\mu_t}{\sigma_k}\frac{\partial k_{sgs}}{\partial x_j}\right) \tag{1.8}$$

Numerical Discritization of the Modeled Governing Equation

Finite Volume Method

The finite volume method transforms partial differential equations into algebraic equations. Finite volume refers to the small volume surrounding each node point on a mesh. In the finite volume method, volume integrals in a partial differential equation that contain a divergence term are converted to surface integrals, using the divergence theorem. These terms are then evaluated as fluxes at the surfaces of each finite volume. Because the flux entering a given volume is identical to that leaving the adjacent volume, these methods are conservative.

The physical domain, surrounding the wind turbine in the wind farm environment, is divided into grid cells with the aid of a blade-fitted three dimensional grid generation procedure. For a deforming or moving control volume, Ω_P, the integral form of the transformed Navier-Stokes equations may be written as,

$$\int_t^{t+\Delta t}\left[\frac{\partial}{\partial t}\iiint_{\Omega_P}\hat{Q}d\Omega + \iiint_{\Omega_P}\left(\frac{\partial \hat{F}}{\partial \xi} + \frac{\partial \hat{G}}{\partial \eta} + \frac{\partial \hat{H}}{\partial \zeta}\right)d\Omega\right]dt = \int_t^{t+\Delta t}\left[\iiint_{\Omega_P}\left(\frac{\partial \hat{F}_v}{\partial \xi} + \frac{\partial \hat{G}_v}{\partial \eta} + \frac{\partial \hat{H}_v}{\partial \zeta}\right)d\Omega\right]dt \tag{1.9}$$

where Ω_P is a deforming control volume, S is the surface of the control volume.

Applying Gauss theorem,

$$\int_t^{t+\Delta t}\left[\frac{\partial}{\partial t}\iiint_{\Omega_P} QdV + \oiint_S\left(E\vec{i} + F\vec{j} + G\vec{k}\right)\bullet\vec{n}dS\right]dt = \int_t^{t+\Delta t}\left[\oiint_S\left(E_v\vec{i} + F_v\vec{j} + G_v\vec{k}\right)\bullet\vec{n}dS\right]dt \tag{1.10}$$

For simplicity, the numerical discretization procedure is presented based on the standard form of the transport equation for a scalar property ϕ. Here, ϕ could be any the contravariant

components of velocity as before, i.e., U , V , W . Assuming that the control volume does not change in time, the semi-discretised form of the transport equation may be written as,

$$\int_t^{t+\Delta t}\left[\frac{\partial \rho\phi}{\partial t}\Omega_P + \iiint_{\Omega_P}\nabla\bullet\left(\rho\vec{V}\phi\right)dV - \iiint_{\Omega_P}\nabla\bullet\left(\rho\Gamma_\phi\nabla\phi\right)dV\right]dt = \int_t^{t+\Delta t}\left(\iiint_{\Omega_P} S_\phi(\phi)dV\right)dt \tag{1.11}$$

Discretization of Spatial Terms

Laplacian term:

$$\iiint_{\Omega_P}\nabla\bullet\left(\Gamma\nabla\phi\right)d\Omega = \sum_f \Gamma_f S_f \bullet\left(\nabla\phi\right)_f \tag{1.12}$$

The 3-D LES solver uses the non-dissipative sixth-order central compact scheme proposed by Lele (Lele) to compute the spatial derivatives. In order to apply this scheme, the curvilinear grid (physical domain) is transformed into a uniform grid, in the computational domain. In the computational domain, the interior grid points are written as follows.

$$\frac{1}{3}f_{i-1}^{'} + f_i^{'} + \frac{1}{3}f_{i+1}^{'} = \frac{7}{9\Delta\xi}\left(f_{i+1} - f_{i-1}\right) + \frac{1}{36\Delta\xi}\left(f_{i+2} - f_{i-2}\right) \tag{1.13}$$

where $f_i^{'}$ is the derivative of f at grid point i along the ξ direction, and $\Delta\xi$ is the uniform grid spacing along the ξ direction. For the first and last grid points, e.g. i = 1 and i = n, the following third-order one-sided compact scheme is applied.

$$f_i^{'} + 2f_2^{'} = \frac{1}{2\Delta\xi}\left(-5f_1 + 4f_2 + f_3\right) \tag{1.14}$$

$$f_n^{'} + 2f_{n-1}^{'} = \frac{1}{2\Delta\xi}\left(5f_n - 4f_{n-1} - f_{n-2}\right) \tag{1.15}$$

For the i = 2 and i = n-1 points, the following fourth order central compact scheme is used.

$$\frac{1}{4}f_1^{'} + f_2^{'} + \frac{1}{4}f_3^{'} = \frac{3}{4\Delta\xi}\left(f_3 - f_1\right) \tag{1.16}$$

$$\frac{1}{4}f_{n-2}^{'} + f_{n-1}^{'} + \frac{1}{4}f_n^{'} = \frac{3}{4\Delta\xi}\left(f_n - f_{n-2}\right) \tag{1.17}$$

The convection term

The convection term is integrated over a control volume and linearized as follows:

$$\iiint_{\Omega_P}\nabla\bullet\left(\rho\vec{V}\phi\right)dV = \oiint_S dS\bullet\left(\rho\vec{V}\phi\right) = \sum_f F\phi_f \tag{1.18}$$

The face field ϕ_f can be evaluated using a variety of schemes.

High order numerical methods have been widely used in CFD, to resolve complex flow features using meshes which are reasonable for today's computers. The weighted essentially non-oscillatory (WENO) finite volume methods, have advantage over other compact schemes because they consider all the three stencils forward, backward and central schemes takes the

weighted average of the values based on these stencils, so has the advantage of obtaining higher order with small stencil and also can capture shocks efficiently.

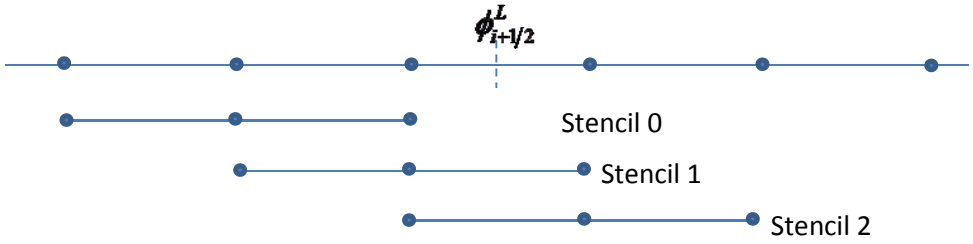

Stencil for the WENO Scheme

For the fifth-order accurate WENO reconstruction of $\phi^L_{i+1/2}$

$$\phi^L_{i+1/2} = \omega_0\phi_0 + \omega_1\phi_1 + \omega_2\phi_2 \tag{1.19}$$

where

$$\begin{cases} \phi_0 = \frac{1}{3}\phi_{i-2} - \frac{7}{6}\phi_{i-1} + \frac{11}{6}\phi_i \\ \phi_1 = -\frac{1}{6}\phi_{i-1} + \frac{5}{6}\phi_i + \frac{1}{3}\phi_{i+1} \\ \phi_2 = \frac{1}{3}\phi_i + \frac{5}{6}\phi_{i+1} - \frac{1}{6}\phi_{i+2} \end{cases} \tag{1.20}$$

and the weights are defined as

$$\omega_s = \frac{\alpha_s}{\sum \alpha_s}, \quad \alpha_s = \frac{C_s}{\varepsilon + \beta_s} \tag{1.21}$$

In the above equation, the smoothness indicators ϕ_s are

$$\begin{cases} \beta_0 = \frac{13}{12}\left(\phi_{i-2} - 2\phi_{i-1} + \phi_i\right)^2 + \frac{1}{4}\left(\phi_{i-2} - 4\phi_{i-1} + 3\phi_i\right)^2 \\ \beta_1 = \frac{13}{12}\left(\phi_{i-1} - 2\phi_i + \phi_{i+1}\right)^2 + \frac{1}{4}\left(\phi_{i-1} - \phi_{i+1}\right)^2 \\ \beta_2 = \frac{13}{12}\left(\phi_i - 2\phi_{i+1} + \phi_{i+1}\right)^2 + \frac{1}{4}\left(3\phi_i - 4\phi_{i+1} + \phi_{i+2}\right)^2 \end{cases} \tag{1.22}$$

and $\phi^R_{i+1/2}$ can be constructed in the way symmetric to $\phi^L_{i+1/2}$.

There are several choices of the variable to be evaluated, for example the primitive variable, conservative variable, or the characteristic variable. Currently in most simulations using the WENO algorithm, either the conservative, or the primitive variables are evaluated.

Time Discretization

The classical four-stage Runge-Kutta explicit scheme is used to advance the solution. This scheme is a predictor-corrector integration scheme initially developed for ordinary differential equations and later extended to the solution of hyperbolic partial differential equations. A distinctive feature of this class of time discretizations is that they are conplex

combinations of first order forward Euler steps and thus maintain stability properties in any semi-norm (total variation norm, maximum norm, entropy condition, etc.) of the forward Euler step. Thus one only needs to prove nonlinear stability for the first order forward Euler step, and one automatically obtains the same stability property for the higher order time discretizations in this class. The most popular scheme is the fourth order Runger-Kutta scheme, which is used here to solve $Q_t = L(Q,t)$, where, $L(u,t)$ is a spatial discretization operator.

The four stage time integration from time step n to n+1 can be written as

$$Q^{n+1} = Q^n + \frac{2}{3}Q^{(2)} + \frac{1}{6}\Delta t\left(k_1 + 2k_2 + 2k_3 + k_4\right) \tag{1.23}$$

where $k_1 = L\left(Q^n, t^n\right) \qquad k_2 = L\left(Q^n + \frac{1}{2}k_1\Delta t, t^n + \frac{\Delta t}{2}\right)$

$k_3 = L\left(Q^n + \frac{1}{2}k_2\Delta t, t^n + \frac{\Delta t}{2}\right) \qquad k_4 = L\left(Q^n + k_3\Delta t, t^n + \Delta t\right)$

The timestep can be calculated from the convective timestep for the Euler equations and a comparison of the convective and diffusive timesteps in the Navier-Sokes equations. The convective timestep is defined from the Courant-Friedrichs-Loewy (CFL) number. The CFL number associated with a particular flow direction, k, is defined at every grid point as

$$CFL_k = \lambda_k \frac{\Delta t}{\Delta k}$$

The CFL number is kept constant to keep every grid point converging at the same rate. This method has been shown to be effective and stable.

The local time-step for the Euler equations is defined as

$$\Delta t = \frac{CFL}{\sqrt{\lambda_{\xi\max}^2 + \lambda_{\eta\max}^2}}\left(\Delta\xi + \Delta\eta\right) \tag{1.24}$$

where $\lambda_{\xi\max}$ and $\lambda_{\eta\max}$ are the maximum eigenvalues in the ξ and η direction respectively.

For the Navier-Stokes equations the above timestep is compared to the diffusive timestep and the minimum value is used as the timestep at every grid point. The diffusive timestep is defined by the von Neumann number σ.

$$\sigma_k = \nu\frac{\Delta t}{\Delta k^2}$$

Solution Procedure for Incompressible Viscous Flow

The incompressible Navier-Stokes equations exhibit a mixed elliptic-parabolic behavior, with the iterative pressure correction technique developed by Patankar and Spalding often used. The technique is embodied in the SIMPLE (Semi-Implicit Method for Pressure-Linked Equations).

For the 2D case on the structured grid, the discretised momentum equation is given by

$$\begin{cases} u_P^{m^*} = \dfrac{Q_u^{m-1} - \sum_l A_l^u u_l^{m^*}}{A_P^u} - \dfrac{1}{A_P^u}\left(p_e S_e - p_w S_w\right)^{m-1} \\ v_P^{m^*} = \dfrac{Q_v^{m-1} - \sum_l A_l^v v_l^{m^*}}{A_P^v} - \dfrac{1}{A_P^v}\left(p_n S_n - p_s S_s\right)^{m-1} \end{cases} \tag{1.25}$$

where $m-1$ is for the last time step, m is stands for the new time step and since the velocities here only satisfy the momentum equation and not the continuity equation. This is emphazed this by using m^* which indicates the intemediate time step.

Define :

$$\begin{cases} u_P^m = u_P^{m^*} + u_P' \\ v_P^m = v_P^{m^*} + v_P \\ p_P^m = p_P^{m^*} + p_P' \end{cases} \tag{1.26}$$

At the new time level m, the velocity field should satisfy the continuity equation. The pressure equation is then

$$\underbrace{\left(\sum_l A_l^p\right)}_{A_P^p} p_P' + \underbrace{\left(-\frac{\rho S_e^2}{A_{P(e)}^u}\right)}_{A_E^p} p_E' + \underbrace{\left(-\frac{\rho S_w^2}{A_{P(w)}^u}\right)}_{A_W^p} p_W' + \underbrace{\left(-\frac{\rho S_n^2}{A_{P(n)}^v}\right)}_{A_N^p} p_N' + \underbrace{\left(-\frac{\rho S_s^2}{A_{P(s)}^v}\right)}_{A_S^p} p_S' = -\Delta\dot{m}_P^* - \underbrace{\Delta\dot{m}_P'}_{omitted} \tag{1.27}$$

where

$$\Delta\dot{m}_P^* = \left[\rho S u^*\right]_e - \left[\rho S u^*\right]_w + \left[\rho S u^*\right]_n - \left[\rho S v^*\right]_s \tag{1.28}$$

The velocity correction equation is:

$$u_e' = \tilde{u}_e' - \frac{S_e}{A_{P(e)}^u}\left(p_E' - p_P'\right) \qquad u_w' = \tilde{u}_w' - \frac{S_w}{A_{P(w)}^u}\left(p_P' - p_W'\right)$$

$$v_n' = \tilde{u}_n' - \frac{S_n}{A_{P(n)}^v}\left(p_N' - p_P'\right) \qquad v_s' = \tilde{v}_s' - \frac{S_s}{A_{P(s)}^v}\left(p_P' - p_S'\right)$$

Wind Turbine Models

Momentum Theory - Actuator Disc Theory

The Actuator Disc model is the oldest analytical tool for evaluating rotor performance. The model is based on conservation of mass, momentum and energy, and is the basis of 1D momentum theory. In the CFD analysis of wind turbine wakes in the wind farm environment, actuator disc theory is used to model the rotor as a continuous disc with a pressure drop, but continuous velocity. Thus individual blades are not modeled; rather, the circular disc of the swept blade area has an imposed boundary condition to model the turbine in the wind simulations.

The rotor is represented by an actuator disc of area A that creates a pressure discontinuity but continuous velocity V. The actuator disc approach uses the following assumptions:

- The flow is ideal and rectilinear across the turbine i.e. steady, homogenous, inviscid, non-rotational, and incompressible. Both the flow and thrust are uniform across the disk.
- Infinite number of blades
- Non rotating wake
- The static pressure at the upwind and downwind boundaries is equal to the ambient static pressure.

Blade Element Momentum - BEM

BEM is applied to the rotor in Two-Dimensional Compared to actuator disk theory, first attributed to Glauert, blade element momentum (BEM) theory determines wing performance as a function of blade length. BEM discretizes the blade radially and determines performance parameters at each discrete section. The net parameters can be taken as a weighted sum of each radial section.

Airfoil data from either experimental or numerical methods correlate the incoming velocity, U_{rel},the angle of attack, α , and the blade geometry to coefficients of lift and drag. These coefficients are used to determine the force vectors for lift and drag. Using angle sum of β and α , these forces are transposed to the force vectors parallel and perpendicular to the plane of rotation known as torque and thrust, respectively. Power is determined by the product of the torque and the rotational speed. An incremental power (P) and power coefficient (C_p) can be determined for each 2-D section of the blade.

BEM implies that the local forces exerted on the blades by the flow are dependent only on local airfoil aerodynamic properties and relative fluid velocity. Decomposing these forces onto the normal and tangential axes, the following expressions are obtained:

$$\begin{cases} f_n = \dfrac{\rho V_{rel} c}{2}\left[U_t C_L + U_n C_D\right] \\ f_t = \dfrac{\rho V_{rel} c}{2}\left[U_n C_L + U_t C_D\right] \end{cases} \tag{1.29}$$

where $V_{rel} = \sqrt{U_{\hat{n}}{}^2 + U_{\hat{t}}{}^2}$ $\quad U_{\hat{n}} = u_i \hat{n}_i$ $\quad U_{\hat{t}} = r\Omega - u_i \hat{t}_i$ $\quad \alpha = \tan^{-1}\left(\dfrac{U_{\hat{n}}}{U_{\hat{t}}}\right) - \beta$

$\hat{n}_i$ corresponds to the unit vector to the actuator disk surface oriented in the same direction as the $\hat{n}$ axis. $\hat{t}_i$ corresponds to the unit vector in the azimuthal direction θ.

The fluid velocity relative to the blade is decomposed into a normal component $U_{\hat{n}}$ and a tangential component $U_{\hat{t}}$ which are functions of the rotational velocity Ω and the fluid velocity u_i. $f_{\hat{n}}$ and $f_{\hat{t}}$ represent the $\hat{n}$ and $\hat{t}$ components of the force exerted by the fluid on the airfoil, per unit length of the blade. C_L and C_D are the lift and drag coefficients and are, in general, functions of angle of attack α , the local Reynolds number Re_c , and relative surface roughness.

Actuator Line Method

Developed by Sørensen and Shen, the flow field around the wind turbine rotor is simulated using the actuator line model. This model combines a three-dimensional Navier-Stokes solver with a technique in which body forces are distributed radially along lines representing the blades of the wind turbine. Thus, the flow field around and downstream the wind turbine is governed by three dimensional Navier-Stokes simulations, while the influence of the rotating blades on the flow field is computed by calculating the local angle of attack and then determining the local forces using tabulated airfoil data.

$$\eta_\varepsilon(d) = \varepsilon^{-2}\pi^{-3/2}\exp\left[-\left(\frac{d}{\varepsilon}\right)^2\right] \tag{1.30}$$

where d is the distance between cell centred grid points and points at the actuator line and ε is a parameter that serves to adjust the concentration of the regularized load.

The main advantage of representing the blades by airfoil data is that much fewer grid points are needed to capture the influence of the blades as compared to what would be needed to simulate the actual geometry of the blades. Therefore, the actuator line model is well suited for wake studies since grid points can be concentrated in a larger part of the wake while keeping the computing costs reasonable. On the other hand, the models reliance on tabulated 2D airfoil data makes it greatly dependent on both their quality as well as the method used for modeling the influence of dynamically changing angles of attack and stall. However, as the main purpose is to study fundamental wake effects it is not required to capture the loads on the rotor exactly.

The applied blade forces need to be distributed smoothly over several mesh points in order to avoid singular behaviour. In practice, the aerodynamic blade forces are distributed along and away from the actuator lines in a three-dimensional Gaussian manner by taking the convolution of the computed local load, f, and a regularization kernel ηε as shown below.

Analytical Wake Models

Werle presented an analytical wake model for application to wind farms. It contains three elements: 1.) an exact model of the essentially inviscid near wake flow region 2.) a methodology for estimating the length of the intermediate wake based on Prandtl's turbulent shear layer mixing solution; and 3.) a far wake model based on the classical Prandtl/Swain axisymmetric wake analysis. The model's predictions reinforce results of recent studies of horizontal axis wind turbine farms indicating that longitudinal turbine spacing of less than 10 rotor diameters leads to severe wake-induced productivity losses.

The near wake is governed by inviscid pressure forces, with the turbulent mixing layer that initiates at the turbine having negligible effect on the flow structure.

$$u_i = 1 + c\left(1 + \frac{2X}{\sqrt{1+4X^2}}\right) \tag{1.31}$$

where u_i is the nondimensional inviscid centerline velocity, c is related to the total circulation induced by the wind turbine, and $X \equiv x/D_p$, c can be determined by matching the predicted outlet velocity at downstream infinity, u_o, to that predicted through use of a momentum balance and actuator disk theory to yield

$$u_i = 1 + \frac{1-u_o}{2}\left(1 + \frac{2X}{\sqrt{1+4X^2}}\right) \tag{1.32}$$

The width, D_i of the capture streamtube can then be calculated from mass conservation,

$$\frac{D_i}{D_p} = \sqrt{\frac{1+u_o}{2u_i}} \tag{1.33}$$

The outlet velocity, u_o, can be determined from the following relations:

Power Coefficient: $$C_P \equiv \frac{P}{\frac{1}{2}\rho A_p V_a^{\,3}} = \frac{u_p A_p (p_u - p_d)}{\frac{1}{2}\rho A_p V_a^{\,3}} = \frac{1}{2}(1+u_o)\left(1-u_o^{\,2}\right) \tag{1.34}$$

Thrust Coefficient: $$C_T \equiv \frac{T}{\frac{1}{2}\rho A_p V_a^{\,2}} = \frac{A_p (p_u - p_d)}{\frac{1}{2}\rho A_p V_a^{\,2}} = \left(1-u_o^{\,2}\right) \tag{1.35}$$

Since the far wakes scales with the Thrust Coefficient, C_T, it is as the controlling parameter for the entire problem. The relation can be inverted to write that:

$$u_o = \sqrt{1-C_T} \qquad C_P = \frac{1}{2}C_T\left(1+\sqrt{1-C_T}\right) \tag{1.36}$$

The centerline velocity and wake growth rate for the complete range of C_T up to the stall limit, $C_T = 1$ are shown below.

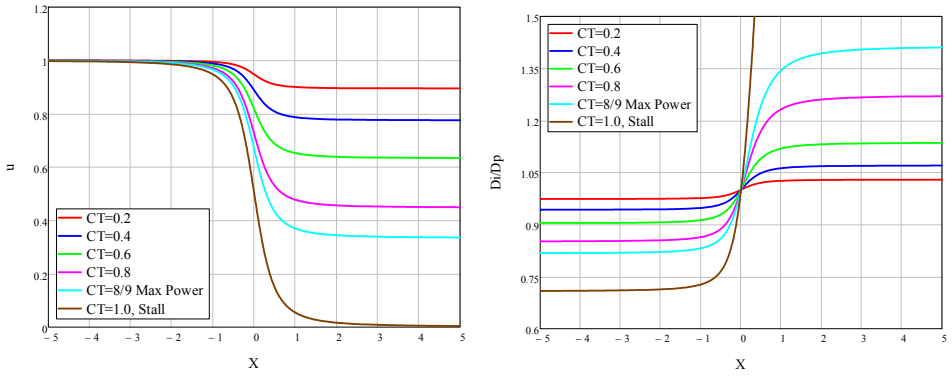

Analytical Wake Model – Inviscid Model

The centerline velocity results can be used to begin to assess the influence of the turbine longitudinal spacing on the power degradation from Turbine 1 to Turbine 2. The power ratio can be written as:

$$\frac{P_2}{P_1} = \left(\frac{V_2}{V_1}\right)\frac{C_{T2}\left(1+\sqrt{1-C_{T2}}\right)}{C_{T1}\left(1+\sqrt{1-C_{T1}}\right)} \tag{1.37}$$

where V_a is the upstream ambient wind speed approaching Turbine 1 and V_2 is the effective wind speed approaching Turbine 2.

$$\frac{V_2}{V_a} = u_{i2} = 1 - \frac{1-u_o}{2}\left[1 + \frac{2(L-1)}{\sqrt{1+4(L-1)^2}}\right] \tag{1.38}$$

The Turbine 1 Thrust Coefficient, C_{T1}, is known, but the corresponding value for Turbine 2, C_{T2} is assumed to be equal to C_{T1}, must be determined from the preformance characteristics of the particular HAWT being employed. The next figure provides the resulting power ratios predicted by the last two equations for the full range of Thrust Coefficients and longitudinal spacing up to L = 5. The levels become extremely low as the Max Power situation is approached and are seen to continue towards zero as the stall level is approached. Clearly these low levels would be unacceptable in any practical sense and indicate why it is necessary to call on the turbulent mixing in the intermediate and far wake regions tohelp increase the centerline velocity and improve the power production situation.

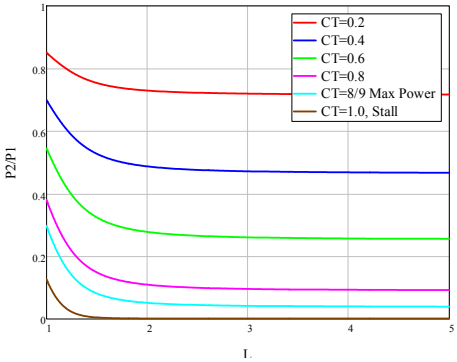

Analytical Wake Model – Inviscid Power Ratios

The Far Wake Region

Using the first order approximation, the viscous wake growth rate, D_V, as given by Swain and the corresponding viscous induced centerline velocity, u_V are

$$\frac{D_V}{D_p} = K(C_T X)^{\frac{1}{3}} \qquad u_V = 1 - \frac{\left(\sqrt{C_T}/X\right)^{\frac{2}{3}}}{2K^2} \tag{1.39}$$

The constant, K, is related to Prandtl's turbulent mixing length and was designated by Swain as a "universal" constant, i.e., one that must be determined from experiments and will be the same for all axisymmetric bodies generating a momentum deficit in a uniform stream, so long as the turbulent mixing length hypothesis is valid. K can be evaluated as:

$$K = \frac{D_V/D_p}{(C_T X)^{1/3}} = \frac{\left(C_T{}^{1/2}/X\right)^{1/3}}{\left[2(1-u_V)\right]^{1/2}} \tag{1.40}$$

Wind turbine experimental data indicate a clear convergence of K to unity from below and above respectively as the scaled axial distances increase. One can write the more general form of the asymptotic far wake model by introducing the virtual origin, X_0, so that

$$u_V = 1 - \frac{1}{2}\left(\frac{\sqrt{C_T}}{X - X_0}\right)^{\frac{2}{3}} \qquad \frac{D_V}{D_p} = \left[C_T(X - X_0)\right]^{\frac{1}{3}} \tag{1.41}$$

The value of X_0, the location of the virtual origin of the wind turbine's far wake region, must be determined through coupling of the far, intermediate and near wake relations.

The Intermediate Region

One can employ Prandtl's solution for turbulent mixing at a planar velocity discontinuity to establish an estimate to the length of the intermediate wake region. This in turn is used to establish X_0 and ultimately couple all three regions. The intermediate wake region begins at a point near X_i, and ends at X_m, when the shear layer penetrates to the centerline. Near X_i, the shear layer thickness is small compared to the radial distance, $R_i = D_i/2 = D_o/2$, and Prandtl's results apply, predicting a linear growth rate for the shear layer width. Using this as a means of estimating X_m, one arrives at the relation:

$$X_m = X_i + K_m \frac{D_o}{D_p} \frac{1+u_o}{1-u_o} \tag{1.42}$$

where the value of K_m has to be established from experimental data. Also, X_i is taken to be 2 and the diameter of the near wake at X_i is given by,

$$\frac{D_i}{D_p} = \sqrt{\frac{1+u_o}{2u_i}} \tag{1.43}$$

The composite wake model

The far wake model is coupled to the near wake by choosing the virtual origin of the far wake, X_0, such that the two velocities, u_i and u_V, are equal at the match point, X_m. The resulting wake centerline velocity relations are:

$$u_w = 1 + \frac{1-u_o}{2}\left(1 + \frac{2X}{\sqrt{1+4X^2}}\right) \quad X < X_m \qquad u_V = 1 - \frac{1-u_m}{\left[\frac{\left(X-X_m\right)\left[2\left(1-u_m\right)\right]^{3/2}}{\sqrt{C_T}} + 1\right]^{2/3}} \quad X > X_m$$

where $u_w = 1 + \frac{1-u_o}{2}\left(1 + \frac{2X}{\sqrt{1+4X^2}}\right)$

Similarly, the resulting wake growth rate relations are:

$$\frac{D_W}{D_p} = \sqrt{\frac{1+u_o}{2u_W}} \quad X < X_m \qquad \frac{D_W}{D_p} = \frac{D_m}{D_p}\left[\frac{C_T\left(X-X_m\right)}{\left(\frac{D_m}{D_p}\right)^3} + 1\right]^{\frac{1}{3}} \quad X > X_m$$

where $\frac{D_m}{D_p} = \sqrt{\frac{1+u_o}{2u_m}}$.

Note that the solution remains dependent on the constant, K_m, which is related inversely to the turbulent mixing length for the intermediate wake region.

As an example calculation, the following figure shows the two components of the centerline velocity solution plus the composite solution for $K_m = 0.1$ at the maximum power case, $C_T = 8/9$. The most significant aspect of the velocity profiles shown is the relatively contorted variation in the velocity as it starts with a low value at the turbine, than decreases further quite rapidly in the near wake after where it reverses itself and begins an initially rapid but ultimately rather surprisingly slow growth toward the free stream value. As also shown, as the constant, K_m, increases (decreasing mixing length), the match point moves downstream as expected. The case of $K_m = 0$ corresponds to an infinitely large mixing length and thus an intermediate wake region length of zero. Similarly, an infinitely large K_m corresponds to a mixing length of zero and would thus produce an infinitely long intermediate wake length.

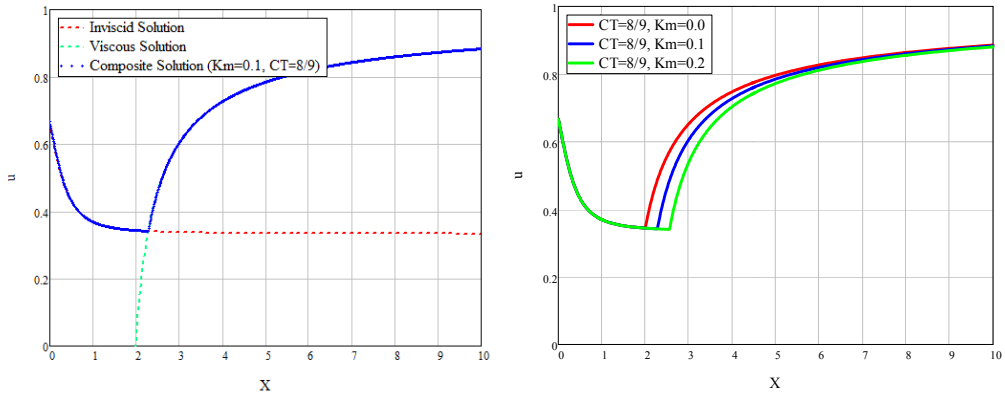

Analytical Wake Model – Model Components at Max Power

The next figure provides a summary of results of the current analysis for a range of thrust coefficient, C_T, from 0.2 to 0.99, the latter being very near stall. Seen in this form, most notable is the very large variation in the wake structure for the typical range over which one expects a HAWT to operate. The flow structure and performance is clearly dominated by the sometimes large velocity trough in the near wake. Even though the velocities asymptotically merge rather quickly in the far wake, they all suffer from an initial deficit and recover very slowly toward the free stream value. One has to be over six diameters downstream to see reasonable velocity recovery which does not begin to attain the 90% level until nine or more diameters distance. The wake growth rates show a much higher sensitivity to the thrust level and are worrisome because of their implications for possible interference with the ground plane for a typical HAWT tower height of 1 to 1.5 turbine diameters. Here, the variation in the intermediate wake is seen to be one of the controlling elements of the far wake growth. These wake growth predictions do not indicate row to row interference for Turbines 2 for up to 10 diameters and well beyond for a typical HAWT lateral spacing of W = 5 or more. Finally, the power degradation ratios, P2/P1 are also very worrisome because of the low values of 0.6 to 0.7 produced for nearly all but the lowest thrust levels, even up to L=10. In should be borne in mind that these predictions can only be viewed as a guide and that the model must be adapted to the particular HAWT performance characteristics, i.e., the dependency of the thrust coefficient on the wind speed in order to obtain accurate predictions for a particular configuration and wind environment.

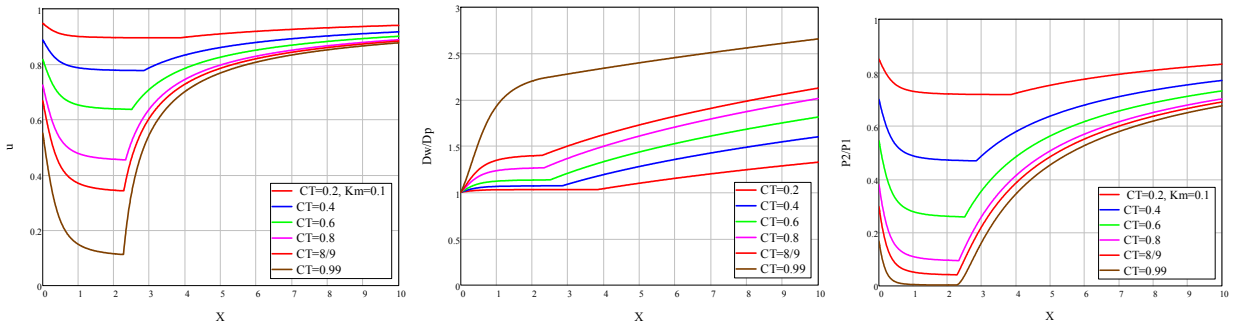

Analytical Wake Model – Model Predication for K_m=0.

Preliminary Results

Preliminary Result for LES of flow over a circular cylinder

The flow over a circular cylinder at Reynolds number 1.4 x 10^5 is simulated. Preliminary results are obtained by LES simulation for flow over a circular cylinder with Re = 1.4 x 10^5. Results will be compared with experimental data and simulation results from similar configurations with other turbulent models.

The computational domian is $-10 \le \frac{x}{D} \le 25$, $-20 \le \frac{y}{D} \le 20$ *and* $-\frac{\pi}{2} \le \frac{z}{D} \le \frac{\pi}{2}$. where x, y and z represent the streamwise, transverse and spanwise directions respectively with the center of the cylinder located and x = y =0.

The computational mesh are generated by ICEMCFD, shows the surface grid of the circular cylinder. The entire domain mesh is also shown, notice fine mesh are adopted especially around the cylinder. The mesh size is 760,080.

The vorticity isosurface colored by velocity magnitude from LES simulations, as expected, is mainly acting in the wake.

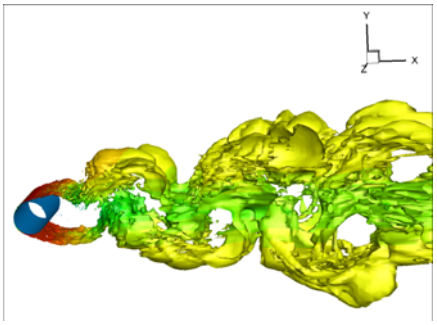

Vorticity isosurface colored by velocity magnitude

The time-averaged pressure coefficient for Re = 1.4 x 10^5 from LES simulation is shown. The spanwise grid distribution has a small effect on the pressure coefficients distribution, the numerical data were averaged in the spanwise direction. Also shown are the oscillations in drag and lift coefficients.

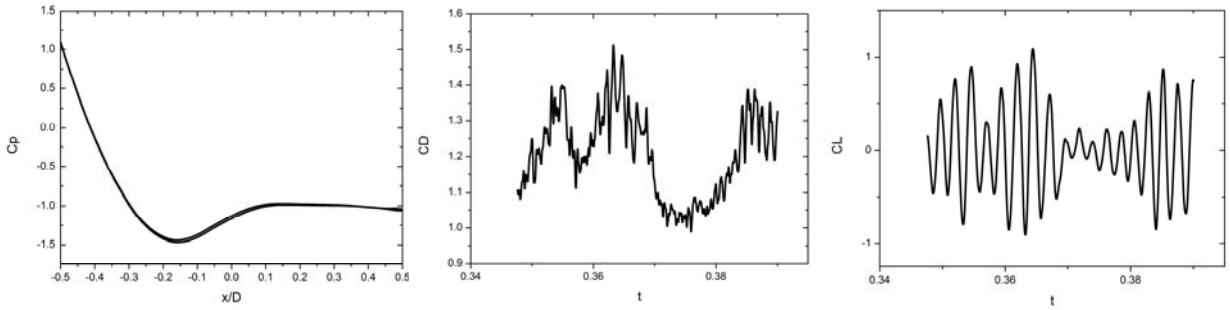

Pressure coefficients and time-dependent drag coefficients and lift coefficients

Preliminary results for ABL simulation

Simulation results are obtained for atmospheric boundary layer simulation from LES model. A simulation of wind conditions is first created for a neutrally stratified atmospheric boundary layer without the presence of turbines. These simulation results will be used as the inlet condition for the simulation with wind turbines. The mesh size is 877,604. Computational meshes are shown below.

Simulation results of temperature and mean temperature are obtained for atmospheric boundary layer simulation from LES model.

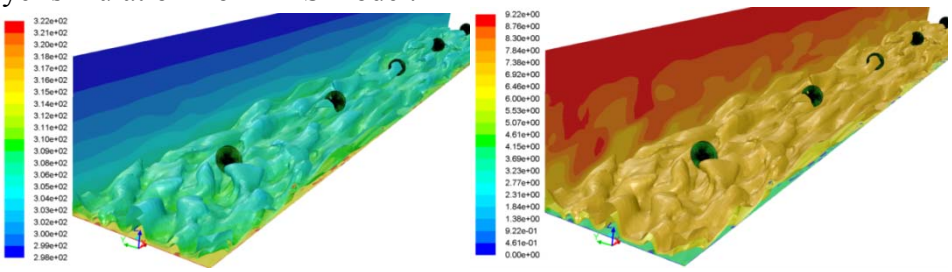

ABL Flow - Contour of Static Temperature (K) and Velocity Magnitude (m/s)

Simulation results of turbulent kinetic energy and velocities are obtained for atmospheric boundary layer simulation from LES model. For different z locations, shown are the kinetic energy plot, (a) shows the x-component velocity (b) shows the y- component velocity and (c) shows the mean velocity distribution.

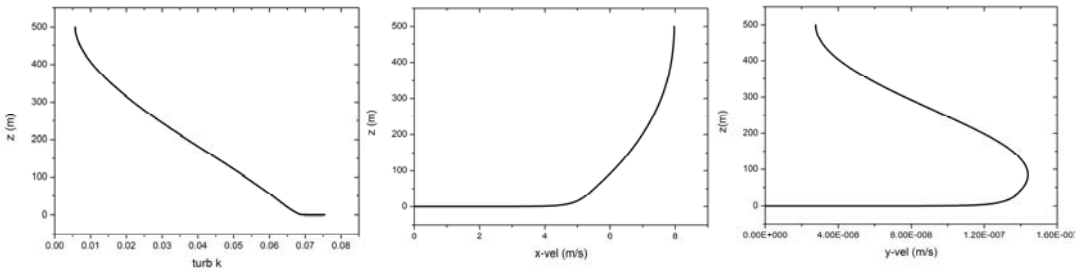

Turbulent kinetic energy

Preliminary results: ABL simulation & wake study - actuator disk model

Simulation results are obtained for atmospheric boundary layer LES simulation combined actuator disk model. The velocity profile and turbulent kinetic energy two rotor diameters down stream of the 2nd turbine are show. It can be seen that there is a significant reduction in the

velocity for the second wind turbine. The kinetic energy profile shows a significant increase in the turbulence level.

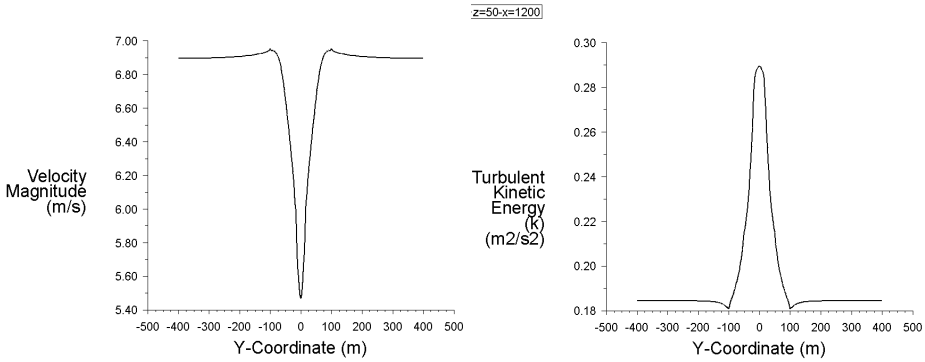

Velocity Profile and Turbulent Kinetic Energy

The velocity profile in the 1D line connecting the center of the two wind turbines is plot. From the result, it is shown that the velocity deficit ratio is about 14%, and the corresponding power deficit ratio is about 37%.

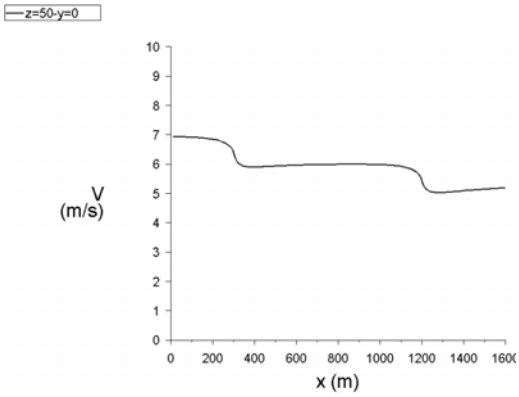

Velocity Profile in the Line Connecting the Center of the Two Wind Turbines

Preliminary results: wake study using actuator line model under neutral condition

Simulation results are obtained for atmospheric boundary layer LES simulation combined actuator line model. The contour plot for iso-surface contour is shown.

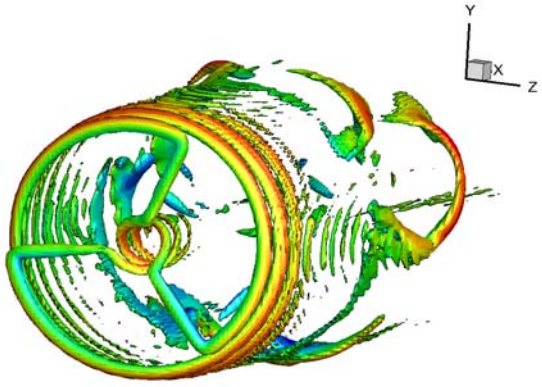

Wind turbine wake simulation with Actuator Line Method – iso-surface contour